MULTIPLE QUANTUM COHERENCES EXPERIMENT, SIMULATIONS AND APPLICATIONS

By

Arman Sainovitch Kussainov

Dissertation

Submitted to the Faculty of the

Graduate School of Vanderbilt University

in partial fulfillment of the requirements

for the degree of

DOCTOR OF PHILOSOPHY

in

Physics

December, 2008

Nashville, Tennessee

Approved:

Professor Daniel F. Gochberg

Professor John C. Gore

Professor Adam W. Anderson

Professor Sait A. Umar

Professor Volker E. Oberacker

ACKNOWLEDGEMENTS

It is a pleasure to thank my science adviser for his endless patience and firm guidance through the stormy seas of science. His everlasting moral and financial support kept me afloat for all these years of grief, sorrow and a rare moments of happiness I've spent at Vanderbilt University.

All members of my PhD committee, past and former ones, Daniel F. Gochberg, Sait A. Umar, Volker E. Oberacker, Adam W. Anderson, John C. Gore, Leonard C. Feldman, as well as my teachers and mentors at Vanderbilt University David J. Ernst, Thomas W. Kephart, Mary Ann Horn, Norman H. Tolk and many others provided invaluable support and knowledge intake necessary to reach this point in my academic career.

Nancy M. Hagans, Dawn Thornton, Ken Willkens, Jarrod M. True, Zou Yue, Amy A. MacKenzie, Kim Hunter, Jane P. Fall, and Captain Bruce W. Martin provided necessary logistics and technical support for my operations on Vanderbilt University campus.

I want to say thanks to E.A. Woodruff III for histology results, Nellie Byun for histology interpretation, and John Fellenstein for construction of the sample holder.

This work was funded from NIH grants EB001452 (Gochberg) and EB000214 (Gore).

Truly yours!

A.S.K.

INTRODUCTION

This thesis discuses the intermolecular multiple quantum coherence (iMQC) phenomenon in nuclear magnetic resonance (NMR). This effect originates from the coherent long range dipole-dipole interactions between spins, and is typically studied with the so-called CRAZED sequence of radio frequency pulses. It is a relatively new development and has attracted interest due to its unusual spin-spin interaction basis and its ability to assess structural information at the hundreds of micrometers distance scale. However, the relationship between the measured signal and the underlying structure is non-trivial, as we will explore both numerically and experimentally.

This thesis is composed of six chapters and two appendices. The first two chapters provide background, on MRI in general and on the CRAZED sequence in particular. Chapter 3 addresses numerical simulations and contains both an overview of the literature and new insights and simulated data concerning cylindrical phantoms and the consequences of employing local vs non-local calculations of the dipolar field and linear vs non-linear calculations of the signal evolution. Chapters 4 and 5 apply the experimental and numerical methods discussed earlier to studies of rat sciatic nerve and mouse liver. Chapter 4 in particular presents new data on the relationship between the CRAZED signal and the underlying sample micro-structures, and it is currently under review for publication. Chapter 6 speculates on the future directions of CRAZED research, while the appendices give the detailed calculations and computer code utilized in the body of the thesis.

TABLE OF CONTENTS

Appendix

LIST OF TABLES

Table Page

LIST OF FIGURES

CHAPTER I

INTRODUCTION TO NMR/MRI

History of subject

The history of NMR/MRI, as a history of every great discovery, has its share of controversy and priority arguments. I will follow the conventional chronological line presented in the sources freely available to the public. Some events described here may have much greater consequences and preconditions than cited but I will keep the description short and relevant to NMR/MRI only.

In 1938, Isidor Isaac Rabi described and measured nuclear magnetic resonance in molecular beams [9]. In 1943, Otto Stern got his Nobel Prize in Physics “for his contribution to the development of the molecular ray method and his discovery of the magnetic moment of the proton” [10]. In 1944, the Nobel Prize in Physics came to Isidor Rabi “for his resonance method for recording the magnetic properties of atomic nuclei” [11]. It is necessary to mention that besides WWII this time stands out for its remarkable progress in the field of atomic energy, theory of radar, and many other discoveries in chemistry and natural sciences, which created a necessary background for rapid development and implementation of NMR. In 1952 Felix Bloch and Edward Mills Purcell got their Nobel Prize in Physics “for their development of new methods for nuclear magnetic precision measurements and discoveries in connection therewith”. The Nobel Prize was an award for independent discovery (published in 1946) of nuclear magnetic resonance in liquids and in solids. Since then nuclear magnetic resonance (NMR) has become widely used to study the molecular structure of pure materials and the composition of mixtures. In 1971, Raymond Damadian discussed in *Science* [12] the way to differentiate tumors and healthy tissue by means of magnetic resonance, thus making the first introduction of NMR to medicine. In 1973, Magnetic Resonance Imaging was first demonstrated on small test tube samples by Paul Christian Lauterbur. That is how the idea of spatial encoding by means of gradients was introduced [13]. In 1975, Richard Ernst proposed magnetic resonance imaging employing phase and frequency encoding methods using the Fourier transform as the main tool for data interpretation. Now this technique is the basis of current NMR/MRI [14]. In 1991, Richard R. Ernst got his Nobel Prize in Chemistry, "for his contributions to the development of the methodology of high resolution nuclear magnetic resonance (NMR) spectroscopy". Recently, in 2003, the Nobel Prize in Physiology or Medicine, "for their discoveries concerning magnetic resonance imaging", went to the Paul C. Lauterbur and Sir Peter Mansfield.

We could keep filling the gaps in our short introduction, year by year, month by month, with detailed description of every remarkable step which has been made. But let us leave this interesting job, at least for now, to the historians of science.

Basics of NMR/MRI experiment

This section introduces several basic concepts of the NMR/MRI experiment, such as the dynamics of a magnetic moment in an external field, how "spin excess" leads to the observable magnetization, and the derivations of the Bloch equation from the basic equations of motion. All descriptions are based on the book by Haacke [1].

Fig.1 diagrams the precession of a magnetic moment in an external field. The angular frequency is

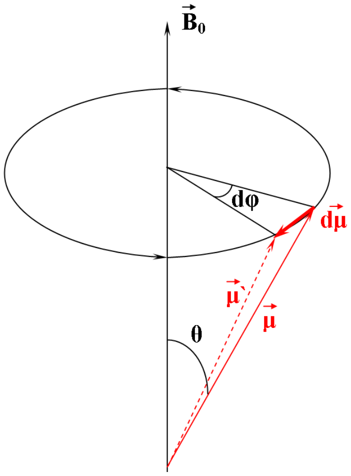

Figure 1: Magnetic moment in an external field B_0. Adapted from [1]

$$\vec{\omega_0} = \gamma \vec{B_0}, \tag{I.1}$$

where γ is the gyromagnetic ratio. Water protons have a γ value of roughly 2.68×10^8 rad/s/Tesla, or $\gamma/(2\pi)$ equal 42.6 MHz/Tesla.

The spin excess in high temperature approximation (for complete analytical expression see Eq.II.37) created by the existence of a preferred direction in space due to $\vec{B_0}$ is equal to

$$Spin\ excess \cong N \frac{\hbar \omega_0}{2kT}, \tag{I.2}$$

where N is the total number of spins in our sample, $\hbar = h/(2\pi)$, T is the temperature in Kelvins, and k is the Boltzmann constant. At the given values of T and B_0 equilibrium magnetization M_0 created by such a disbalance in spin orientation is described by the formula

$$M_0 = \frac{\rho_0 \gamma^2 \hbar^2}{4kT} B_0. \tag{I.3}$$

The observable signal in NMR/MRI is created by flipping/rotating the magnetization into the plane perpendicular to the main B_0 field and observing its precession,which induces signal in the RF coil enclosing the sample (see Fig.2).

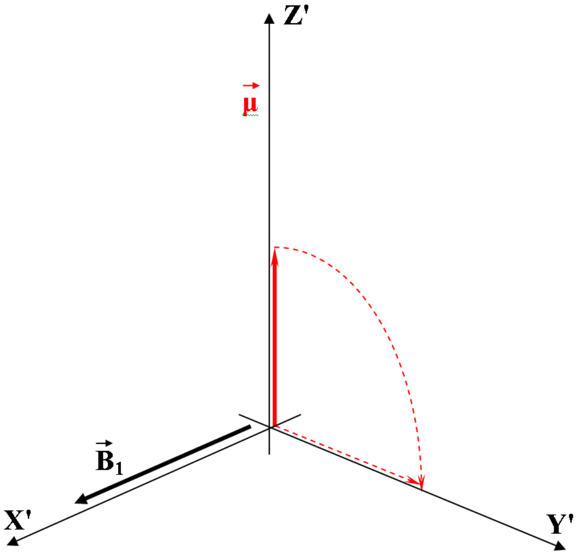

Figure 2: Magnetization flip in rotating frame

The energy which was previously introduced to the system by irradiation with RF (radio frequency) pulse is then dissipated through multiple mechanisms such as “spin-lattice” and “spin-spin” relaxation, radiation damping and diffusion.

“Spin-lattice” interaction results in signal decay, or relaxation. The energy dissipate through interaction with the lattice oscillations or phonons. Magnetization previously rotated away from being aligned along B_0 field regrows back to the Z axis, which is defined to be the direction of the B_0 field. The rate of this process is characterized by a time constant T_1, called the longitudinal relaxation time (see Haacke p.54 for T_1 and T_2 values). If all the magnetization has been rotated into the XY plane ($M_z(0)$=0) than the process of its recovery is described by the following equation

$$M_z(t) = M_0(1 - e^{-t/T_1}). \tag{I.4}$$

The so called "spin-spin" relaxation dephases the spins with a characteristic time constant T_2. It means that even if we observe the signal magnitude decay (which corresponds to magnetization in the X-Y plane) we may not see corresponding regrowth of magnetization back along the Z axis. Magnetization stays in XY plane but due to the lack of coherence between and within individual groups of the spins it is effectively averaged throughout the sample volume. This process is described by the following equation

$$M\perp(T_E) = M_0(1 - e^{-T_R/T_1})e^{-T_E/T_2}, \tag{I.5}$$

where T_R is the repetition time between experiments. T_E ("echo time") is the between when the magnetization is rotated into the X-Y plane and when the signal is acquired. Additional 180^0 pulses may be introduced to eliminate ("refocuse") extra signal dephasing due to the external field inhomogeneities. This combination of RF pulses is usually referred to as a "spin echo" pulse sequence and the T_2^* value in this case is replaced by T_2.

The equation of motion is directly derived from the equation for torque produced by the field on the magnetic moment. After several lines of derivations we can write down the fundamental equation of motion

$$\frac{d\vec{\mu}}{dt} = \gamma\vec{\mu} \times \vec{B}. \tag{I.6}$$

Starting with Eq.I.6, and then incorporating the T_1 and T_2 relaxation effects discussed above, gives the Bloch equation for magnetization vector $\vec{M}$

$$\frac{d\vec{M}}{dt} = \gamma\vec{M} \times \vec{B}_{ext} + \frac{1}{T_1}\left(M_0 - M_z\right)\hat{z} - \frac{1}{T_2}\vec{M}_{\perp}. \tag{I.7}$$

For the case when the external magnetic field is a constant vector $\vec{B}_{ext} = B_0\hat{z}$, Eq.(I.7) may be written as a system of three differential equations

$$\begin{aligned} \frac{dM_z}{dt} &= \frac{M_0 - M_z}{T_1} \\ \frac{dM_x}{dt} &= \omega_0 M_y - \frac{M_x}{T_2} \\ \frac{dM_x}{dt} &= -\omega_0 M_x - \frac{M_x}{T_2}. \end{aligned} \tag{I.8}$$

The solution of this system is

$$\begin{aligned} M_x(t) &= e^{-t/T_2}\left(M_x(0)\cos\omega_0 t + M_y(0)\sin\omega_0 t\right) \\ M_y(t) &= e^{-t/T_2}\left(M_y(0)\cos\omega_0 t - M_x(0)\sin\omega_0 t\right) \\ M_z(t) &= M_z(0)e^{-t/T_1} + M_0(1 - e^{-t/T_1}). \end{aligned} \tag{I.9}$$

The steady–state solution can be obtained by taking $t \to \infty$

$$\begin{aligned} M_x(\infty) = M_y(\infty) &= 0 \\ M_z(\infty) &= M_0. \end{aligned} \tag{I.10}$$

Current state of NMR/MRI and its perspectives

Currently, typical magnetic resonance imaging has resolution limits on the order of a millimeter unless specifically designed and operated at high and ultrahigh (>3 Tesla) field strength, employing parallel imaging coils, entailing long measurement times, or having taken other non-conventional measures. It is widely accepted for its noninvasive nature, speed and specific targeting of the universal medium water.

We discuss some extreme system below that can explore submillimeter structures, and in the next chapter we will begin our discussion of an alternative method for gathering structural information at even smaller (down to $\sim$ 10μm) length scales.

Extreme high field systems

Nowadays the highest magnetic field strengths and gradient values were achieved in the system of National High Magnetic Field Laboratory operated for the National Science Foundation by Florida State University, the University of Florida and Los Alamos National Laboratory (with sites at each of those locations). A 45 T hybrid magnet in Tallahassee, Florida, is capable of producing 45 T constant B_0 in a 32 mm bore. On the short time scale, pulsed magnets can produce fields up to 300

T for 6 μs within 10 mm bore. The Pulsed Field Program is located in Northern New Mexico at Los Alamos National Laboratory. The same site also hosts a proton Magnetic Resonance Imaging System operated at 900 MHz and with a 100 mm room temperature bore [15].

CHAPTER II

CRAZED EXPERIMENT

Multiple spin echoes in solid ^{3}He. First observation and interpretation.

The macroscopic effect of intermolecular multiple quantum coherences (iMQC) in the form of multiple spin echoes was first correctly interpreted by G. Deville *et al.* in [2]. It was 1979 and, as outlined in the introduction, the pulsed gradients technique had already been introduced to NMR. A solid ^{3}He sample, existing along with liquid phase at the temperature T =1 to 20 mK, responded to the sequence of an applied static field gradient two radio-frequency (RF) pulses at times 0 and τ with a train of echoes evenly spaced at times 2τ, 3τ, 4τ, …, nτ (see Fig.3 for the pulse sequence (marked by arrows on the oscilloscope snapshot), resulting signal and numerical simulation data are shown on the right). While the echo at 2τ was expected, the echoes at 3τ, 4τ, . . . could not be explained without adding an additional non-linear term to the Bloch equations.

We are not going to spend too much time elaborating details of this unique low temperature solid state NMR experiment. Later on [3] it was shown that the same type of phenomena can be observed in liquids at room temperature, and we will discuss the theoretical basis of this effect without having to assume extreme relaxation and diffusion values such as those in a low temperature solid. The key point is that introducing a dipole-dipole Hamiltonian into the Bloch equations yields a nonlinear differential equation that explains the CRAZED experiment. We will discuss solutions

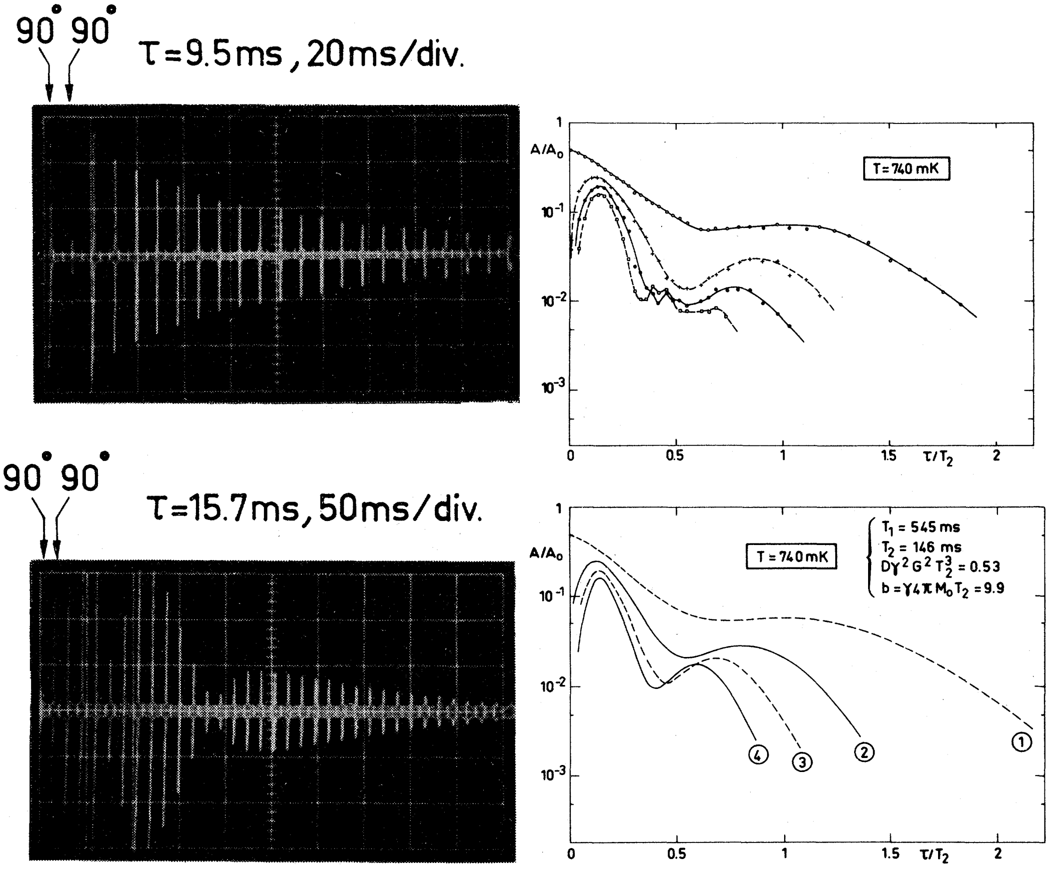

(a) (b)

Figure 3: (a) Multiple echoes patterns obtained for two values of the time interval τ between the 90° radio-frequency pulses. T = 320 mK, the magnetic field H_0 = 9250 G and the molar volume $V_m = 23.6\text{cm}^3$. (b) Experimental (top) and calculated (bottom) amplitudes of some multiple echoes. Reprinted from [2]

for the basic case with and without diffusion and the relationship between this solution and magnetization helix pitch and a defined dipolar demagnetizing time.

Multiple spin echoes in liquids

In 1990, R. Bowtell *et al.* published [3] the theory of the multiple spin echoes in liquids (see Fig.4 for pulse sequence and multiple spin echoes signal), almost right after it was observed for the first time by W. Dürr *et al.* and P. Glover *et al.* and reported at the Annual Meeting Society of Magnetic Resonance in Medicine [16, 17].

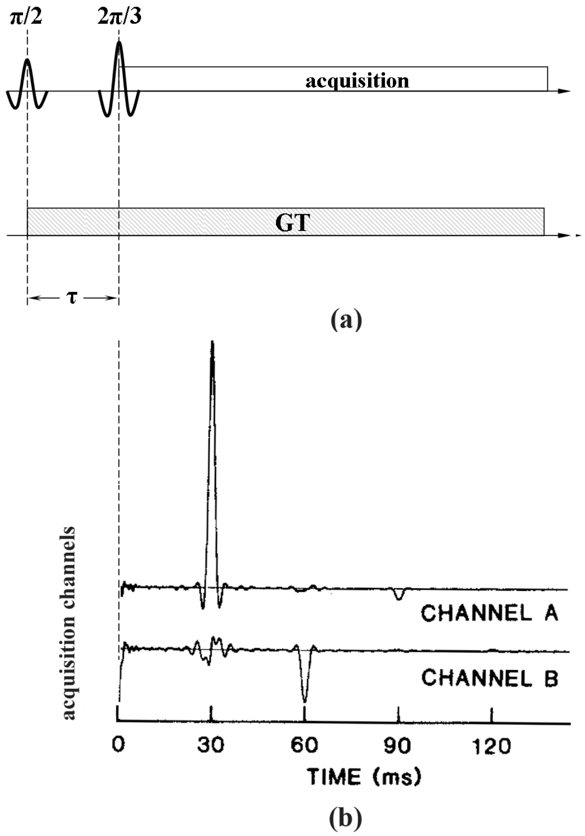

Figure 4: (a)Pulse Sequence. (b) Multiple spin echoe evenly spaced with time interval τ. From Bowtell *et al*[3]

Our line of discussion will proceed from the explicit inclusion of the dipolar demagnetizing field $\mathbf{B_d}(\mathbf{r})$ (as well as a diffusion term) into the Bloch equation I.7.

$$\begin{aligned}\frac{\mathbf{M}(\mathbf{r})}{dt} &= \gamma\mathbf{M}(\mathbf{r}) \times [\mathbf{B}(\mathbf{r}) + \mathbf{B_d}(\mathbf{r})] \\ &- \left(\frac{M_z - M_0}{T_1}\right)\hat{\mathbf{z}} - \left(\frac{M_x\hat{\mathbf{x}} + M_y\hat{\mathbf{y}}}{T_2}\right) + D\nabla^2\mathbf{M}(\mathbf{r}), \qquad \text{(II.1)}\end{aligned}$$

where $\mathbf{M}(\mathbf{r})$ is magnetization, $\mathbf{B}(\mathbf{r})$ is the applied magnetic field, T_1 and T_2 are the relaxation times, D is the diffusion constant, $\hat{\mathbf{x}}$, $\hat{\mathbf{y}}$ and $\hat{\mathbf{z}}$ are Cartesian unit vectors, and $\mathbf{B_d}(\mathbf{r})$ is given by

$$\mathbf{B_d}(\mathbf{r}) = \frac{\mu_0}{4\pi} \int \frac{d^3 r'}{|\mathbf{r} - \mathbf{r}'|} \left[\mathbf{M}(\mathbf{r}') - 3 \left(\frac{\mathbf{M}(\mathbf{r}') \cdot (\mathbf{r} - \mathbf{r}')}{|\mathbf{r} - \mathbf{r}'|} \right) (\mathbf{r} - \mathbf{r}') \right]. \tag{II.2}$$

This expression is nonlocal and unwieldy in all but a limited number of cases when the sample has a simple geometry or the gradients are very large.

For a relatively large gradient, Deville *et al.* [2] has shown that the problem can be simplified. A large uniform field B_0 and a linear gradient G applied along the unit vector $\hat{\mathbf{s}}$

$$\mathbf{B}(\mathbf{r}) = (B_0 + Gs)\hat{\mathbf{z}} \tag{II.3}$$

will ensure that demagnetizing field B_d now depends only on the local magnetization and is given by

$$\mathbf{B_d}(s) = \mu_0 \triangle \left[M_z(s)\hat{\mathbf{z}} - \frac{1}{3}\mathbf{M}(s) \right], \tag{II.4}$$

where

$$\triangle = \frac{1}{2}(3(\hat{\mathbf{s}} \cdot \hat{\mathbf{z}}) - 1). \tag{II.5}$$

The Bloch equation then transforms into

$$\begin{aligned}\frac{d\mathbf{M}(s)}{dt} &= \gamma\left(\mathbf{M}(s)\times\left[B_0+Gs+\mu_0\triangle M_z(s)\right]\hat{\mathbf{z}}\right)\\ -\left(\frac{M_z-M_0}{T_1}\right)\hat{\mathbf{z}} &- \frac{M_x\hat{\mathbf{x}}+M_y\hat{\mathbf{y}}}{T_2}+D\frac{d^2\mathbf{M}(s)}{ds^2}.\end{aligned} \tag{II.6}$$

Einzel *et al.* [18] have shown one way of solving these equations in the simple case when T_1 and T_2 are much greater than τ.

$$M_z\left(s,t\right)=M_0\sum_{n=-\infty}^{n=\infty}b_n\left(t\right)e^{in\gamma Gs\tau} \tag{II.7}$$

$$M^+\left(s,t\right)=M_x+iM_y=M_0e^{-i\gamma Gs\tau}\sum_{n=-\infty}^{n=\infty}a_n\left(t\right)e^{in\gamma Gs\tau}. \tag{II.8}$$

The amplitude of the n-th echo is then $M_0|a_n\left(n\tau\right)|$. Substitution of these equations into Bloch equation gives

$$\frac{da_n}{dt}=-a_n\left(t\right)D\left(\gamma G\right)^2\left(t-n\tau\right)-i\mu_0\gamma\Delta M_0\sum_{p=-\infty}^{p=\infty}a_p\left(t\right)b_{n-p}\left(t\right). \tag{II.9}$$

Initial conditions for the two-pulse sequence is that at the moment $t=0$ only a_0, a_1, b_0, b_1 are nonzero. That is

$$\begin{aligned}b_1(t)&=b_1(0)\exp\left(-D^*t/\tau\right)\\ a_1(t)&=a_1(0)\exp\left(\frac{-D^*}{3}\left(\left[\frac{t}{\tau}-1\right]^3+1\right)\right).\end{aligned} \tag{II.10}$$

for all other orders

$$a_n(t) = -i\mu_0\gamma\triangle M_0 \exp\left(-\frac{D^*}{3}\left(\frac{t}{\tau}-n\right)^3\right) \times \int_0^t \exp\left(\frac{D^*}{3}\left[\frac{t'}{\tau}-n\right]\right) a_{n-1}(t')b_1(t')dt', \tag{II.11}$$

where $D^* = (\gamma G)^2 D\tau^3$. As one can see a_2 is proportional to $(\mu_0\gamma\triangle M_0\tau)$, a_3 is proportional to $(\mu_0\gamma\triangle M_0\tau)^2$ and so on, assuming that $(\mu_0\gamma\triangle M_0\tau) \ll 1$. The initial conditions depends on the amplitudes and phases of the RF pulses as well. That is for the RF pulses $[\phi_1^x\phi_2^x]$

$$b_1(0) = -\frac{\sin(\phi_1)\sin(\phi_2)}{2}\exp\left(-\frac{D^*}{3}\right) \tag{II.12}$$

but for the RF pulses $\left[\phi_1^x\phi_2^{-y}\right]$

$$b_1(0) = +i\frac{\sin(\phi_1)\sin(\phi_2)}{2}\exp\left(-\frac{D^*}{3}\right), \tag{II.13}$$

where ϕ_1 and ϕ_2 are the flip angles and superscripts refer to their phases. In case of both pulses applied along X axis

$$M_0\left|a_1(\tau)\right| = M_0\exp\left(-\frac{2D^*}{3}\right)\sin(\phi_1)\left(\frac{1-\cos(\phi_2)}{2}\right). \tag{II.14}$$

Substitution into Eq.II.11 gives the amplitude of the second echo

$$M_0\|a_2(\tau)\| = \frac{1}{2}M_0\beta F_\beta(D^*)\sin^2\phi_1(1-\cos\phi_2)\sin\phi_2, \tag{II.15}$$

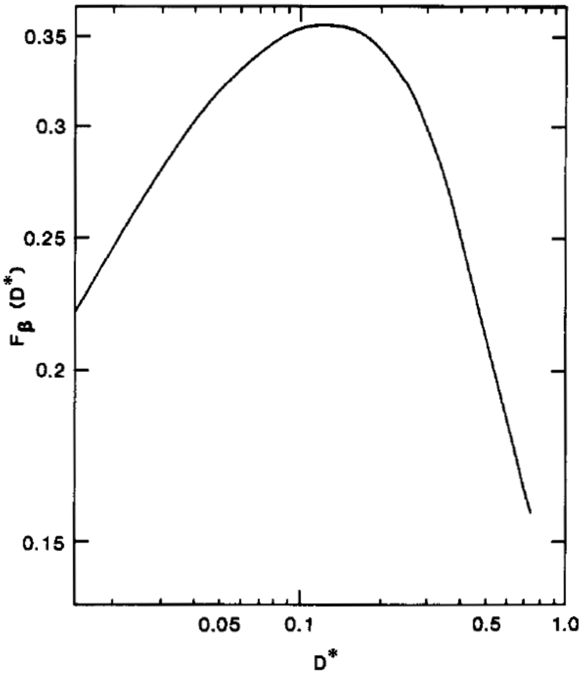

Figure 5: The function $F_\beta(D^*)$. From Bowtell *et al.*

where

$$\beta = \mu_0 \gamma \triangle M_0 \left[D(\gamma G)^2 \right]^{-1/3} \tag{II.16}$$

and

$$F_\beta(D^*) = \frac{1}{2} \pi^{\frac{1}{2}} D^{*-\frac{1}{6}} \exp{(-7D^*/3)} erf(D^{*1/2}). \tag{II.17}$$

Thus the value of the second echo will be maximized when $2\tau = [(\gamma G)^2 D]^{-1/3}$ (see Fig.5).

In order to test the validity of our data, we have reproduced the conditions necessary to observe multiple spin echo in liquids, and we have implemented the pulse sequence displayed in the Fig.4. We measured the ratio of the first two echo heights as function of gradient strength and compared these results to the ratio of Eq.II.14 and Eq.II.15:

$$\left|\frac{a_2(2\tau)}{a_1(\tau)}\right| = exp(2D^*/3)\beta F_\beta(D^*). \tag{II.18}$$

Our sample was 10 mm nmr tube, about 15 cm long filled with 1% $CuSO_4$ solution in disstiled water. Experimental data were acquired on a 7 Tesla 16-cm horizontal bore Varian Inova (Varian Inc., Palo Alto, CA, USA) scanner system running at 300 MHz and using a 25 mm diameter and 22 mm long Litz coil from Doty Scientific,Columbia, SC, USA.

As we can see our data (red dots) and analytical solution (green line) have a very good match (see Fig.4). This agreement with known theory was one of our experimental methods before pursuing the novel measurements described in chapters IV and V.

Quantum mechanical interpretation by Warren.

The "rediscovery" of the multiple spin echoes happened in 1993 with Warren's *et al.* publication in *Science* [19].

Given the name CRAZED (COSY Revamped by Asymetric Z-Gradient Echo Detection), it was set up and described in terms and concepts of 2D NMR spectroscopy [20]. In [5] Richter and Warren presented a method based on the density matrix

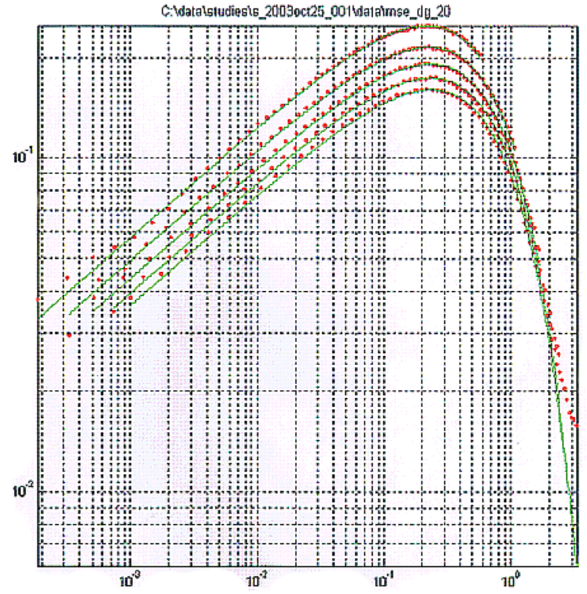

Figure 6: Variation of the ratio of second and first echo amplitude with $D*$ for different values of G. Red circles are our experimental data. Solid green lines are the analytical expression (see Eq.II.18). The gradient is applied along Z axis and takes values [5.3 7.9 10.6 17.6 26.4] $\times 10^{-3}$ T m^{-1} from top line to the bottom.

formalism and using quantum coherences notation and terminology. In contrast, our work stayed within the frame of "classical" (Bloch equation with non-linear terms) description of this experiment, discussed in the previous section. Later by Jeener et al. [21] both these descriptions were shown to be equivalent.

Multiple quantum coherences

Consider the nucleus characterized by its spin $I = 1/2$ and magnetic moment μ connected by the following expression

$$\mu = \gamma I. \tag{II.19}$$

The magnetic moment of the nuclei in the lowest energy state is aligned along the external B_0 field. The gyromagnetic ratio γ sign defines the direction of the angular momentum vector I (for the negative γ it is aligned against the external B_0 field).

Now consider two (spin 1/2) nuclei A and X. The energy levels for such a system are shown on Fig.7(a). If two spins do not interact with each other the system is called uncoupled (see the left part of the Fig.7(a)) otherwise it is called the coupled heteronuclear (containing atoms of the different elements) system. Transitions are between states characterized by the frequencies ν and coupling constant J.

We can describe this system in terms of basis "ket" vectors $|++\rangle$, $|-+\rangle$, $|+-\rangle$, $|--\rangle$, where the first position in the brac"ket" is taken by nucleus A and the second one by nucleus X. As plotted in figure Fig.7(a) , sign "$-$" corresponds to the lowest energy state and is also described by the $\downarrow$ notation (the "+" sign and $\uparrow$ symbol correspond to the highest energy state).

All possible transitions between the states are listed on Fig.7(b). Diagonal elements corresponds to the "populations" of individual states. Off-diagonal elements connect pairs of different states and called "coherences". The order of coherence is defined by the nature of the transition, that is how many "flips" are required to connect the states. Flips have signs and may "cancel" each other. For instance $|++\rangle \rightarrow |-+\rangle$ corresponds to the flip in the state of nucleus A only and represents a *single quantum coherence* 1Q_A while $|-+\rangle \rightarrow |+-\rangle$ corresponds to the flips of both nuclei in different directions and is called a *zero quantum coherence* ZQ_{AX}, although the energy of transition (as could be seen from Fig.7(a)) is not exactly zero.

In general, at thermal equilibrium, any spin system populated according to the

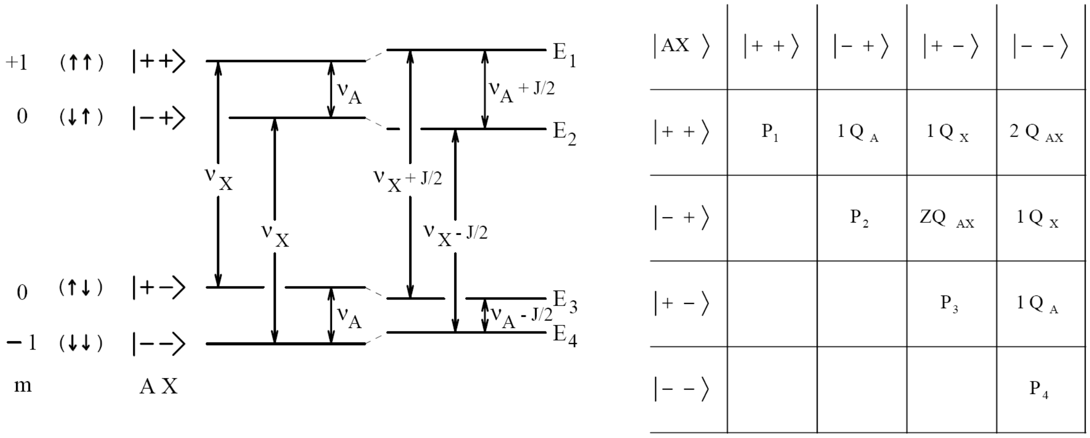

$\lvert AX\rangle$	$\lvert + +\rangle$	$\lvert - +\rangle$	$\lvert + -\rangle$	$\lvert - -\rangle$
$\lvert + +\rangle$	P_1	$1Q_A$	$1Q_X$	$2Q_{AX}$
$\lvert - +\rangle$		P_2	ZQ_{AX}	$1Q_X$
$\lvert + -\rangle$			P_3	$1Q_A$
$\lvert - -\rangle$				P_4

(a) (b)

Figure 7: (a) Coupled and uncoupled energy levels (from left to the right) for the system of two (spin 1/2) nuclei A and X. The values of the total magnetic quantum number are given on the left. (b) The matrix of two-spin system coherences. Pictures adapted with some changes from G. Mateescu *et al.* [4]

Boltzmann distribution has a density matrix given by

$$\rho_{eq} = \frac{\exp\left(-\mathscr{H}\hbar/kT\right)}{\mathrm{tr}\left[\exp\left(-\mathscr{H}\hbar/kT\right)\right]}, \tag{II.20}$$

where $\mathscr{H}$ is hamiltonian, T is the temperature, $\hbar$ is the reduced Planck constant, k is the Boltzmann constant.

For a single spin 1/2 system, the hamiltonian is expressed through the angular momentum operator I_z by the following equation

$$\mathscr{H} = \omega I_z. \tag{II.21}$$

Using the same "ket" notation for the basis functions (see Fig.7(b)), the angular momentum operator for this system can be written as follows

$$I_z = \begin{pmatrix} \langle +|I_z|+\rangle & \langle +|I_z|-\rangle \\ \langle -|I_z|+\rangle & \langle -|I_z|-\rangle \end{pmatrix} = \frac{1}{2}\begin{pmatrix} +1 & 0 \\ 0 & -1 \end{pmatrix}. \tag{II.22}$$

Substitution of Eq.II.22 into Eq.II.21 and Eq.II.20 produces the following expression

$$\rho_{eq} = \frac{\exp\left(-\mathscr{H}\hbar/kT\right)}{\mathrm{tr}\left[\exp\left(-\mathscr{H}\hbar/kT\right)\right]} = \frac{\exp\left((-\hbar\omega/kT)I_z\right)}{\mathrm{tr}\left[\exp\left((-\hbar\omega/kT)I_z\right)\right]} = \frac{\begin{pmatrix} \exp\left(-\frac{\hbar\omega}{2kT}\right) & 0 \\ 0 & \exp\left(+\frac{\hbar\omega}{2kT}\right) \end{pmatrix}}{\exp\left(-\frac{\hbar\omega}{2kT}\right) + \exp\left(+\frac{\hbar\omega}{2kT}\right)}. \tag{II.23}$$

Now consider a system of two isolated 1/2 spins, assuming no coupling. Using the set of basis function defined in Fig.7(b), we can write down the z-component of the angular momentum matrix representation for an individual spin

$$I_{zA} = \begin{pmatrix} \langle ++|I_{zA}|++\rangle & \bullet & \bullet & \bullet \\ \bullet & \langle -+|I_{zA}|-+\rangle & \bullet & \bullet \\ \bullet & \bullet & \bullet & \bullet \\ \bullet & \bullet & \bullet & \bullet \end{pmatrix} = \frac{1}{2}\begin{pmatrix} +1 & 0 & 0 & 0 \\ 0 & -1 & 0 & 0 \\ 0 & 0 & +1 & 0 \\ 0 & 0 & 0 & -1 \end{pmatrix}, \tag{II.24}$$

and for sum of them as follows

$$I_{zA} + I_{zX} = \frac{1}{2}\begin{pmatrix} +1 & 0 & 0 & 0 \\ 0 & -1 & 0 & 0 \\ 0 & 0 & +1 & 0 \\ 0 & 0 & 0 & -1 \end{pmatrix} + \frac{1}{2}\begin{pmatrix} +1 & 0 & 0 & 0 \\ 0 & +1 & 0 & 0 \\ 0 & 0 & -1 & 0 \\ 0 & 0 & 0 & -1 \end{pmatrix}$$

$$= \begin{pmatrix} +1 & 0 & 0 & 0 \\ 0 & 0 & 0 & 0 \\ 0 & 0 & 0 & 0 \\ 0 & 0 & 0 & -1 \end{pmatrix}. \qquad \text{(II.25)}$$

For this two spin system all other components (operators) and their combination may be written as follows

$$I_{xA} = \frac{1}{2}\begin{pmatrix} 0 & +1 & 0 & 0 \\ +1 & 0 & 0 & 0 \\ 0 & 0 & 0 & +1 \\ 0 & 0 & +1 & 0 \end{pmatrix},\ I_{yA} = \frac{1}{2}\begin{pmatrix} 0 & -i & 0 & 0 \\ +i & 0 & 0 & 0 \\ 0 & 0 & 0 & -i \\ 0 & 0 & +i & 0 \end{pmatrix}, \qquad \text{(II.26)}$$

$$(I_x + iI_y)_A = \begin{pmatrix} 0 & +1 & 0 & 0 \\ 0 & 0 & 0 & 0 \\ 0 & 0 & 0 & +1 \\ 0 & 0 & 0 & 0 \end{pmatrix}, \qquad \text{(II.27)}$$

$$I_{xX} = \frac{1}{2}\begin{pmatrix} 0 & 0 & +1 & 0 \\ 0 & 0 & 0 & +1 \\ +1 & 0 & 0 & 0 \\ 0 & +1 & 0 & 0 \end{pmatrix}, \; I_{yX} = \frac{1}{2}\begin{pmatrix} 0 & 0 & -i & 0 \\ 0 & 0 & 0 & -i \\ +i & 0 & 0 & 0 \\ 0 & +i & 0 & 0 \end{pmatrix} \tag{II.28}$$

$$(I_x + iI_y)_X = \begin{pmatrix} 0 & 0 & +1 & 0 \\ 0 & 0 & 0 & +1 \\ 0 & 0 & 0 & 0 \\ 0 & 0 & 0 & 0 \end{pmatrix}. \tag{II.29}$$

These matrices are often referred to as coherences as well. If we take a look at the product of I_{xA} and I_{xX} its operator will take a form of

$$I_{xA}I_{xX} = \frac{1}{2}\cdot\frac{1}{2}\begin{pmatrix} 0 & 0 & 0 & 1 \\ 0 & 0 & 1 & 0 \\ 0 & 1 & 0 & 0 \\ 1 & 0 & 0 & 0 \end{pmatrix}, \tag{II.30}$$

which is the mixture of 2-spin zero quantum ZQ$_{AX}$ and double quantum 2Q$_{AX}$ coherences in the basis plotted in Fig.7(b).

The classical description of NMR by the Bloch equations uses the magnetization vector $\propto \mu$ (see Eq.II.19).

COSY and CRAZED pulse sequences

The next few paragraphs give a short description of the COSY experiment and its interpretation, which is of great importance for the further understanding of the CRAZED pulse sequence.

The correlation spectroscopy (COSY) experiment is a typical 2D experiment. The basic pulse sequence for this experiment is shown in Fig.8(a). Two $\pi/2$ pulses are spaced t_1 time apart and are followed by an evolution time period t_2. The resultant COSY spectrum is a two dimensional Fourier transform of FID values obtained from changing the values of t_1 and t_2 respectively (see Fig.8(b)).

If two distinguishable types of spins (spin A and spin B) are J-coupled, the spins will evolve as follows. After the first $\pi/2$ pulse, each spin will be described by a single-quantum coherences, such as I_{xA}. During the preparation period t_1, the scalar coupling between spins A and B induces evolution to single-quantum coherences like $I_{yA}I_{zB}$, which evolve with the resonance frequency of spin A (ω_A) . At last, application of the second $\pi/2$ pulse transforms them into the single-quantum $I_{zA}I_{yB}$ coherences. Evolution now takes place at the resonance frequency of the second spin species ω_B and the spin system evolves into single-quantum, single-spin coherences like I_{xB}.

Fourier transform of the FID values with respect to t_1 and t_2 yields a two dimensional spectrum of the J-coupled spins, ω_A in F_1 and at ω_B in F_2 direction (see Fig.8(b)). The same considerations for type B spins, and the symmetry of the experiment ensure the appearance of the three other sets of peaks at all possible combinations of ω_A and ω_B.

Next imagine a mixture of acetone and benzene tested with the same COSY

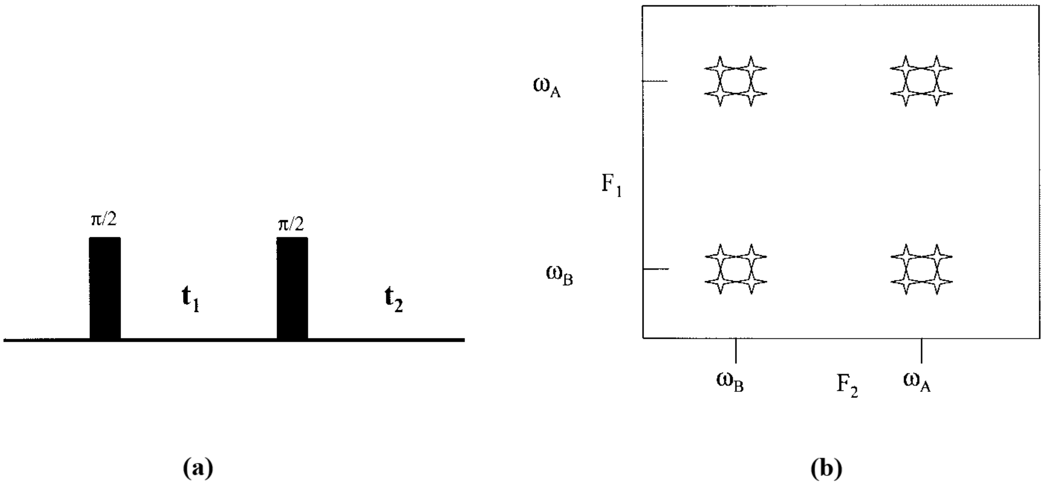

Figure 8: (a) COSY pulse sequence. (b) COSY spectrum of a molecule with two coupled spins. Note that there are cross peaks between all lines. Reproduced from [5]

experiment. The six equivalent J coupled spins in each benzene ring (see [22]) will produce no observable splitting, and will be omitted. The Fourier transform of the FID (1D spectrum) from this mixture contains two lines only and the COSY spectrum (shown in Fig.9(a)) also contains only two diagonal peaks. As expected there are no cross peaks (J coupling) between spins belonging to the different liquids.

Now imagine wee add a "double-quantum gradient filter" to the pulse sequence, as was done in [5] and is illustrated in the Fig.9(b). The action of this filter is as follows. The first gradient pulse modulates the resonance frequency of the spins along the applied gradient direction with the spatial frequency γGT (which could be visualized as a spatial helix of magnetization). Averaging over the whole sample produces no detectable net magnetization associated with this helix. The second gradient pulse is twice the size of the first one and applied after the last $\pi/2$ pulse. This second gradient would, at first glance, to dephase any possible signal appear.

The pulse sequence was named the CRAZED (COSY Revamped by Asymmetric Z-Gradient Echo Detection) sequence after the filtering effect of two gradients. Lin *et al.* [23] have shown that there is a large unexpected signal after this pulse sequence. This result contradicts the classical high-temperature density matrix approximation point of view. As shown on Fig.9(b), there is a full set of peaks along the pseudo-diagonal $F_1 = -2F_2$, and these cross peaks indicate a net coupling between the benzene and acetone protons. Only a breakdown of the density matrix high-temperature approximation [24] may serve as an explanation for the signal observed after the COSY pulse sequence modified by a double quantum filter (see next Eq.II.32). In our

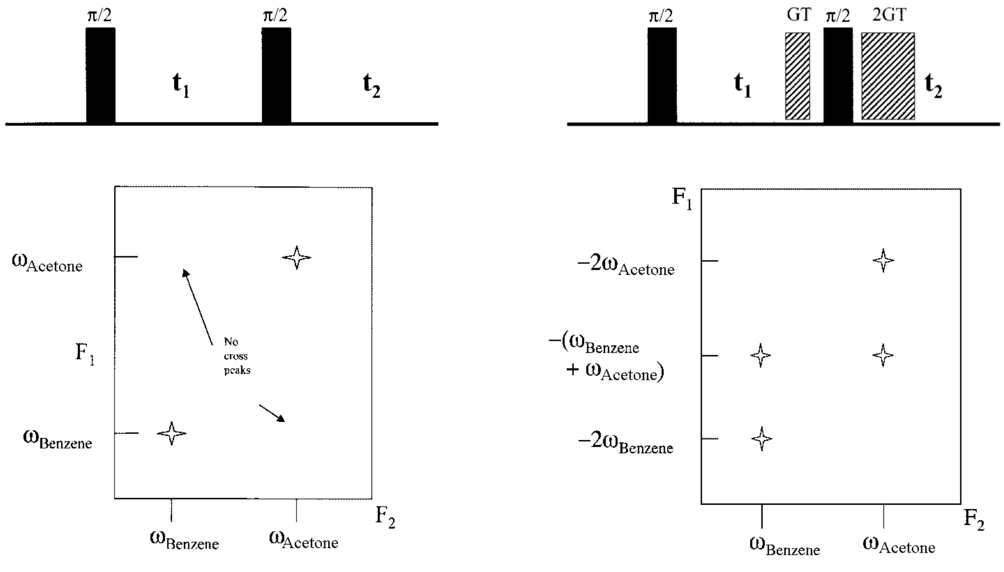

(a) **(b)**

Figure 9: (a) COSY pulse sequence and COSY spectrum of a mixture of acetone and benzene. COSY spectrum shows no cross peaks between them because there is no intermolecular coupling. (b) CRAZED pulse sequence and CRAZED spectrum of a same sample. Intermolecular double-quantum peaks (benzene to acetone spins coupling) are observed supporting the idea of high temperature approximation breakdown. Reproduced from "Intermolecular Multiple Quantum Coherences in Liquids" [5].

previously adopted notation, the high temperature approximation, generally used for the description of all NMR/MRI phenomena, has the following form

$$\rho_0^{HT} = \frac{\exp\left((-\hbar\omega/kT)\sum_i I_{zi}\right)}{\mathrm{tr}\left[\exp\left(-\mathscr{H}/kT\right)\right]} \approx \frac{\mathbf{1} - (\hbar\omega/kT)\sum_i I_{zi}}{\mathrm{tr}\left[\exp\left(-\mathscr{H}/kT\right)\right]}. \tag{II.31}$$

Instead, the Taylor expansion with at least the first three terms should be used

$$\begin{aligned} \rho_0 &= \frac{\exp\left((-\hbar\omega/kT)\sum_i I_{zi}\right)}{\mathrm{tr}\left[\exp\left(-\mathscr{H}/kT\right)\right]} \\ &\approx \frac{\mathbf{1} - (\hbar\omega/kT)\sum_i I_{zi} + (\hbar\omega/kT)^2\sum_i\sum_j I_{zi}I_{zj} - \ldots + \ldots}{\mathrm{tr}\left[\exp\left(-\mathscr{H}/kT\right)\right]}. \end{aligned} \tag{II.32}$$

The first term on the right after the unity matrix is a linear “high-field” approximation and the second quadratic term is the next Taylor expansion term and it is the one which is responsible for an observable signal after the double quantum filter (see [5] for a more complete analytical description).

The main practical inference from the results of this experiment is that we can see the dipole coupled spins belonging to different molecules. If the spatial separation between these spins has a structure imprint on it, then the signal should inherit it as well, which leads us to numerous possible structure studies and applications at the scale previously unavailable for conventional NMR/MRI methods.

CRAZED experiment from the classical point of view

In this section we will revisit the analysis of the CRAZED experiment diagrammed in Fig.9(b). In the last section we analyzed the experiment using quantum mechanical evolution of product operators. In this section, we will perform a “classical” analysis of the magnetization evolution using the modified Bloch equations.

The exact form of the dipolar interaction (see [25]) is given by

$$\mathbf{B}_d(\mathbf{r}) = \frac{\mu_0}{4\pi} \int d^3\mathbf{r}' \, \frac{1}{|\mathbf{r}-\mathbf{r}'|^3} \left[\mathbf{M}\left(\mathbf{r}'\right) - \frac{3\left\langle \mathbf{M}\left(\mathbf{r}'\right), \mathbf{r}-\mathbf{r}'\right\rangle}{|\mathbf{r}-\mathbf{r}'|}\right], \tag{II.33}$$

The secular part, which is the only one left after Zeeman averaging, is

$$\mathbf{B}_d(\mathbf{r}) = \frac{\mu_0}{4\pi} \int d^3\mathbf{r}' \, \frac{1 - 3\ cos^2\ \theta_{rr'}}{2|\mathbf{r}-\mathbf{r}'|^3} \times [3M_z(\mathbf{r}')\hat{\mathbf{z}} - \mathbf{M}(\mathbf{r}')]. \tag{II.34}$$

Remember that the Bloch equation without relaxation and diffusion terms is given by

$$\frac{d\mathbf{M}\left(\mathbf{r}, t\right)}{dt} = \gamma \mathbf{M}\left(\mathbf{r}, \mathbf{t}\right) \times [B_{\mathbf{0}}\hat{\mathbf{z}} + \mathbf{B_d}\left(\mathbf{r}, \mathbf{t}\right)], \tag{II.35}$$

where the constant magnetic field $B_0\hat{\mathbf{z}}$ is augmented by the dipolar field $\mathbf{B_d}\left(\mathbf{r}, t\right)$. Eq.II.34, is a nonlocal function of magnetization distribution and makes Eq. II.35 essentially nonlinear.

Follow the pulse sequence in Fig.9 the magnetization right after θ^y RF pulse in general is

$$M_z = M_0\ \cos\ \theta$$

$$M^+ \equiv M_x + iM_y = M_0\ - sin\ \theta. \tag{II.36}$$

The classical expression for the excess magnetization M_0 per unit volume produced by the difference between the number of spins with $I = 1/2$ aligned up and down along the preferred direction is given by (previously, see Eq.I.2, high temperature approximation has been used)

$$M_0 = \left(\frac{1}{2}\gamma\hbar\right)\frac{N_\alpha - N_\beta}{V} = -\frac{1}{2}\frac{N}{V}\gamma\hbar\ \tanh\left(\frac{\hbar\omega_0}{2kT}\right) = -\frac{1}{4}\frac{N}{V}\gamma\hbar\Im, \tag{II.37}$$

where $\Im = 2\tanh\left(\frac{\hbar\omega_0}{2kT}\right)$. Sign convention used in the previous expressions assumes that positive gyromagnetic ratio gives $M_0 > 0$ and $\Im < 0$.

Making straightforward substitution into differential Eq.II.35 and solving it we'll get

$$\begin{aligned} M^+(t) = M_0\ \sin\theta\ \exp\left(i\triangle\omega t\right)\exp\left(i\gamma M_z t\frac{3}{2}\frac{\mu_0}{4\pi}\int\ d^3\mathbf{r}'\ \frac{1-3\ cos^2\ \theta_{rr'}}{2|\mathbf{r}-\mathbf{r}'|^3}\right) = \\ = M_0\ sin\theta\ \exp\left(i\triangle\omega t\right)\exp\left(-i\frac{N\gamma^2\hbar\Im}{4V}\frac{3}{2}\frac{\mu_0}{4\pi}\int\ d^3\mathbf{r}'\ \frac{1-3\ \cos^2\ \theta_{rr'}}{2|\mathbf{r}-\mathbf{r}'|^3}\right) = \\ = M_0\ \sin\theta\ \exp\left(i\triangle\omega t\right)\exp\left(-i\Im t\ \cos\ \theta\frac{3}{2}\sum_j\ D_{ij}\right), \end{aligned} \tag{II.38}$$

where D_{ij} is

$$D_{ij} = \frac{\mu_0}{4\pi}\frac{\gamma^2\hbar}{4}\frac{1-3\cos^2\theta_{ij}}{r_{ij}^3} = 188.7\left[\frac{1-3\cos^2\theta_{ij}}{r_{ij}^3}\right] rad\cdots s^{-1} \tag{II.39}$$

for ^{1}H and r_{ij} in nm and explicit summation over the spins replaced the integral for the purpose of results comparison which will be done later.s Eq.II.38 says that the zero frequency gets additional shift of $\Im t\cos\theta\frac{3}{2}\sum_j D_{ij}$. In order to get a good visual explanation of the nature of the extra picks in 2D COSY experiment let us right down magnetization for this experiment right after the second $\pi/2$ pulse

$$M(t_2 = 0) = \hat{y}M_0 \ \sin\left(\triangle\omega t_1\right) - \hat{z}M_0 \ \cos\left(\triangle\omega t_1\right), \tag{II.40}$$

which has the same form as Eq.II.38 if we'll make $\theta = \pi + \triangle\omega t_1$.

Substitution into Eq. II.38 gives us

$$M^+\left(t_1, t_2\right) = iM_0 \ \sin\left(\triangle\omega t_1\right) \times \exp\left[i\left(\triangle\omega t_2 + \xi_i \ \cos\left(\triangle\omega t_1\right)\right)\right], \tag{II.41}$$

where $\xi_i = \Im t_2 1.5 \sum_j D_{ij}$.

As we can see from exponential term, frequency shift during t_2 is modulated by the $\cos\left(\triangle\omega t_1\right)$ function producing after Fourier transform multiple peaks.

Under the strong linear gradient assumption [2] the nonlocal expression for the demagnetizing field in Eq. II.34 transformed into

$$B_d(s) = \mu_0 \triangle_s \left[M_z\left(s\right)\hat{z} - M\left(s\right)/3\right] = \left(\triangle_s/\gamma\tau_d M_0\right)\left[M_z\left(s\right)\hat{z} - M\left(s\right)/3\right]. \tag{II.42}$$

Direct substitution to the Bloch equation gives us

$$\begin{aligned} \frac{dM\left(s\right)}{t} &= \gamma\left[M\left(s\right) \times B_0\left(s\right)\right] + \gamma\left[M\left(s\right) \times B_d\left(s\right)\right] = \\ = \gamma\left[M\left(s\right) \times B_0\left(s\right)\right] &+ \gamma\left[M\left(s\right) \times \mu_0 \triangle_s\left[M_z\left(s\right)\hat{z} - M\left(s\right)/3\right]\right] \\ &= \gamma\left[M\left(s\right) \times B_0\left(s\right)\right] + \gamma\left[M\left(s\right) \times \mu_0 \triangle_s M_z\left(s\right)\hat{z}\right]. \end{aligned} \tag{II.43}$$

For the n-quantum CRAZED sequence

$$\begin{aligned} M_z &= -M_0 \ \cos\left[\triangle\omega\left(t_1+T\right)+\gamma GTz\right] \\ M^+ &= iM_0 \ \sin\left[\triangle\omega\left(t_1+T\right)+\gamma GTz\right]. \end{aligned} \tag{II.44}$$

Second gradient and the following evolution in t_2 keeps the M_z constant and changes the transverse magnetization as follows

$$\begin{aligned} M^+ = e^{i\triangle\omega(nT+t_2)} \ e^{in\gamma GTz} \ \exp\left\{i\gamma\mu_0 M_z \triangle_s\left(nT+t_2\right)\right\} iM_0 \\ \times \sin\left[\triangle\omega\left(t_1+T\right)+\gamma GTz\right]. \end{aligned} \tag{II.45}$$

Change of variables $t_1+T \rightarrow t_1$, $nT+t_2 \rightarrow t_2$ plus Bessel function expansion and we can rewrite Eq.II.45

$$\begin{aligned} M^+ &= e^{i\triangle\omega t_2} e^{in\gamma GTz} iM_0 \ sin\left(\triangle\omega t_1+\gamma GTz\right) \\ &\times \sum_{m=-\infty}^{\infty} i^m J_m\left(-t_2\triangle_s/\tau_d\right) e^{im\triangle\omega t_1+im\gamma GTz} \\ &= e^{i\triangle\omega t_2}\frac{M_0}{2}\sum_{m=-\infty}^{\infty} i^m J_m\left(-t_2\triangle_s/\tau_d\right) \\ \times &\left[e^{i(m+1)\triangle\omega t_1+i(n+m+1)\gamma \ GTz} - e^{i(m-1)\triangle\omega t_1+i(n+m-1)\gamma \ GTz}\right]. \end{aligned} \tag{II.46}$$

Strong gradient assumption now means that γGTz winds the magnetization in several turns, thus averaging over the sample makes the signal disappearing unless $m=-n\pm1$

and Eq.II.46 reduces to the next one

$$\begin{aligned}
&M^{+}\left(t_1,t_2\right) = \\
&i^{-1-n}e^{i\triangle\omega t_2}e^{-in\triangle\omega t_1}\frac{M_0}{2}\left[J_{-n-1}\left(-\frac{t_2\triangle_s}{\tau_d}\right)+J_{-n+1}\left(-\frac{t_2\triangle_s}{\tau_d}\right)\right] \\
&= i^{-1-n}e^{i\triangle\omega t_2}e^{-in\triangle\omega t_1}M_0 n\left(\frac{\tau_d}{t_2\triangle_s}\right)\times J_{-n}\left(-\frac{t_2\triangle_s}{\tau_d}\right) \\
&= i^{n-1}e^{i\triangle\omega t_2}e^{-in\triangle\omega t_1}M_0 n\left(\frac{\tau_d}{t_2\triangle_s}\right)\times J_{n}\left(-\frac{t_2\triangle_s}{\tau_d}\right).
\end{aligned} \tag{II.47}$$

CRAZED structure studies

Warren: *"... We have discovered a significant omission in the decades-old theoretical understanding of NMR, and have corrected this omission to reveal new physics and a new imaging method."*[26].

Simple structure studies

The first viable structure application was reported in Science [19]. In this study the presence of biomolecules in water solution was detected through intermolecular quantum coherences and interpreted using a density matrix formalism. It was shown that the CRAZED method can detect the signal originating primarily from pairs of spins separated by about one turn of the magnetization helix. The distance can be adjusted to any value from ∼1 μm up to hundreds of micrometers by varying the gradient strength and length. It was proposed that the intensity of a two-quantum peak between water and dilute molecule inside a cell or vesicle could directly measure the radial distribution function of the water concentration, and this might correlate with local structural abnormalities. A somewhat similar approach has been published by Bowtell one year earlier in 1992 (see [27]).

Despite the fact that analytical solutions containing structure sensitive parameters like magnetization density, helix pitch size or diffusion, existed quite for awhile it took more than ten years to put them together in a reasonable NMR/MRI modality . The quest for robust CRAZED based structure sensitive application is still on. In this section we want to give a short review of the main steps which have been taking in this direction. I'll keep the right to talk about publication which I think relevant to the CRAZED structure applications, omitting the others not less interesting ones.

The first tabulated set of structure scales as an explicit function of correlation distances was obtained for the pair of nested cylinders containing different liquids in 1995. The fact of interaction of one type of the spins with another across the walls of the tube was proved through 2D spectroscopy [28] methods. An interesting fact is that this approach have been reported as an imaging, although one can easily understand it as a result of everlasting pressure for the results.

Similar publication of the next year 1996 came from the group of Bowtell [29] with major difference in numerical simulation method based on Enzel series decomposition. The most unique side of this paper is that Fourier spectrum of modulated magnetization and both Fourier images of the structure and dipolar demagnetizing field were put into correspondence in K-space allowing to predict many observable properties of the signal. Again their sample was constructed from coaxial tubes filled with acetone and water. Unlike the 2D studies of Warren only correlation distance value has been changed through the process of varying modulation gradients.

In order to speed up the acquisition process burdened with multiple averages and/or phase cycling scheme iMQC sequences have been fitted into echo planar imaging [30]. Many functional MRI iMQC applications have been reported as well (see for example [31]).

Non imaging applications of the periodic structures were prevailing in the first years, such as one by Charles-Edwards *et al.* [32] have studied a system of glass beads and glass tubes in a water container. Robyr and Bowtell *et al.* [33] have studied the signal from randomly packed polystyrene microspheres as a function of imposed correlation distance. Double gradient filter have been used unlike the continuous background gradients of the first years. More references can be found in Chapter 5 with respect to our primary biology samples studies.

Shocking abundance of the studies where samples were studied varying d_c (correlation distance) values and fitted to the imaging sequence have followed.In 2002 Louis-Serge Bouchard *et al.* [34] have imaged plastic bottle filled with plastic straws of various size. Many interesting problems such as interference with imaging gradient have been considered. Bowtell *et al.* [6] as well as Alessandri and Capuani [35] have studied plastic holders filled with glass beads later they tried to use the same approach in trabecular bone studies and have been joined by Chih-Liang [36], Louis-S. Bouchard [37] and many others. Number of the CRAZED brain applications is uncountable as well (see for example Zhong [38] and Rizi [39]). Author do not like to make this work look like endless review of the papers were only small variation of samples, timing schemes and numerical interpretations have been introduced and will stop here.

There is a subtle division into CRAZED spectroscopy and imaging applications. The last one merely represent a visualization of spectroscopy methods throughout the volume of the sample under consideration by means of different imaging pulse sequences with only hope to see "unique" or "new" contrast which is in many cases just an imaging artifact.

In order to check the "CRAZED" origin of the image there is a test which almost became a standard. That is a "$3\cos^2(\theta_{gradient}) - 1$" test when the gradients placed along Z, Y and X axis consecutively (assuming that B_0 field is pointed along Z axis). If we subtract the sum of two images intensities when the CRAZED gradients are placed along X and Y axis respectively from the image when the gradients are placed along Z axis we should get a zero intensity image if the origin of the signal is iDQC.

Another approach which stands alone from all other CRAZED applications is a diffraction approach. This one also able to produce analytical results matching the reality but so far without any major practical applications [40].

Paterson autocorrelation function

The most appealing and natural applications of the iMQC phenomena is an attempt to solve a backward reconstruction problem for the unknown geometry based on the DDF measurements. So far it has been done with inconsistent success for the simplest form of the uniform arrays of microbjects [41] and Warren's group has encoded through the correlation gradient strength and direction the macroscopic sample geometry [42]. Then the integral equation for the total signal intensity was solved numerically by a simulated annealing algorithm to recover indicator function of the fluid phase. Group of P.Robyr and R.Bowtell has studied the analytical relationship between the CRAZED signal and Patterson function of the sample [43] producing some general results of an interim value for the tubes filled with glass beads of different size. Patterson function (see Eq.II.48) is closely related to the sample's autocorrelation function and may serve as a good descriptor of the structure if properly reconstructed form the FID signal.

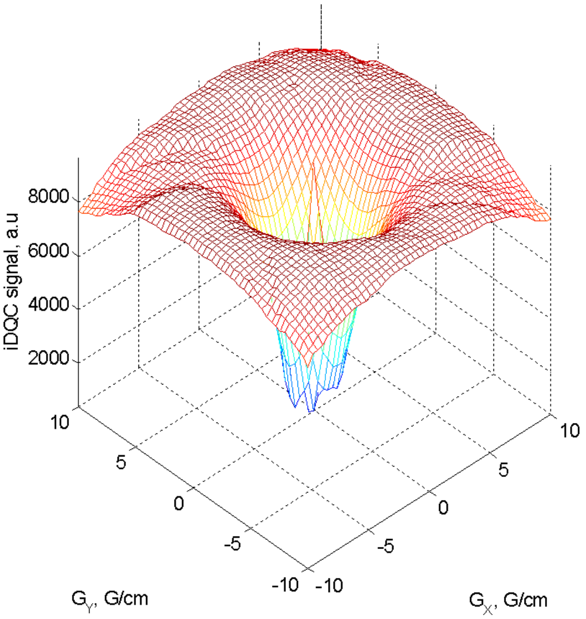

Figure 10: One slice of the data intended for reconstruction of the Patterson function of the long cylinder.

$$P_M(\mathbf{r}) = \frac{i4D}{\gamma\mu_0\pi^{3/2}W(r:D,t)}\frac{2r}{3(\hat{\mathbf{r}}\hat{\mathbf{z}})^2-1}\int_{\infty}^{\infty} d^3k_m S_r(\mathbf{k_m})\exp\left(i\mathbf{k_m}\cdot\mathbf{r}\right), \qquad (\text{II}.48)$$

were $\mathbf{r}$ is the radius vector, D is the coefficient of diffusion, $\mathbf{k_m}$ is the wave vector of the modulation imposed on the transverse magnetization by the first gradient pulse (see Fig.9(b)), t is the time counted from the middle of the second gradient and W is given by the following expression

$$W(r;D,t) = \int_0^{r/\sqrt{8Dt}} \left(1 - \frac{24Dtx^2}{r^2}\right) e^{-x^2} dx - \frac{\sqrt{\pi}}{2}. \tag{II.49}$$

We set up two experiments with the purpose to test practical aspect of this sample shape reconstruction technique. The signal from the long 10 mm nmr tube filled with $CuSO_4$ dopped water have been measured (see Fig.10) and the same type of the data was acquired for the nerve sample prepared in a way described in Chapter 5 (see Fig.11).

One common feature for both experiments is an extremely long acquisition time, on the order of tens of hours to sample the whole k-space for backward reconstruction. We have abandoned this type of measurement as an unpractical. You can see nice 3D evolution of the "$3\cos^2(\theta_{gradient}) - 1$" dependence as a function of the gradient strength, which will be studied in chapter V.

CRAZED imaging

As we mentioned before the imaging application have been produced by fitting the basic spectroscopy sequence into the gradient echo imaging. We have repeated on our 7 Tesla Varian small imaging system experiment as described in [6].

The cross section images of 1 cm nmr tube exhibit expected behavior of the spin

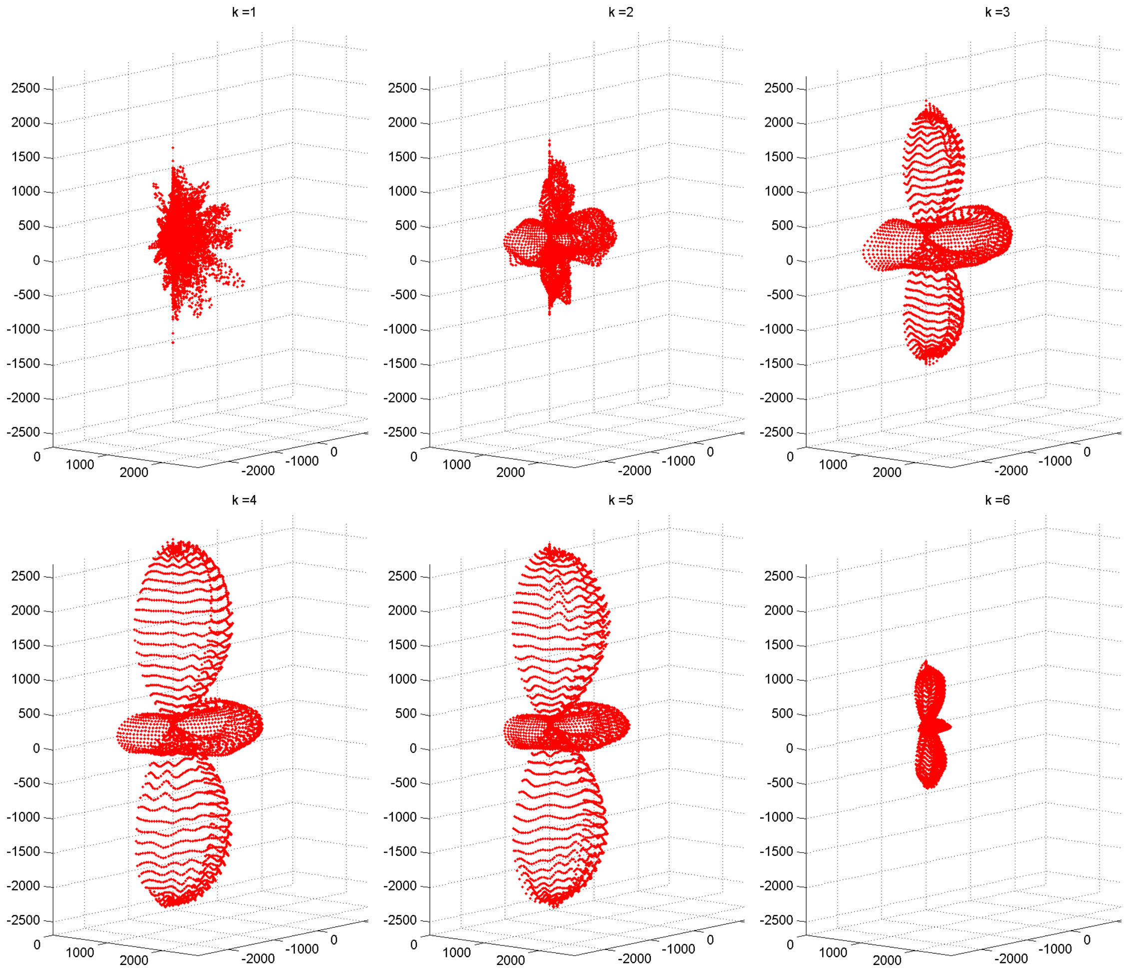

Figure 11: Nerve sample Patterson function studies.

ensemble as a response to the changed CRAZED gradient strength. The bigger the correlation distance the less number of pair of spins contribute to the signal of interest within the limited volume of the sample.

Additional phase cycling schemes alleviate the problem of undesirable coherence pathways and interference of the crazed gradients with the basic imaging gradients. The problem of very long time acquisition still persists. EPI imaging with CRAZED gradients have been tried as well without major success and motivation mainly because the robust applications even for the regular iMQC sequence have not been

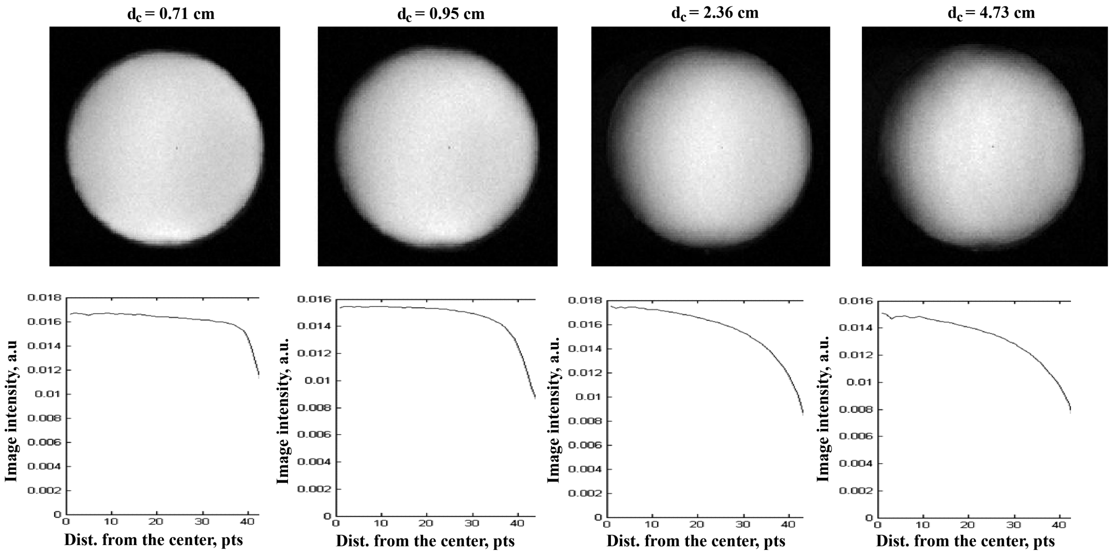

Figure 12: CRAZED imaging. Imposed correlation distance d_c values printed at the top of each image. Image intensity distribution as a function of distance from the center is plotted below. For more details see Bowtell *et al.* [6].

developed yet.

CHAPTER III

NUMERICAL SIMULATIONS

Bloch equation. Linear and nonlinear terms.

Currently, within CRAZED studies, there are two major approaches to the analytical description and subsequent numerical simulation of the dipolar field contribution, provided by Warren and Enzel/Deville/Bowtell, although one may argue that the differences are limited those differences between a Fourier integral and a Fourier series.

In the context of my thesis, the chapter "Numerical Simulations" is limited to the solution of the first order differential equation, the modified Bloch equation, by the Runge–Kutta method [44], or, where it is sufficient, just by the first order term in the Taylor expansion in accordance with the linear approximation. As has been shown previously in [2] when the gradient is sufficiently large, the dipolar field B_d takes the local form in Fourier space, the integral Eq.II.2 is then simply a convolution integral, and our results should be consistent with this.

The B_d field by itself is not of much value unless we introduce it into the Bloch equation, which is an empirical vector equation representing a combination of two relaxation terms with the basic equation of motion of magnetization [1]. If this mathematical model properly incorporates the dipolar field B_d, we may expect the credible reproduction of the free induction decay (FID) in the presence of the real dipolar field and some other, perhaps new, properties of the signal.

$$\frac{\partial M(\mathbf{r},t)}{\partial t} = \gamma \mathbf{M}(\mathbf{r}) \times \left\{ \left[\frac{\Delta\omega}{\gamma}\hat{\mathbf{z}} + G(\hat{\mathbf{s}}\cdot\mathbf{r})\hat{\mathbf{s}} \right] + \mathbf{B}_r(\mathbf{r}) + \mathbf{B}_d(\mathbf{r}) \right\} - \frac{M_x(\mathbf{r})\hat{\mathbf{x}} + M_y(\mathbf{r})\hat{\mathbf{y}}}{T_2(\mathbf{r})} + \frac{M_0(r) + M_z(\mathbf{r})\hat{\mathbf{z}}}{T_1(\mathbf{r})} - D\nabla^2 \mathbf{M}(\mathbf{r},t). \tag{III.1}$$

Eq.(III.1) is a partial differential equation. All three components together represent a set of nonlinear coupled equations. The nonlinearity comes from the $\vec{\mathbf{B_r}}$ and $\vec{\mathbf{B_d}}$ dependence on $\vec{M}$, as will be discussed below. The time of integration is determined by how far we want to follow magnetization evolution. The first term in the curved brackets on the right side represents the effect of chemical shift and applied gradients G. Then we have the non-linear radiation damping and dipolar field terms. The effects of diffusion and relaxation complete the picture. Here and further on in the text we will follow the approach developed by Tilman Enss and Sangdoo Ahn and Warren S. Warren in [7].

The chemical shift, the effect of applied gradients, and relaxation terms are local in space. They involve the local combination of instantaneous magnetization values at each point with relaxation constants and the gyromagnetic ratio. There are still several nonlocal terms left to compute: diffusion, radiation damping and dipolar field.

Radiation damping has the form:

$$\vec{B}_r(\vec{r}) = \frac{\langle M_y \rangle}{\gamma M_0 \tau_r}\hat{\mathbf{x}} + \frac{\langle M_x \rangle}{\gamma M_0 \tau_r}\hat{\mathbf{y}}, \tag{III.2}$$

where $\tau_r = \frac{1}{\gamma \mu_0 M_0 (\eta Q/2)}$, and η is the filling factor and Q is the probe quality factor.

Radiation damping is nonlocal because it involves the average magnetization $\langle M\perp\rangle$ of the sample. But if the B_1 field is uniform throughout the sample, then the radiation damping effect may be treated as the same in every point of the sample. Thus for each step in time we need to calculate B_r only once.

The next term, not so straightforward for our computations, is the dipolar field B_d. As we can see from the expression for the secular part of the DDF field,

$$\vec{B}_d\left(\vec{r}\right) = \frac{\mu_0}{4\pi}\int d^3r'\frac{1-3cos^2\theta_{rr'}}{2|\vec{r}-\vec{r}''|^3}\times\left[3M_z\left(\vec{r}'\right)\hat{z}-\vec{M}\left(\vec{r}'\right)\right] \tag{III.3}$$

it depends on the magnetization values at each point of the sample, which makes it time dependent as well.

Apart from a few special cases, this integral should be calculated directly. Deville et al. [2] have shown that in real space this integral is a convolution product (nice derivation using spherical harmonics is given in recent L.-S Boucahrd *et al.* paper [42])

$$\vec{B}_d\left(\vec{k}\right) = \frac{\mu_0}{6}\left[3\left(\hat{\mathbf{k}}\cdot\hat{\mathbf{z}}\right)^2-1\right]\left\{3M_z\left(\vec{k}\right)\hat{z}-\vec{M}\left(\vec{k}\right)\right\}, \tag{III.4}$$

where

$$\vec{B}_d\left(\vec{k}\right) = \int d^3exp\left(i\vec{k}\cdot\vec{r}\right)\vec{B}_d\left(\vec{r}\right) \tag{III.5}$$

$$\vec{M}\left(\vec{k}\right) = \int d^3exp\left(i\vec{k}\cdot\vec{r}\right)\vec{M}\left(\vec{r}\right). \tag{III.6}$$

For the fully modulated magnetization profile, represented by a single Fourier component, Eq.(III.4) may be written as follows

$$\vec{B}_d(s) = \mu_0 \Delta_s \left[M_z(s)\,\hat{\mathbf{z}} - \frac{1}{3}\vec{M}(s) \right], \tag{III.7}$$

where $\Delta_s = \left[3(\hat{\mathbf{s}} \cdot \hat{\mathbf{z}})^2 - 1\right]/2$ and $k = |k|\hat{\mathbf{s}}$. It is necessary to mention at this point singularity at k=0 for Eq.(III.4), which will be properly treated later.

Thus, instead of the computationally extensive integral Eq.(III.3), we do a fast Fourier transform to get an $\vec{M}\left(\vec{k}\right)$. Then we multiply this three dimensional matrix at every point in Fourier space by the factor

$$\frac{\mu_0}{6}\left[3\left(\hat{k} \cdot \hat{z}\right)^2 - 1\right] \begin{pmatrix} -1 & 0 & 0 \\ 0 & -1 & 0 \\ 0 & 0 & 2 \end{pmatrix}. \tag{III.8}$$

After backward transformation we will get $\vec{B}_d(\vec{r})$.

In the same way, the differential operator for diffusion $D\nabla^2$ can be reduced to the $-Dk^2$ in Fourier space. A flow chart for the method described can be found in Fig.13.

This method has existed for quite a while with many successful applications and we have used it as well for our specific set of phantoms and biological samples. Having the predicting power of a good mathematical model has helped us to highlight specific properties of the geometry under study and has given insight about the next steps necessary to undertake. For the purposes of our calculations, the Matlab, R2006b(73) software package has been used. The computer was running under RedHat Enterprise

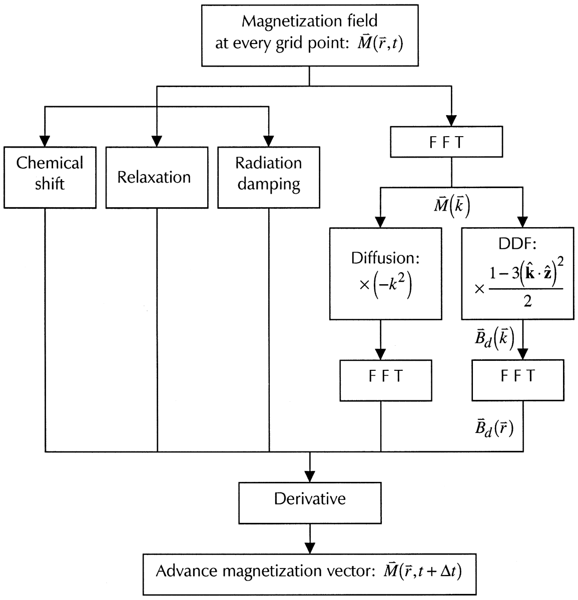

Figure 13: Calculation of the modified Bloch equation. Reproduced from [7].

Linux-WS v4 OS and has Dual Intel(R) XEON(TM) CPU 2.20GHz with 3.5GB RAM and 80GB ATA HD.

Phantom Generation

For the purpose of our simulations, a set of simple phantoms has been created. Spheres, single individual tubes, and groups of fibers, packed or spaced at a certain distance, have been generated using analytical formulas of these objects. A single sample generated in such a way has been used as a “seed” for a sequence of “snapshots,” 3D matrices corresponding to the object sequentially placed at the different angles (see Fig.14). That is, we decided to generate these matrices not analytically but through the application of rotational operators to the seed matrix. See Eq.III.9

$$Q_x\left(\phi\right) = \begin{pmatrix} 1 & 0 & 0 \\ 0 & cos\phi & -sin\phi \\ 0 & sin\phi & cos\phi \end{pmatrix}, \; Q_z\left(\theta\right) = \begin{pmatrix} cos\theta & -sin\theta & 0 \\ sin\theta & cos\theta & 0 \\ 0 & 0 & 1 \end{pmatrix}. \tag{III.9}$$

It is advantageous in a way that the sample may not always have simple geometry and/or possess the analytical description of its shape. Thus, later on, we may use arbitrary shapes supplied from any 3D data acquisition and reconstruction scheme.

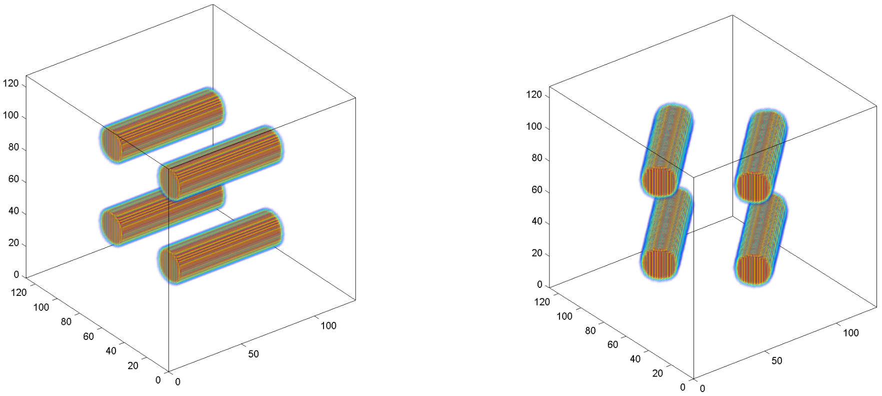

(a) Seed

(b) Rotated Sample

Figure 14: Using initial orientation of the sample along Y axis as a “seed” (a) rotated magnetization distribution (b) has been generated using Eq.III.9

Instantaneous RF pulses and gradients

A Double Quantum Coherence version of the CRAZED sequence has been simulated with a four part phase cycling scheme, (see Fig.15). A Matlab subroutine for

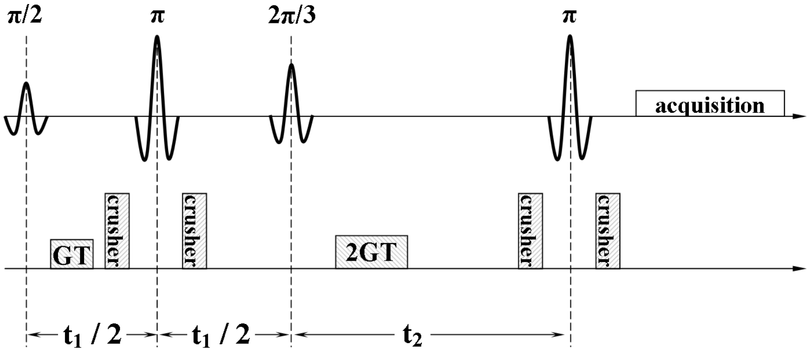

Figure 15: Intermolecular double-quantum coherence pulse sequence with 4 part phase cycling on the first pulse and receiver. All pulses are adiabatic.

the instantaneous RF pulse has been written in such a way that it describes the application of the real RF pulses in an infinitesimally short period of time, (see Appendix A). It means that each point and each component of the 3D matrix representation of magnetization undergoes instantaneous transformation, resulting in a flip of the total magnetization vector on the arbitrary angle.

Instantaneous gradients have been introduced in the same way, that is the phase shift associated with the presence of the gradient has been instantaneously applied to the discretized magnetization values at each point of space, (see Appendix A).

Phase cycling implementation

The phase cycling procedure (see Appendix A) has been implemented with strict random access memory limitations in mind. Just the single matrix of 256×256×256 values of magnetization at each point in space takes 128 Mb of memory. We have created on the hard drive three arrays of magnetization values which have been uploaded and then augmented by the current value magnetization for this particular time step within the current phase step and then saved back to the hard drive. This procedure substitutes slow, but nearly unlimited, hard drive space for the more limited random access memory.

DDF calculations in Fourier space and by direct integration

In this section, we will calculate the single z component of dipolar field B_d using Eq.III.3 and Eq.III.4 considered in the previous section.

We need to create a simulation volume sized N×N×N voxels and center within it a uniformly magnetized cube twice as small (that is $N/2 \times N/2 \times N/2$, see the code in Appendix A for details) with a single nonzero component M_z=1. We want to see how calculation time for the component(s) of dipolar field B_d will depend on the method we use and the value of N. The code does not assume calculation time dependence on the size of the cube, and only one z component of the dipolar field $B_d z$ was calculated. Calculations of all three will take roughly three times as much memory and time unless duly optimized to the symmetry of the problem.

The singularity at $\vec{k} = 0$ in Eq.III.4 presents a complication in making a quantitative comparison of Direct integration versus Fourier space calculations. When our calculations take place in Fourier space, the $\vec{B_d}(\vec{k} = 0)$ is explicitly set equal to zero, which removes the contribution from average value of the calculated magnetization in real space, but has the advantage of avoiding the singularity in Eq.III.4. Other values for $\vec{B_d}(\vec{k} = 0)$ were explored, but without any serious advantages and this strategy has been abandoned. From this point on, the Fourier Transform will called FFT, after its implementation in Matlab as a Fast Fourier Transform.

Table 1: Sample information and performance data for computer systems used for comparison

Linux Workstation		MAC/PC	
processor	: 0	OS Name	:Microsoft Windows XP Professional
vendor id	: AuthenticAMD	OS Version	:5.1.2600 Service Pack 2 Build 2600
cpu family	: 15	OS Manufacturer	:Microsoft Corporation
model	: 4	OS Configuration	:Member Workstation
model name	: AMD Athlon(tm) 64 Processor 3400+	OS Build Type	:Multiprocessor Free
stepping	: 8	Product ID	:76487-OEM-0040055-81049
cpu MHz	: 2200.169	System Manufacturer	:Apple Computer, Inc.
cache size	: 1024 KB	System Model	:MacPro1,1
fpu	: yes	System type	:X86-based PC
fpu exception	: yes	Processor(s)	:4 Processor(s) Installed.
cpuid level	: 1		[01]: x86 Family 6 Model 15
wp	: yes		Stepping 6 GenuineIntel 2659 Mhz
flags	: fpu vme de pse tsc msr pae mce cx8		[02]: x86 Family 6 Model 15
	cx8 apic sep mtrr pge mca cmov pat		Stepping 6 GenuineIntel 2660 Mhz
	pse36 clflush mmx fxsr sse sse2		[03]: x86 Family 6 Model 15
	syscall nx mmxext lm 3dnowext 3dnow		Stepping 6 GenuineIntel 2660 Mhz
bogomips	: 4407.38		[04]: x86 Family 6 Model 15
TLB size	: 1088 4K pages		Stepping 6 GenuineIntel 2660 Mhz
clflush size	: 64	BIOS Version	:APPLE - 5c
cache alignment	: 64	Total Phys Mem	:2,042 MB
address sizes	: 40 bits physical, 48 bits virtual	Avail. Phys Mem	:1,407 MB
		Virt Mem: Max Size	:2,048 MB
		Virt Mem: Avail	:2,008 MB
		Virt Mem: In Use	:40 MB

In our study we have used two computer systems: a Linux Workstation running Red Hat Enterprise Linux OS and a Mac/PC machine running Windows XP Pro. Performance and information pages for both of these systems are generated and printed in Table.1.

Fig.16 plots the data from this “contest” between direct integration (Eq.III.3) and Fourier space calculations (Eq.III.4). As one may expect, the time necessary for the calculation of a single component grows as a power of 3 and 6 for the Fourier Space and Direct Integration method respectively. One may see it as a direct consequence of the code’s nested loops structure reflecting our simulated physical reality.

Fig.17 compares the results of calculating $\vec{B}_d(\vec{k}=0)$ directly and through Fourier space. The differences are quite small and happen predominately close to the edges

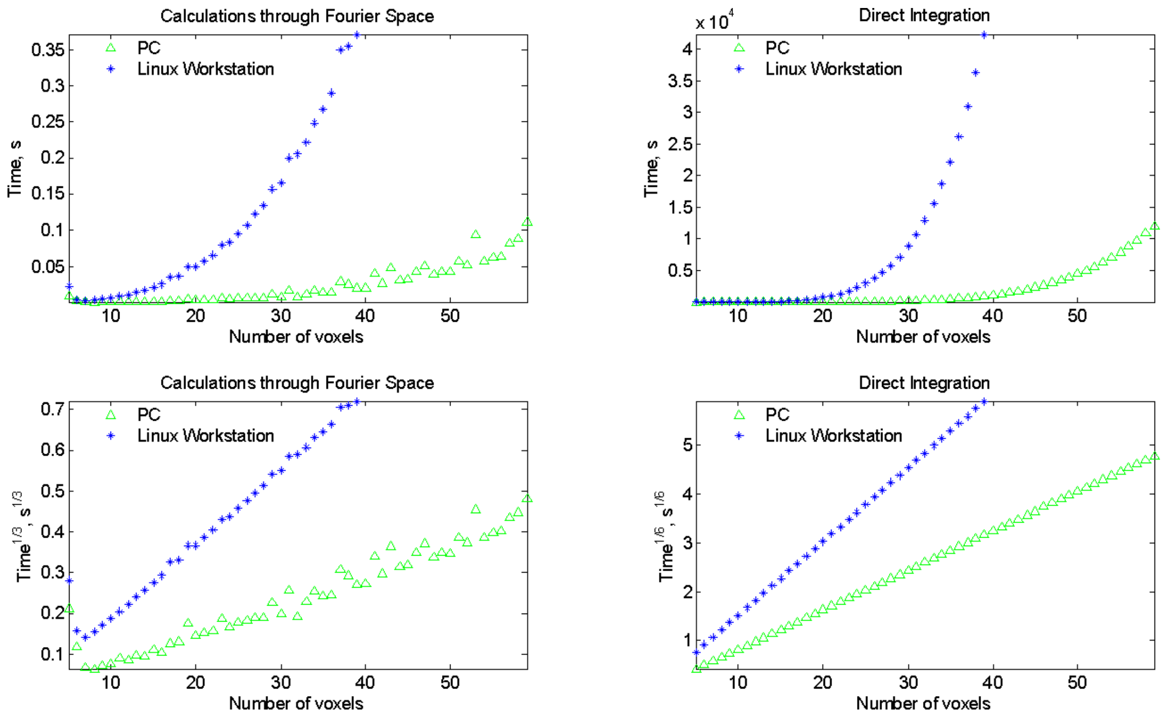

Figure 16: Time comparison for Direct and Fourier calculations

of the simulated space. This difference is due to the inherent repetition in real space that is implicitly assumed when calculating $\vec{B}_d(\vec{k} = 0)$ via FFT. One way to compare two sets of the data is to calculate the value of Ψ, simular to the standard deviation value (see Eq.III.10).

$$\Psi = \sqrt{\frac{\sum_V \left({B_d}^{Fourier} - {B_d}^{Direct}\right)^2}{N^3}}, \tag{III.10}$$

which is plotted as a function of the number of voxels on Fig.18. The key result is that average deviation between the two methods is $\sim 10^{-3}$ times smaller than the equilibrium M_z value of 1, i.e. that calculating B_d in Fourier space adds only a small systematic error.

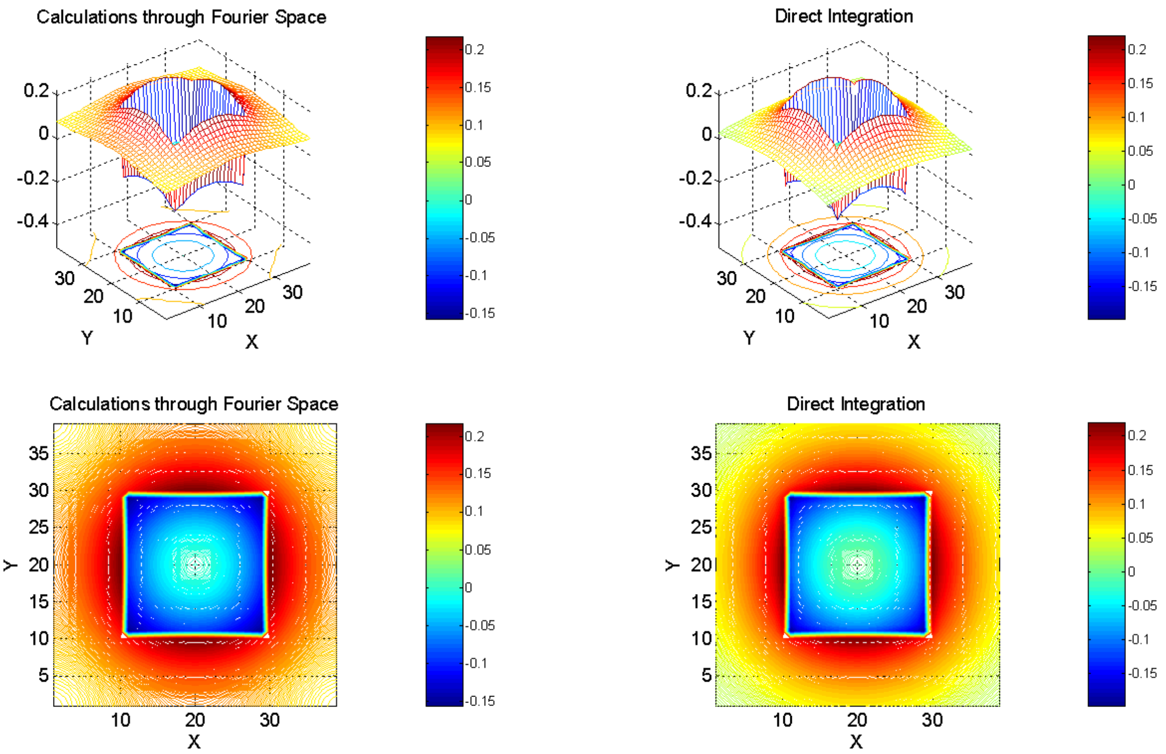

Figure 17: Direct and Fourier calculations for cubical sample

Dependence on memory fragmentation and other factors have not being explicitly accounted for. One may consider the differences which originate from the exclusion of the $\mathbf{k_0}$ component from Fourier method calculations. This question will be addressed in the next section.

Contribution of the $\vec{k} = 0$ component to the dipolar field calculations

The singularity in Eq.III.4 has the following form

$$\lim_{k_x,k_y,k_z \to 0} \left[3 \left(\frac{k_z}{\sqrt{k_x^2 + k_y^2 + k_z^2}} \right)^2 - 1 \right] \qquad \text{(III.11)}$$

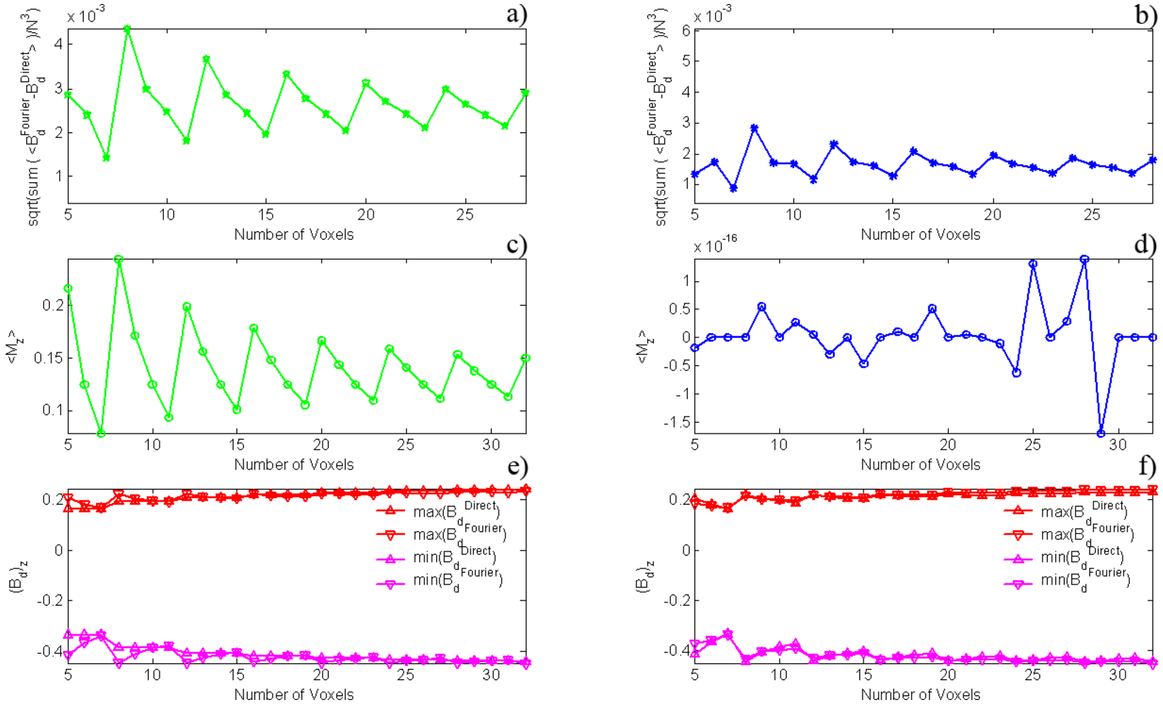

Figure 18: $\Psi = \sqrt{\frac{\sum_V \left({B_d}^{Fourier} - {B_d}^{Direct}\right)^2}{N^3}}$ value as a function of N. Left raw represent the data when $\mathbf{k_0}$ component was set to zero. Right raw represent the data when nonzero $\mathbf{k_0}$ component was intentionally removed from the original magnetization distribution.

and accounts for the exclusion of $\mathbf{k_0}$ component from our calculations. The value of Eq.III.11 depends on how k_x, k_y, k_z approach zero.

From an explicit expression of one dimensional Fourier transform (see Eq.III.12).

$$FFT\left[x\left(n\right)\right] = X\left(k\right) = \sum_{n=1}^{N} x\left(n\right)\exp\left(-j\cdot 2\pi\left(k-1\right)\left(n-1\right)/N\right), \qquad 1 \leq k \leq N, \qquad \text{(III.12)}$$

one can see that the $\vec{k} = 0$ ($\vec{k} = 1$ in our one dimensional calculation based on Matlab conventions) component, which is the first term of the sum to the right, is just an average value of the function taken over the simulation grid (see Eq.III.13).

$$x(n) = \frac{1}{N} X(k=1) + \frac{1}{N} \sum_{k=2}^{N} X(k) \exp\left(j \cdot 2\pi (k-1)(n-1)/N\right), \quad 1 \le n \le N. \qquad \text{(III.13)}$$

Thus, if the original magnetization distribution does not have any average value or it has been subtracted (see Eq.III.14).

$$x(n) - \frac{1}{N} \sum_{n=1}^{N} x(n) = x(n) - \langle x(n) \rangle =$$
$$\frac{1}{N} \sum_{k=2}^{N} X(k) \exp\left(j \cdot 2\pi (k-1)(n-1)/N\right), \; 1 \le n \le N.$$
$$x(n) - \langle x(n) \rangle = IFFT\left(X(k) \Big|_{k_0=0} \right) \qquad \text{(III.14)}$$

Eq.III.4 will have exact numerical equivalent.

These considerations are the basis for Warren's treatment of the $\mathbf{k_0}$ component referred to in [7] and studied previously in detail in [45].

There is a question of what to do with the fictitious magnetization profile which was created by subtraction of the average value of magnetization everywhere over the simulation volume. The answer, found by numerical simulations, in most cases, is nothing.

This results becomes clear by visualizing the effect of the dipolar field in Fourier space. Fig.19 plots the 3D matrix of the dipolar weighting coefficients. As one might expect from our previous considerations (see Eqs.III.12-III.14) the $\vec{k} = 0$ contribution to the calculated DDF value needs to be computed by a different method than all other

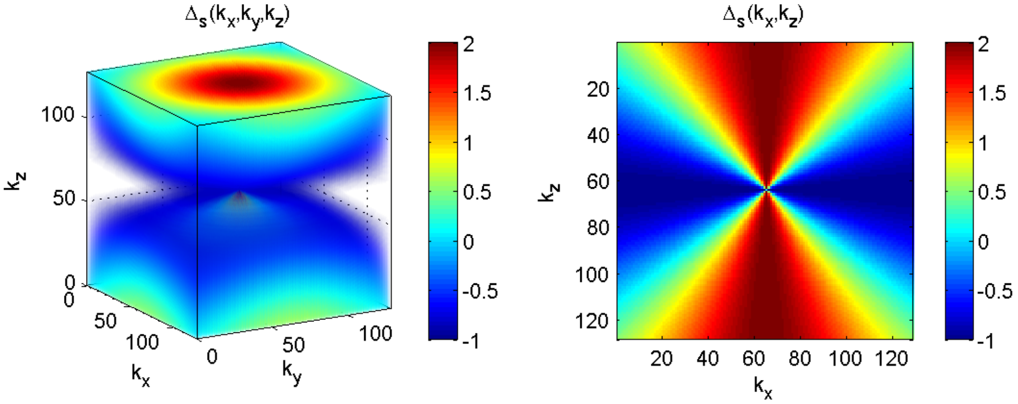

Figure 19: Dipolar Coefficient

Fourier components. Specifically, we will calculate the $\vec{k}=0$ component contribution in r-space, thus avoiding the singularity noted in Eq.III.4 and Eq.III.11, i.e. we will use:

$$\vec{B_d}\left(\vec{r}\right)^{\mathbf{k=0}} = \frac{\mu_0}{4\pi}\int d^3r' \frac{1-3cos^2\theta_{rr'}}{2|\vec{r}-\vec{r'}'|^3} \times \left[3\langle M_z\left(\vec{r'}\right)\rangle\hat{z} - \langle\vec{M}\left(\vec{r'}\right)\rangle\right], \tag{III.15}$$

in which the triangle brackets correspond to the average values of magnetization components over the simulation volume, in accordance with Eqs.III.12-III.14. We will then add this contribution to the $\vec{B_d}(\vec{r})$ calculated via Eq.III.4.

We have implemented this procedure numerically in Appendix B (see the quoted part of the ddf.m function). It is computationally equivalent to the calculation of the DDF field by the direct method (see Eq.III.3). The key result is that including the contribution to $\vec{B_b}(\vec{r})$ from the $\vec{k}=0$ component of $\vec{M}(\vec{k})$ makes extremely little difference. Its contribution small and becomes negligible as soon as magnetization is significantly modulated and the $\vec{k}=0$ component value naturally goes to zero.

Typical data from numerical simulations. Fitting the Bessel function

Fig.20 represents a typical snapshot of our simulation program interface. The basic layout of our output GUI changes on a regular basis depending on the goal of a particular simulation. Here is a list of the elements with explanations given in the order of their appearance:

1. "Number of voxels = 128" corresponds to the size of our simulation grid, which is 128 by 128 by 128 in this case.

2. "Sample Radius = 32 voxels" is the radius of the phantom if it is spherical (disc) or half the length of its side if it is cubical.

3. "$R_1 = 0s^{-1}$" and "$R_2 = 0s^{-1}$" are the relaxation rates.

4. "τ_{dipol}" is a dipolar time $\tau_{dipolar} = 1/\left(\gamma\mu_0 M_0\right)$.

5. "τ_{damp}" is the radiation damping time $\tau_{damping} = \tau_{dipolar}/\left(\eta Q/2\right)$.

6. "K-space = n" filter refers to filtering in the Fourier space to reduce Gibss ringing.

The next column continues to give general descriptions of the numerical experiment set up.

1. "Voxel size = 0.15625 mm" is the size in real units of measurements ascribed to the simulation volume; that is, we put the 128×128×128 simulation volume in correspondence with a 2×2×2 cm cube in the real space, which resulted in 20 mm /128 pts = 0.15625 mm voxel size (see the next two items).

2. “Sample size =5 mm” is the phantom size.
3. “Volume size= $20\times20\times20$ mm^{3}” is the size of the smallest discrete element in the simulation grid.
4. “RF pulses =[90 90] degrees” are the flip angles of the α and β pulses.
5. “RF phases =[90 90] degrees” are the phases of RF pulses.
6. “First inst_grad = [0.011 0.011 0.125] cycles/voxel” refers to the first gradient orthogonal component along each major axis [x y z]. The units of measurement reflect the effect this gradient produces on the magnetization. This gradient winds the magnetization to a certain number of cycles per voxel.
7. “First inst_grad = [0.0002 0.0002 0.0019] Gauss/cm*s” The next line shows the same gradient in terms of (Gauss per cm) × second. Because our gradients are treated as instantaneous, the units are modified to incorporate s multiplier.
8. “Correlation distance d$_c$=[7.1023 7.1023 0.625] mm” is calculated in accordance to the formula $d_c = \pi/(\gamma GT)$ and given in this case in mm.

The last column is of general interest and gives the shape of our sample (“cube”), value of B_0 field (7 Tesla), time integration step “dt =0.05 s” (in case we have more than one) and “calculation time =72.92 minutes” which is the time required for the program to run from the very beginning until the last piece of data has been displayed.

Approximately 250 ms after we began to sample the signal, it started to deviate from the Bessel function. That is the time when the nonlocal nature of the dipolar

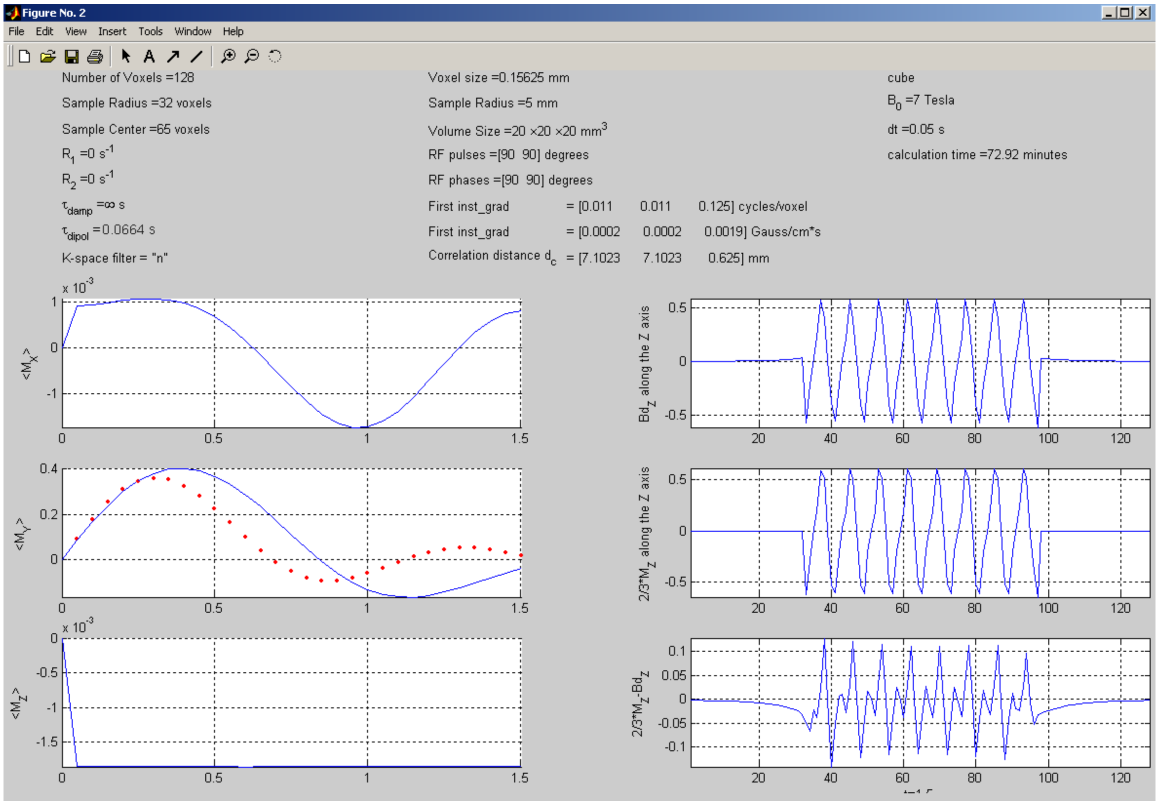

Number of Voxels =128

Sample Radius =32 voxels

Sample Center =65 voxels

R_1 =0 s^{-1}

R_2 =0 s^{-1}

τ_{damp} =∞ s

τ_{dipol} =0.0664 s

K-space filter = "n"

Voxel size =0.15625 mm

Sample Radius =5 mm

Volume Size =20 ×20 ×20 mm^3

RF pulses =[90 90] degrees

RF phases =[90 90] degrees

First inst_grad = [0.011 0.011 0.125] cycles/voxel

First inst_grad = [0.0002 0.0002 0.0019] Gauss/cm*s

Correlation distance d_c = [7.1023 7.1023 0.625] mm

cube

B_0 =7 Tesla

dt =0.05 s

calculation time =72.92 minutes

Figure 20: Snapshot of the simulation program interface for the cubical sample 64 by 64 by 64 points under basic conditions. No relaxation processes, radiation damping is neglected

field manifests itself. This simulation program calculates $\vec{B}_d(\vec{r})$ using the Fourier space method discussed in the previous sections. In the limit of high G, we expect a local relation (Eq.III.7), which leads to a Bessel function growth in time. Clearly, this result is not the case for our general simulations.

So far the majority of publications have been content with the linear part of magnetization evolution under the dipolar field. From the point of view of the numerical simulations it looks quite reasonable. Within the linear regime only the initial slope of the time evolution of the signal ($\langle M_y \rangle$ in Fig.20) is relevant. This is all we need for the experiment described in chapters IV and V. Unless we need to follow the magnetization evolution for a time period on the order of $\tau_{dipolar}$ or longer, there is no need to perform computationally extensive simulations, with the more than one time step (see section “DDF calculations in Fourier space and by direct integration”. For water at room temperature and a B_0 field of 7 Tesla, $\tau_{dipolar} = (\gamma \mu_0 M_0)^{-1} \approx 70$ ms, see Fig.20).

We have also tested experimentally that as long as we stay within the linear regime or, more precisely, within the time period when the DQC signal grows and reaches its maximum, all properties of the signal we have mentioned previously in relation to the numerical simulation stay the same. It should be mentioned that the maximum in DQC signal observed experimentally does not necessarily correspond to the 2.2 $\tau_{dipolar}$ maximum dictated by the analytical expression. Typically this echo amplitude has been modified and shifted to much earlier times by T_1 and T_2 relaxation processes plus diffusion and radiation damping.

When the signal decay due to T_2/T_1 relaxations and/or diffusion damping is long enough (compare to $\tau_{dipolar}$) oscillatory behavior of the signal, as illustrated in Fig.20. In the literature, this regime is called nonlinear. Use of term “non-linear” may be confusing. There are two ways in which the CRAZED experiment is nonlinear: 1) the signal is non-linear in time, though often, as in chapters IV and V, we only calculate the linear regime. 2) The Bloch equation is non-linear in $\vec{M}$. We are currently discussing the first case. At the beginning of this chapters, we discussed the second case.

There actually is a subtle connection between these two uses of the term “non-linear”. In chapter IV and V we will use magnetization at time $t = 0$ to determine $\frac{d\vec{M}}{dt}$, and we will also approximate the signal as proportional to $\frac{d\vec{M}}{dt}$. In this sense, we get rid of both non-linearities. That is, if you only use the linear term in the time evolution, you lose at least some of the unusual effects of $\frac{d\vec{M}}{dt}$ being non-linear in $\vec{M}$.

The nonlinear regime was studied in a recent paper of Marques *et al.* [46]. It should be mentioned that this study uses different type of simulations which is limited the accurate regime of the solution of the system of differential equations.

Take a look at the output of our numerical simulations in Fig.20. The linear regime was expected to be and was observed up to ≈ 300 ms (the maximum of the signal happens to be at $2.2\tau_{dipolar}$). The red dotted line represents the predicted Bessel function behavior and the solid blue line represents our numerical simulations. The linear regime is maintained if $t_2/\tau_{dipolar} \ll 1$ which makes $J_m\left(t_2/\tau_{dipolar}\right) \propto \left(t_2/\tau_{dipolar}\right)^m$. In this case J_{n-1} term dominates and the signal varies as $\left(t_2/\tau_{dipolar}\right)^{n-1}$ which is exactly what we see in our simulations. After ≈ 300 ms these approximate relationships are not valid anymore.

It is possible to make the first maximum in simulations happens closer to the first maximum of the predicted Bessel function by using a finer grid size (and a bigger number of voxels) which will allow us to simulate stronger gradients. That will make linear dependence (somewhat different from the term "linear regime" if referring to the evolution from the initial unperturbed state of magnetization) between magnetization M and induced dipolar field B_d valid for a longer period of time.

We have enough elements to efficiently reproduce an evolution of magnetization under the Bloch equation. In order to validate this statement we can explicitly make the linear approximation regime ($B_d \sim M$) valid throughout the whole time course of magnetization evolution (see Fig.21). Numerically, it is done by making a matrix of

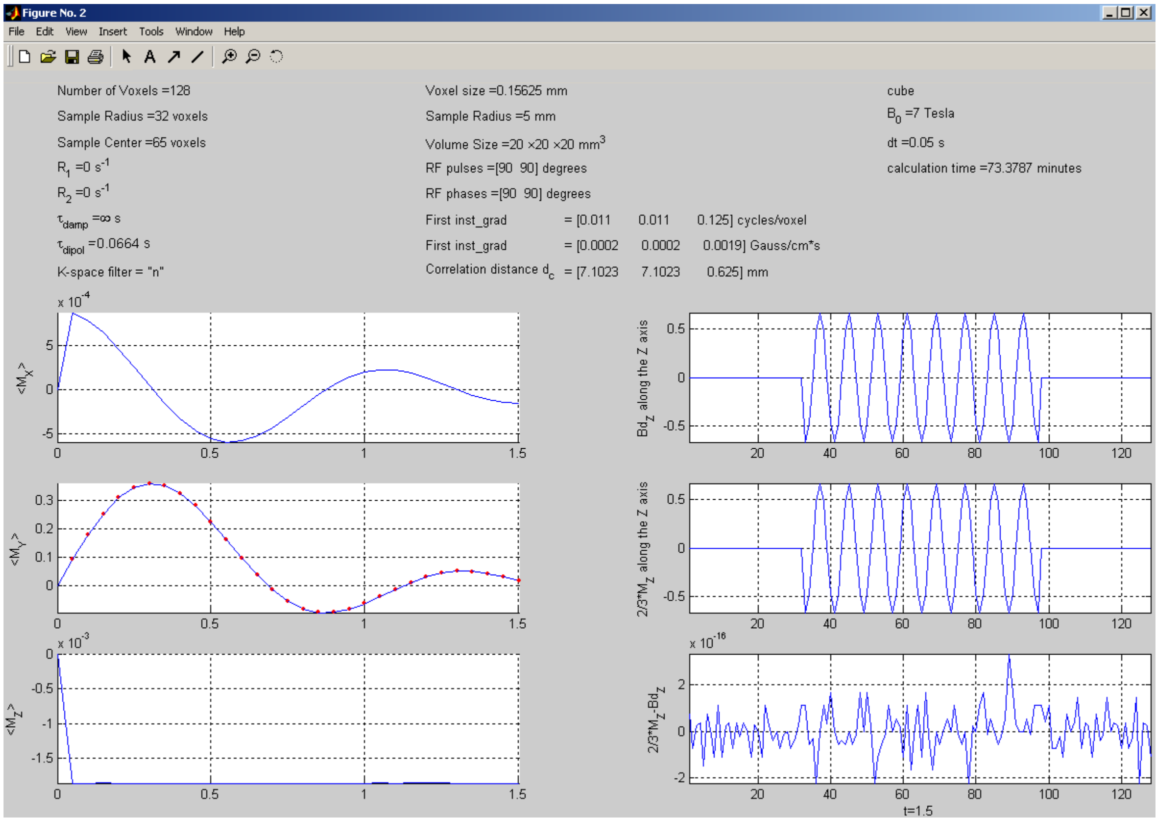

Number of Voxels =128
Sample Radius =32 voxels
Sample Center =65 voxels
R_1 =0 s^{-1}
R_2 =0 s^{-1}
τ_{damp} =∞ s
τ_{dipol} =0.0664 s
K-space filter = "n"

Voxel size =0.15625 mm
Sample Radius =5 mm
Volume Size =20 ×20 ×20 mm^3
RF pulses =[90 90] degrees
RF phases =[90 90] degrees
First inst_grad = [0.011 0.011 0.125] cycles/voxel
First inst_grad = [0.0002 0.0002 0.0019] Gauss/cm*s
Correlation distance d_c = [7.1023 7.1023 0.625] mm

cube
B_0 =7 Tesla
dt =0.05 s
calculation time =73.3787 minutes

Figure 21: Magnetization evolution under Bloch equation. Strong gradient assumption was simulated by making the matrix of dipolar coefficients in the K-space equal to 1.

dipolar weighting coefficients explicitly equal to the unit matrix. Physically, it means that $B_d \sim \alpha M$ for any moment in time, not only at the initial stage (see Fig.21).

The closest match between the simulations and the predicted Bessel function-like behavior we were able to achieve was when the number of voxels=265 and CRAZED gradients were strong enough to wind the magnetization helix more than 10 times across the sample. It does not mean that our data is wrong; as explained above, we just can not numerically simulate long nonlinear behavior directly. Another analytical method will be described in the last section of this chapter.

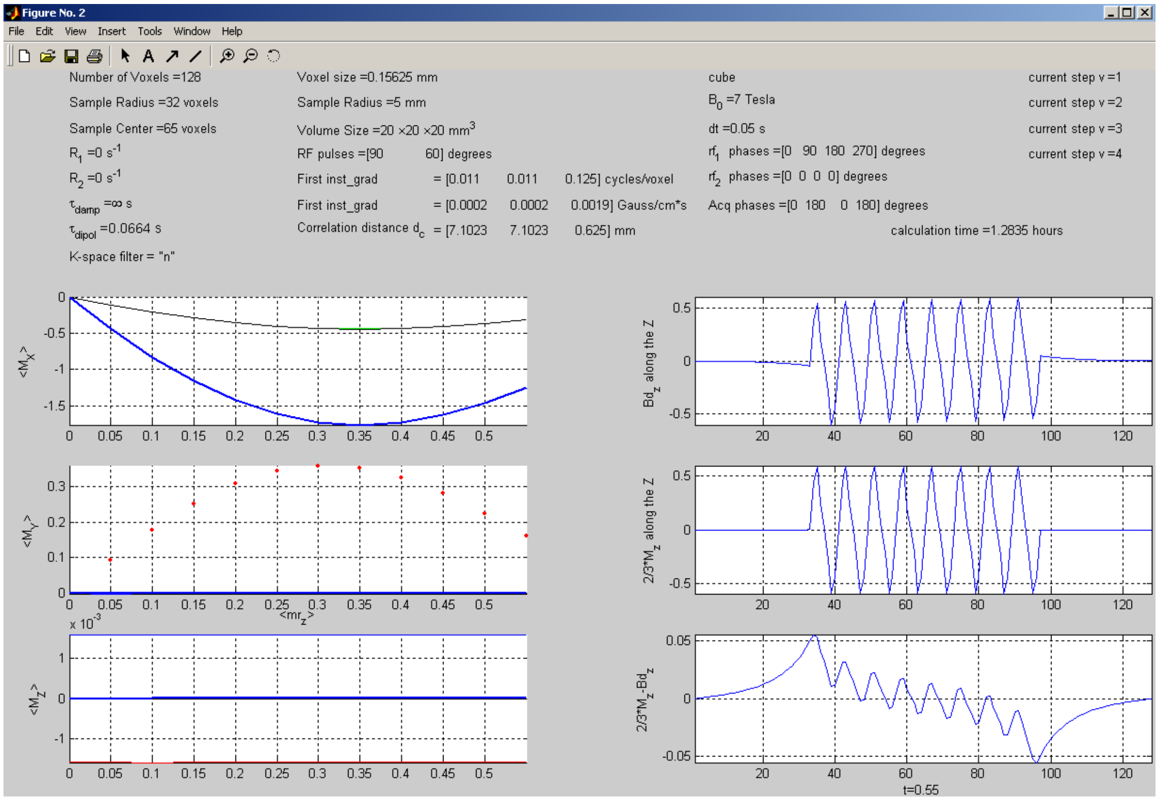

Number of Voxels =128

Sample Radius =32 voxels

Sample Center =65 voxels

R_1 =0 s^{-1}

R_2 =0 s^{-1}

τ_{damp} =∞ s

τ_{dipol} =0.0664 s

K-space filter = "n"

Voxel size =0.15625 mm

Sample Radius =5 mm

Volume Size =20 ×20 ×20 mm^3

RF pulses =[90 60] degrees

First inst_grad = [0.011 0.011 0.125] cycles/voxel

First inst_grad = [0.0002 0.0002 0.0019] Gauss/cm*s

Correlation distance d_c = [7.1023 7.1023 0.625] mm

cube

B_0 =7 Tesla

dt =0.05 s

rf_1 phases =[0 90 180 270] degrees

rf_2 phases =[0 0 0 0] degrees

Acq phases =[0 180 0 180] degrees

calculation time =1.2835 hours

current step v =1

current step v =2

current step v =3

current step v =4

Figure 22: Magnetization evolution under Bloch equation. Phase cycling procedure for the double quantum coherence signal selection is implemented.

The contribution from the zero component is minimal, which has been tested by making deltak = I, where I stands for the unit matrix, and deltak(ctr,ctr,ctr) = 0, where ctr refers to the index of the zero frequency component in K-space, only the slightest deviation from the Bessel function - like behavior was observed.

Phase cycling procedure was implemented to eliminate the effects of the finite sample size and to most closely reproduce the real multiple pulse, multiple pulse phases sequences.

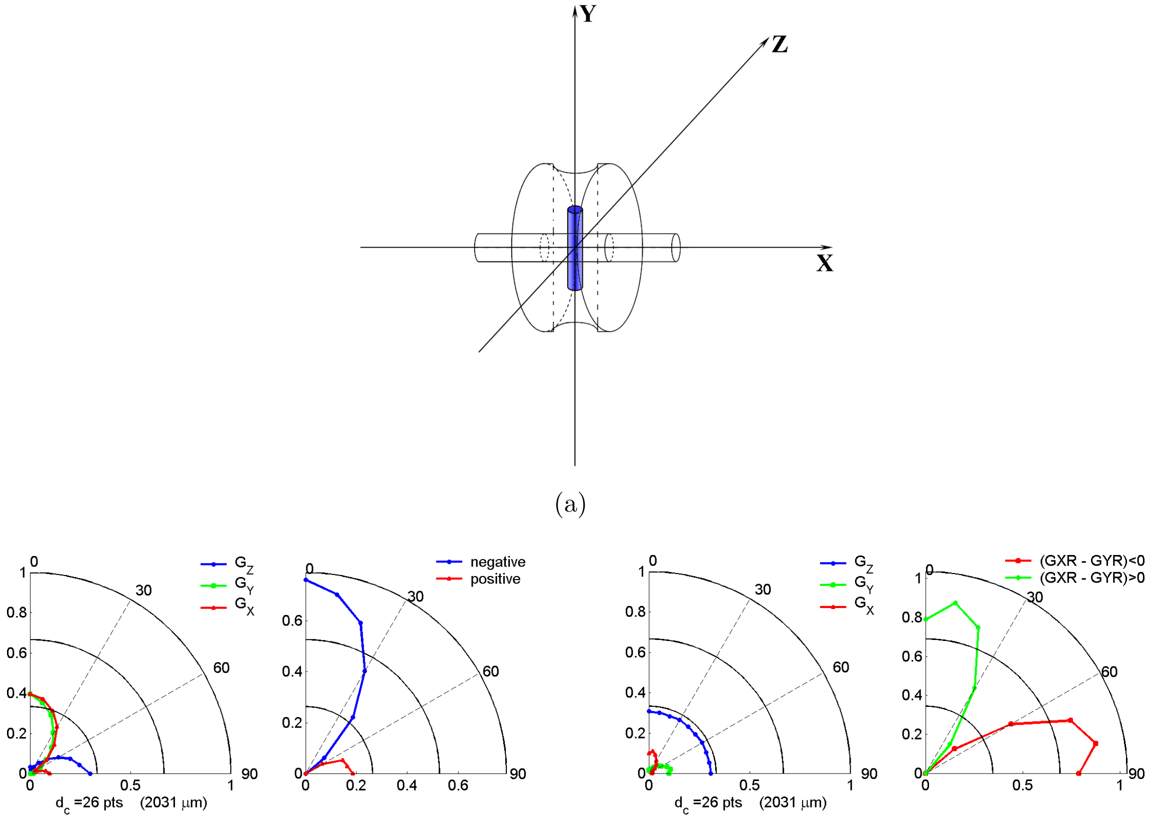

(a)

(b)

(c)

Figure 23: Holder with sample in the magnet reference frame.

Simple phantom simulation data

Numerical simulations have been set to closely reproduce our real experiment and described as follows. Two types of experiments have been made (see Chapter 4 for more details) which are the sample rotation in ZY plane (from Z to Y axis, see Fig.23(b) and rotation in YX plane (from Y to X axis, see Fig.23(c). For all type of rotations the CRAZED gradients were kept along Z, Y, and X axis consecutively.

Fig.23(b) and (c) have two parts. The first part corresponds to the raw data, that is iDQC signal as a function of sample orientation for three different gradient orientations G_Z, G_Y, G_X (see the picture's legend). The second part of each picture represents the raw data processed with the following algorithm. The $Z - Y$ sample

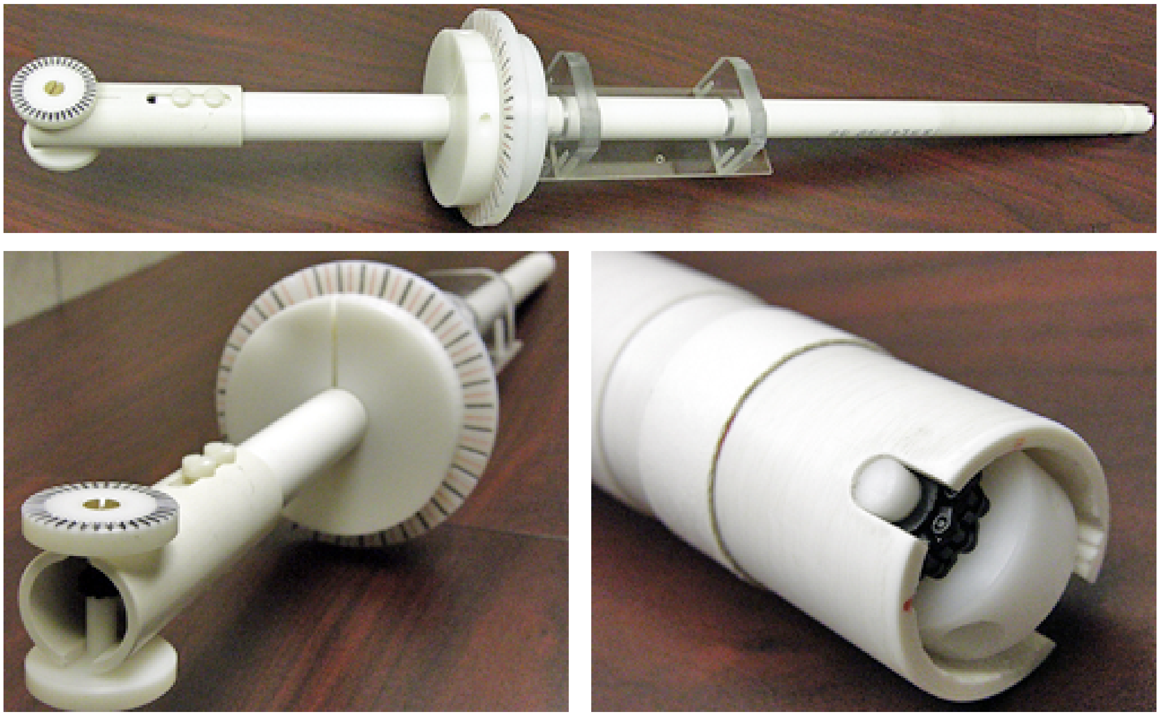

Figure 24: Sample Holder

rotation data presented as $\|G_Z\| - \|G_Y\| - \|G_Z\|$ and the $Y - X$ sample rotation data presented as $\|GXR\| - \|GYR\|$, where $\|G_i\|$ is the magnitude of the signal when the gradient is in the direction i and $\|GXR\|$ and $\|GYR\|$ are normalized in the way described in [47], that is $GXR = 4\|G_X\|/(\|G_X\| + \|G_Y\| + \|G_Z\|)$ and $GYR = 4\|G_Y\|/(\|G_X\| + \|G_Y\| + \|G_Z\|)$. The thick lines are the result of simulations, while the three data set are plotted as thinner lines. Four complete sets of these data are given in Figs.27, 28, 29, 30 at the end of this chapter.

Fig.23(a) displays a basic part of the sample holder, the probe. Through the system of gears and chains it allows us to arbitrarily position the sample (painted blue) in the magnet bore. In the picture the sample is shown oriented along the Y axis, perpendicular to the major axis of the magnet. On Fig.24 we can see an

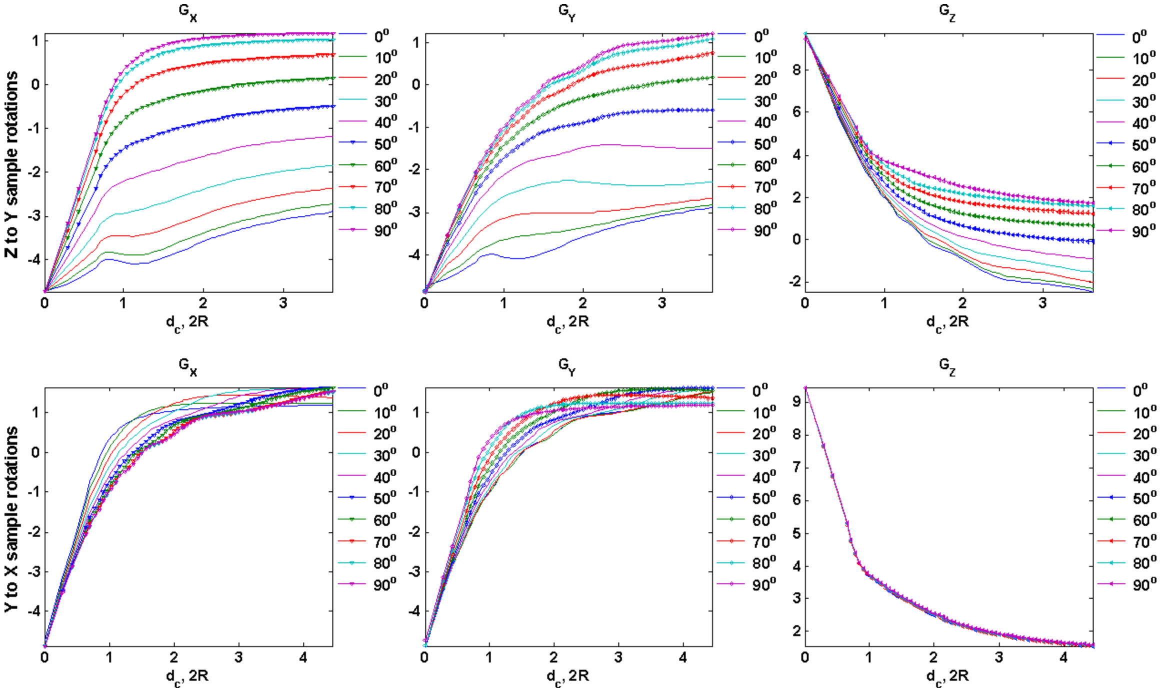

Figure 25: Z to Y and Y to X simulations data as a function of d_c measured in the units of the sample width (2R).

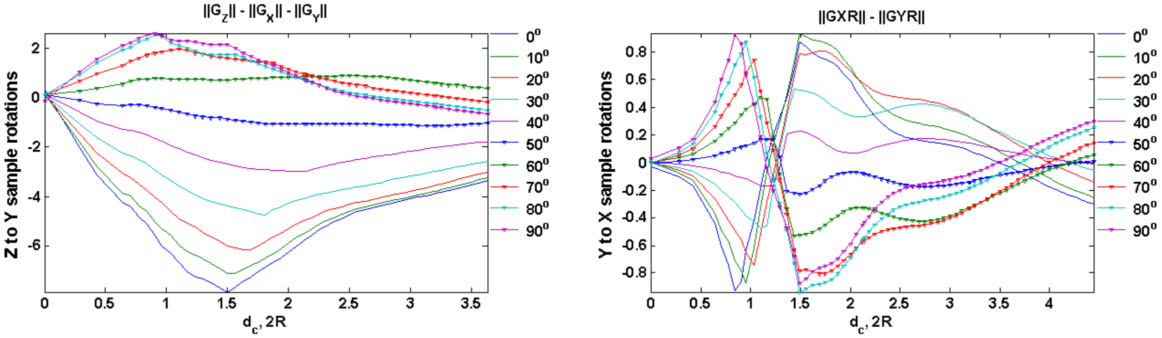

Figure 26: Phantom numerical simulations data plotted with the metrics suggested by Bouchards *et al.* as a function of imposed correlation distance d_c measured in the units of the sample width (2R).

assembled sample holder with the probe head (low right corner), two perpendicular planes rotation knobs and dials (low left corner) and a general view with RF coil mount plate (top).

Figs.25 and 26 is another representation of the numerical simulation data for different sample orientations (given in degrees on the right side of each plot). Fig.25 gives simulation data for $Z-Y$ (top) and $Y-X$ (bottom) rotations as a function of correlation distance d_c in the units of the sample width (2R), for the three gradient directions G_X, G_Y and G_Z and 10 different sample orientations (from 0° to 90° degrees) measured from Z (top raw of the pictures) and Y (bottom raw of the pictures) axis respectively. Fig.26 plots the same correlation distance d_c dependencies only now for the Bouchard *et al.* metrics $\|G_Z\| - \|G_Y\| - \|G_Z\|$ and $\|GXR\|$ and $\|GYR\|$ described earlier.

Determining the CRAZED signal as d_c goes to zero

In the linear approximation, the signal $\vec{S}$ is given by

$$S_i \propto \frac{dM_i}{dt} \propto \left(\vec{M} \times \vec{B}\right)_i = \sum_{\mathbf{r}_l}^{V} \left[M_j(\mathbf{r}_l)B_k(\mathbf{r}_l) - M_k(\mathbf{r}_l)B_j(\mathbf{r}_l)\right], \tag{III.16}$$

where i, j, k refer to the vector components x,y,z and cyclic permutations and the sum includes all discrete elements covering the sample [47].

In the limit $d_c \to 0$, $\vec{B_d}$ takes the following form in real space [2]

$$\vec{B_d}(s) = \mu_0 \triangle_s \left[M_z(s)\hat{\mathbf{z}} - \frac{1}{3}\vec{M}(s)\right], \tag{III.17}$$

with $\triangle_s = \frac{1}{2}\left[3\left(\hat{\mathbf{s}}\cdot\hat{\mathbf{z}}\right)^2 - 1\right]/2$ and $\hat{\mathbf{s}}$ is the unit vector along the gradient direction.

Since $\vec{M} \times \vec{M} = 0$, Eq.(III.16) reduces to

$$\begin{aligned} S_x &= \mu_0 \triangle_s \sum_{\mathbf{r}_l}^{V} M_y(\mathbf{r}_l) M_z(\mathbf{r}_l) \\ S_y &= -\mu_0 \triangle_s \sum_{\mathbf{r}_l}^{V} M_x(\mathbf{r}_l) M_z(\mathbf{r}_l). \end{aligned} \tag{III.18}$$

After the 90_{ϕ_1} RF pulse:

$$\begin{aligned} M_x &= -M_0 \sin(\phi_1) \\ M_y &= +M_0 \cos(\phi_1) \\ M_z &= 0. \end{aligned} \tag{III.19}$$

After first +GT gradient

$$\begin{aligned} M_x &= -M_0 \sin(\phi_1) \cos(ks) + M_0 \cos(\phi_1) \sin(ks) \\ M_y &= +M_0 \cos(\phi_1) \cos(ks) + M_0 \sin(\phi_1) \sin(ks), \end{aligned} \tag{III.20}$$

where $k = \gamma G T$.

Ignoring relaxation and chemical shift, after the 120_0 RF pulse:

$$\begin{aligned} M_x &= [-M_0 \sin(\phi_1) \cos(ks) + M_0 \cos(\phi_1) \sin(ks)] \\ M_y &= [+M_0 \cos(\phi_1) \cos(ks) + M_0 \sin(\phi_1) \sin(ks)] \left(-\frac{1}{2}\right) \\ M_z &= [+M_0 \cos(\phi_1) \cos(ks) + M_0 \sin(\phi_1) \sin(ks)] \left(-\frac{\sqrt{3}}{2}\right). \end{aligned} \tag{III.21}$$

After another +2GT gradient:

$$\begin{aligned}
M_x = \quad & M_0\left[-\sin\left(\phi_1\right)\cos\left(ks\right)+\cos\left(\phi_1\right)\sin\left(ks\right)\right]\cos\left(2ks\right) \\
& +\left(-\tfrac{1}{2}\right)M_0\left[\cos\left(\phi_1\right)\cos\left(ks\right)+\sin\left(\phi_1\right)\sin\left(ks\right)\right]\sin\left(2ks\right) \\
M_y = \quad & \left(-\tfrac{1}{2}\right)M_0\left[\cos\left(\phi_1\right)\cos\left(ks\right)+\sin\left(\phi_1\right)\sin\left(ks\right)\right]\cos\left(2ks\right) \\
& -M_0\left[-\sin\left(\phi_1\right)\cos\left(ks\right)+\cos\left(\phi_1\right)\sin\left(ks\right)\right]\sin\left(2ks\right) \\
M_z = \quad & \left(-\tfrac{\sqrt{3}}{2}\right)M_0\left[\cos\left(\phi_1\right)\cos\left(ks\right)+\sin\left(\phi_1\right)\sin\left(ks\right)\right] \qquad \text{(III.22)}
\end{aligned}$$

For further calculations, we only need to keep those terms that reduce to $\sum\cos(0) = \sum 1$ =volume= V. Terms like $\sum\cos(nks)$ are averaged to 0 in the limit $d_c \to 0$ (and $k_m \to \infty$).

We will need the following trigonometric identities

$$\begin{aligned}
\sin(u)\sin(v) &= \frac{1}{2}\left[\cos(u-v)-\cos(u+v)\right] \\
\cos(u)\cos(v) &= \frac{1}{2}\left[\cos(u-v)+\cos(u+v)\right] \\
\sin(u)\cos(v) &= \frac{1}{2}\left[\sin(u+v)+\sin(u-v)\right] \\
\cos(u)\sin(v) &= \frac{1}{2}\left[\sin(u+v)-\sin(u-v)\right]. \qquad \text{(III.23)}
\end{aligned}$$

The following combinations will produce zero and nonzero terms

$$\cos(2ks)\cos(ks)\cos(ks) = \cos(2ks)\frac{1}{2}\left[\cos(0)+\cos(2ks)\right] \to$$

$$\begin{aligned}
&\frac{1}{2}\cdot\frac{1}{2}\left[\cos\left(0\right)+\cos\left(4ks\right)\right]\rightarrow\frac{1}{4}\\
\cos\left(2ks\right)\cos\left(ks\right)\sin\left(ks\right)=\cos\left(2ks\right)&\frac{1}{2}\left[\sin\left(2ks\right)+\sin\left(0\right)\right]\rightarrow\\
&\frac{1}{2}\cdot\frac{1}{2}\left[\sin\left(4ks\right)+sin(0)\right]\rightarrow 0\\
\cos\left(2ks\right)\sin\left(ks\right)\sin\left(ks\right)=\cos\left(2ks\right)&\frac{1}{2}\left[\cos\left(0\right)-\cos\left(2ks\right)\right]\rightarrow\\
&-\frac{1}{2}\cdot\frac{1}{2}\left[\cos\left(0\right)+\cos\left(4ks\right)\right]\rightarrow-\frac{1}{4}\\
\sin\left(2ks\right)\sin\left(ks\right)\sin\left(ks\right)=\sin\left(2ks\right)&\frac{1}{2}\left[\cos\left(0\right)-\cos\left(2ks\right)\right]\rightarrow\\
&-\frac{1}{2}\cdot\frac{1}{2}\left[\sin\left(4ks\right)+\sin\left(0\right)\right]\rightarrow 0\\
\sin\left(2ks\right)\sin\left(ks\right)\cos\left(ks\right)=\sin\left(2ks\right)&\frac{1}{2}\left[\sin\left(2ks\right)+\sin\left(0\right)\right]\rightarrow\\
&\frac{1}{2}\cdot\frac{1}{2}\left[\cos\left(0\right)-\cos\left(4ks\right)\right]\rightarrow\frac{1}{4}\\
\sin\left(2ks\right)\cos\left(ks\right)\cos\left(ks\right)=\sin\left(2ks\right)&\frac{1}{2}\left[\cos\left(0\right)+\cos\left(2ks\right)\right]\rightarrow\\
&\frac{1}{2}\cdot\frac{1}{2}\left[\sin\left(4ks\right)+sin(0)\right]\rightarrow 0.
\end{aligned}\tag{III.24}$$

Thus, substituting Eq.III.22 to Eq.III.18, we end up with

$$\begin{aligned}
S_x=-\frac{\sqrt{3}}{2}M_0^2\mu_0\triangle_s V\bigg[&\left(-\frac{1}{2}\right)\left(\frac{1}{4}\right)\cos^2\left(\phi_1\right)+\left(-\frac{1}{2}\right)\left(-\frac{1}{4}\right)\sin^2\left(\phi_1\right)\\
&-\left(\frac{1}{4}\right)\left(-\sin^2\left(\phi_1\right)\right)-\left(\frac{1}{4}\right)\cos^2\left(\phi_1\right)\bigg]=\\
&=\frac{3\sqrt{3}}{16}M_0^2\mu_0\triangle_s\cos\left(2\phi_1\right)V
\end{aligned}\tag{III.25}$$

and

$$S_y = +\frac{\sqrt{3}}{2} M_0^2 \mu_0 \triangle_s V \Bigg[\left(\frac{1}{4}\right)\left(-\frac{1}{2}\right)\sin{(2\phi_1)} + \left(-\frac{1}{4}\right)\left(\frac{1}{2}\right)\sin{(2\phi_1)}$$
$$+\left(-\frac{1}{2}\right)\left(\frac{1}{4}\right)\left(\frac{1}{2}\right)\sin{(2\phi_1)} + \left(-\frac{1}{2}\right)\left(\frac{1}{4}\right)\left(\frac{1}{2}\right)\sin{(2\phi_1)}\Bigg] =$$
$$= -\frac{3\sqrt{3}}{16} M_0^2 \mu_0 \triangle_s \sin{(2\phi_1)} V. \qquad \text{(III.26)}$$

Finally, after applying phase cycling procedure, see Table 2

Table 2: S$_x$ and S$_y$ values after application of the 4 part phase cycling scheme.

ϕ_1	acq	$S_x,\ \frac{3\sqrt{3}}{16} M_0^2 \mu_0 \triangle \sum_{\mathbf{r}_l}^{V} 1$	$S_y,\ -\frac{3\sqrt{3}}{16} M_0^2 \mu_0 \triangle \sum_{\mathbf{r}_l}^{V} 1$
0	0	1	0
90	180	1	0
180	0	1	0
270	180	1	0
	$\sum =$	4	0

$$S_x = \frac{3\sqrt{3}}{4} M_0^2 \mu_0 \triangle_s V, \quad S_y = 0. \qquad \text{(III.27)}$$

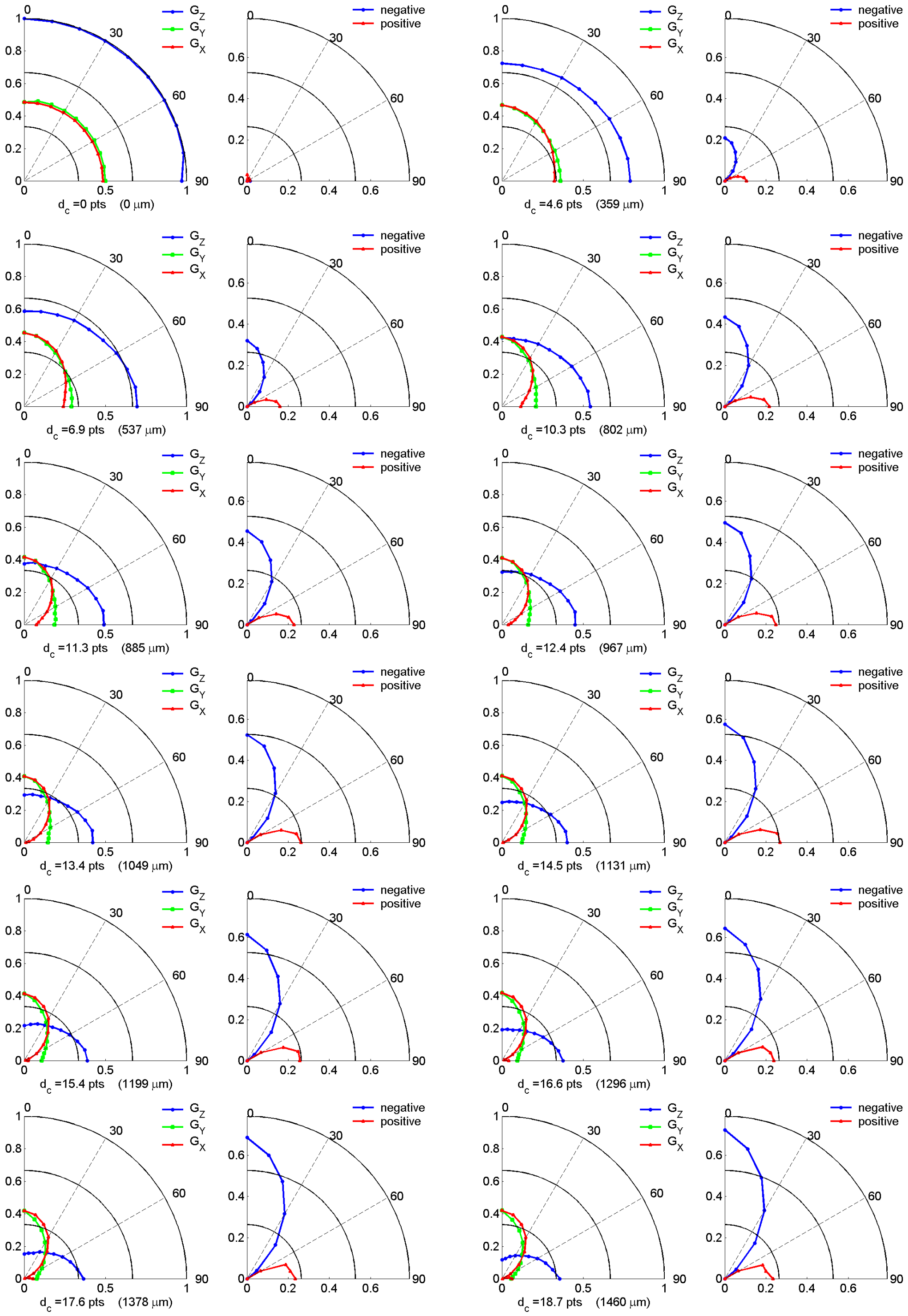

Figure 27: Z to Y. Set 1

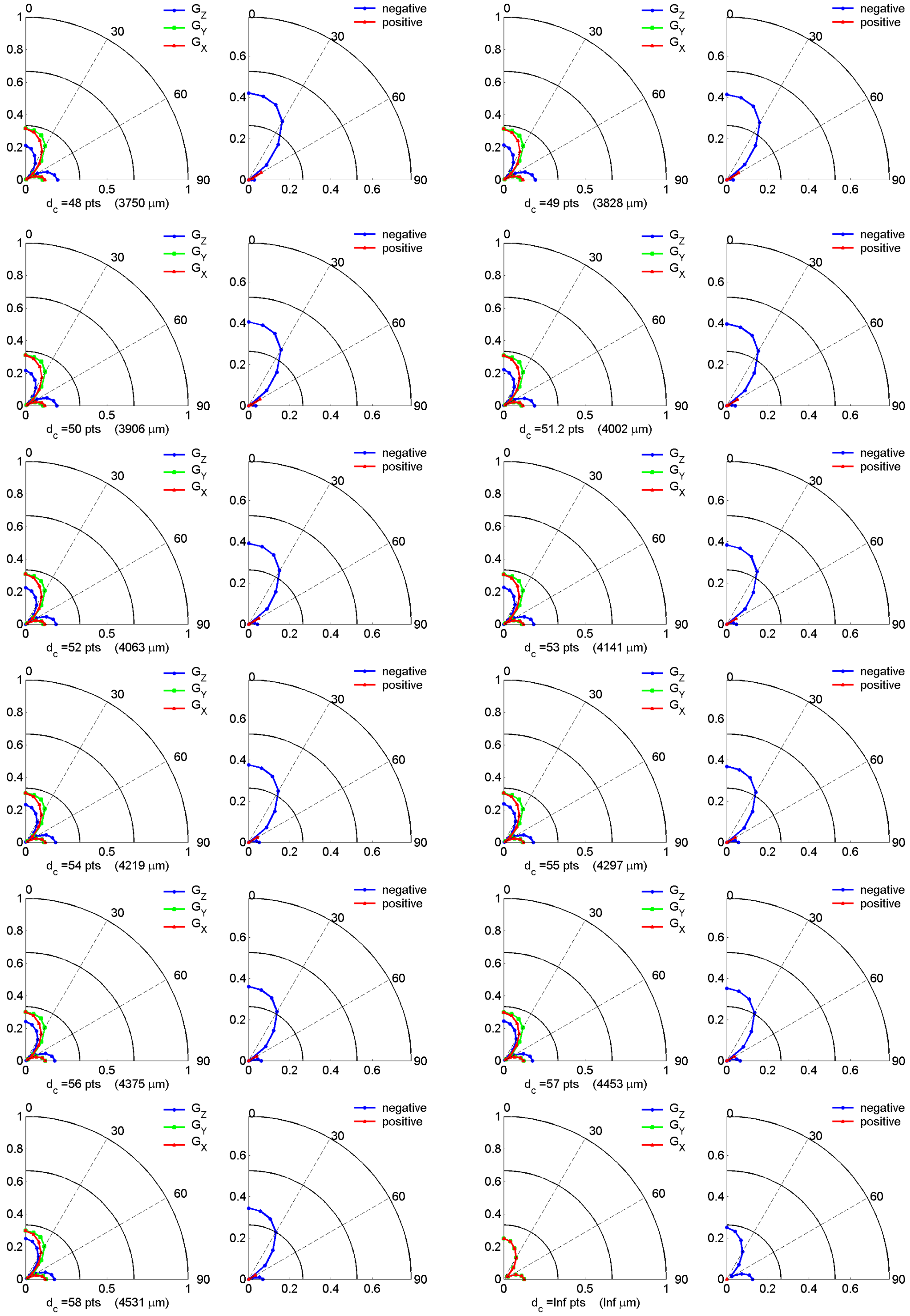

Figure 28: Z to Y. Set 2

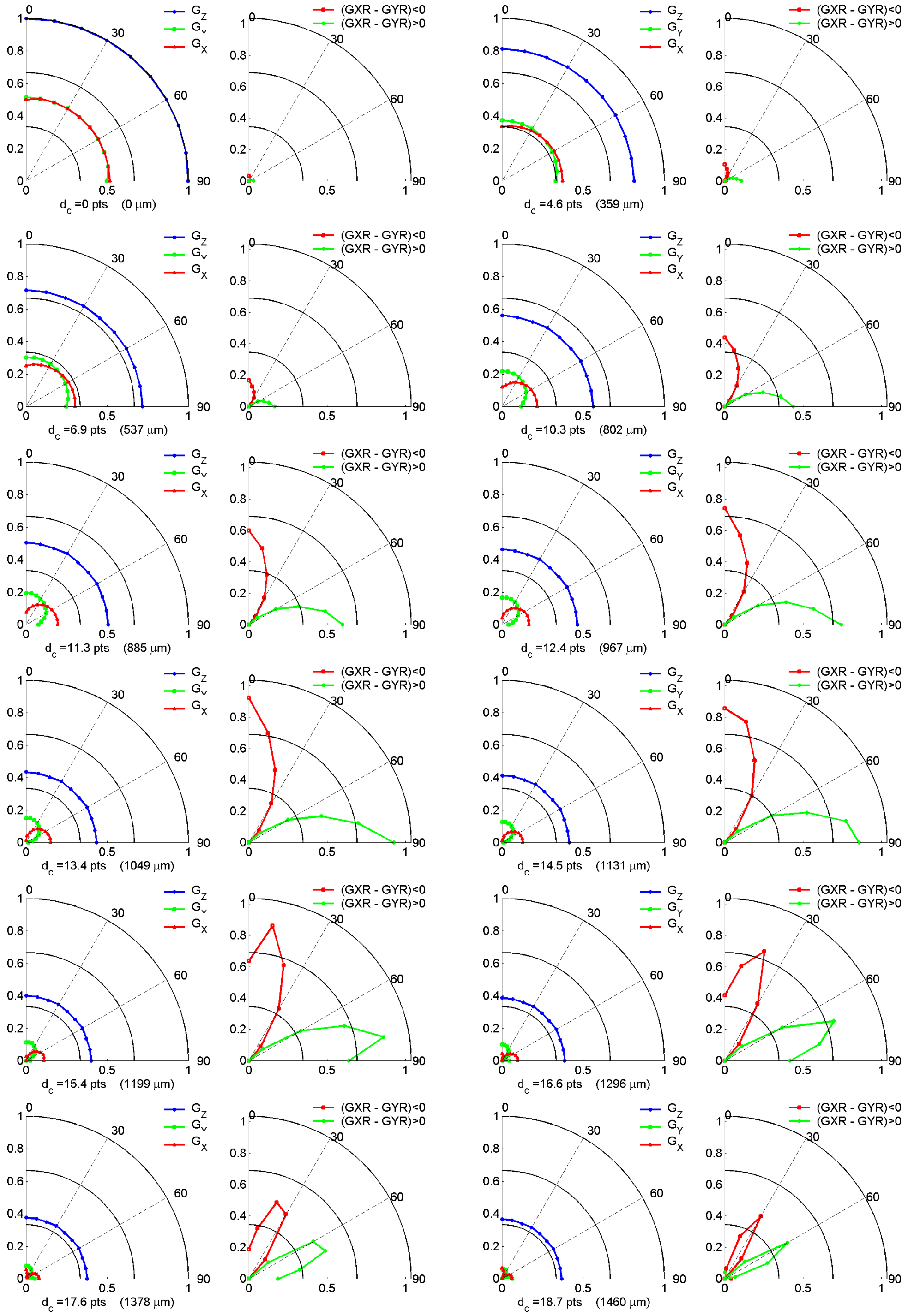

d_c =0 pts (0 μm)

d_c =4.6 pts (359 μm)

d_c =6.9 pts (537 μm)

d_c =10.3 pts (802 μm)

d_c =11.3 pts (885 μm)

d_c =12.4 pts (967 μm)

d_c =13.4 pts (1049 μm)

d_c =14.5 pts (1131 μm)

d_c =15.4 pts (1199 μm)

d_c =16.6 pts (1296 μm)

d_c =17.6 pts (1378 μm)

d_c =18.7 pts (1460 μm)

Figure 29: Y to X. Set 1

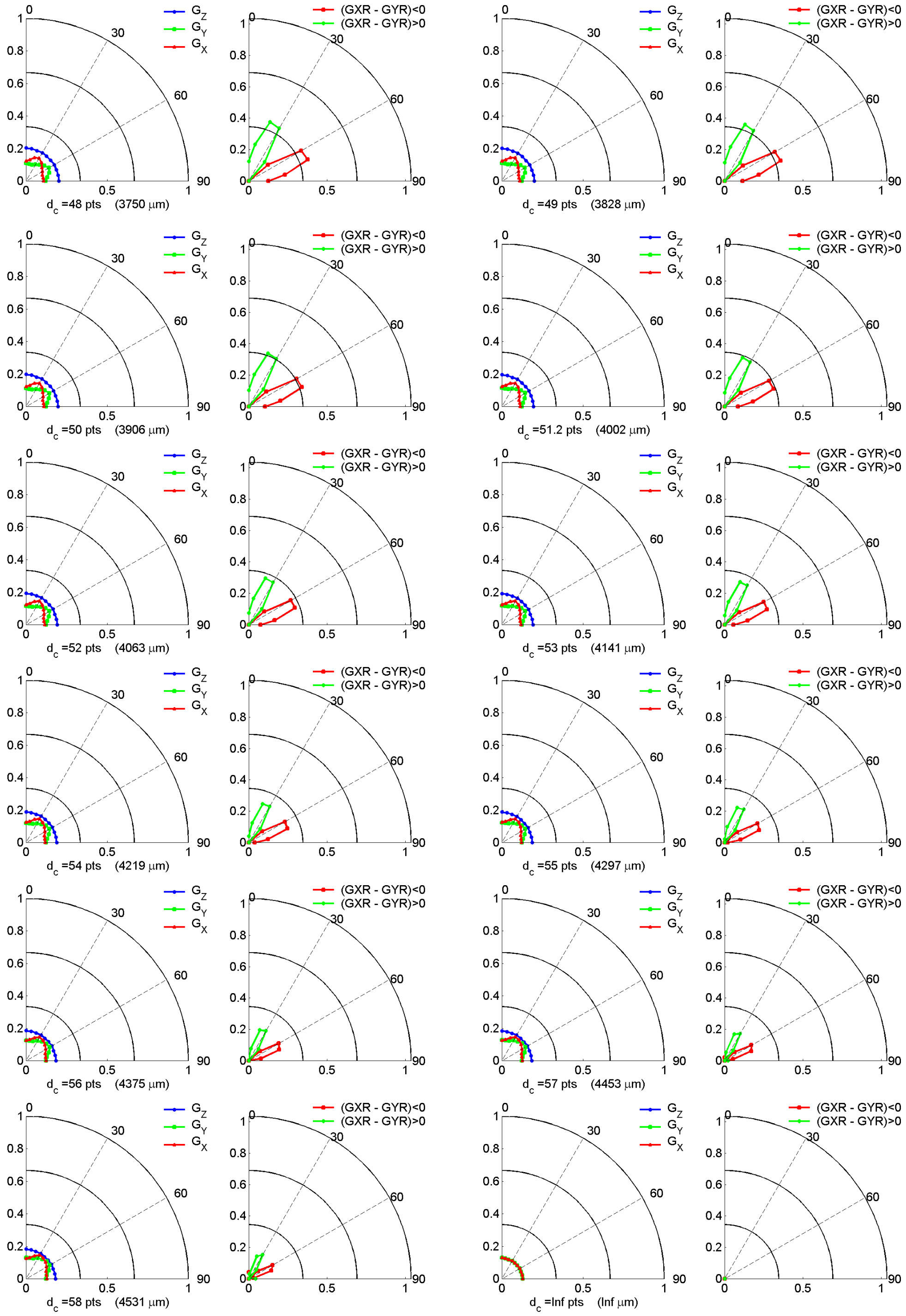

Figure 30: Y to X. Set 2

CHAPTER IV

RAT SCIATIC NERVE CRAZED STUDIES

Introduction

We measured the CRAZED signal from ex vivo rat sciatic nerve while varying the sample orientation and the gradient induced correlation distance, and we compared these results to a doped water cylindrical sample of the same size but lacking any internal structure. The results for the doped water sample are in good agreement with numerical simulations of the dipole-dipole interactions in a uniform cylinder for correlation distances ranging from 4 mm to 32 μm. These results indicate that the relation between the measured signal and the induced correlation distance is highly dependent on the sample and gradient orientation, thereby limiting the interpretability of CRAZED measurements that vary only the correlation distance. The results for the sciatic nerve are more difficult to interpret, but have characteristics indicative of cylinders at both the ten and hundreds of micrometers distance scales, reflecting both axon and the tibial/peroneal fascicle structures that compose the nerve. These results support the view that CRAZED methods are able to probe a range of distance scales not available in other magnetic resonance methods.

Conventional magnetic resonance imaging is typically limited to resolutions of 100's of micrometers in small animals and to millimeters in humans. Diffusion and diffusion tensor measurements [48] provide information on subvoxel structures (averaged over the voxel dimensions) on the roughly 10 μm distance scale; hence its wide utilization in studies of axons. While diffusion tensor studies have been used to track large ($\sim$50 μm) cell orientations in muscle fibers [49], it is the parallel subvoxel structures on the μm scale that inhibit the water diffusion. No single conventional magnetic resonance method probes both the micrometer and millimeter distance scales or an intermediate scale ($\sim$ 50–300 μm) between diffusion measures and direct imaging [50].

The CRAZED (COSY revamped with asymmetric z-gradient echo detection) [19] pulse sequence, based on the long range dipole-dipole interactions [2], has a structural sensitivity determined by the applied gradients. Specifically, the correlation distance $d_c = \pi/\gamma G T$ dictates the distance scale of the signal sensitivity to magnetization variations, where G is the applied gradient amplitude with duration T (see Fig.31). As such, the CRAZED signal provides a means for probing the intermediate scale as well as providing a single consistent method for probing structures at all scales. The relationship between d_c, magnetization variations, and the measured signal, however, is not trivial.

Numerous attempts have been made to establish this relationship numerically, analytically, and experimentally. The principle of tuning experiment sensitivity to the distance scale was proposed by Warren *et al.* [19] for solutions of proteins. The signal was shown to originate predominantly from spins separated by one-half turn of the magnetization helix. Richter *et al.* examined the sensitivity to the strength of imposed magnetization modulation/helix pitch and its direction, and the existence of resolution limits imposed by diffusion for parallel cylinders of varying content [28]. P. Robyr and R. Bowtell [29] developed a Fourier-space formalism to explain experimental data from coaxial cylinders. Follow-up studies of the same group include modeling the signal dependence on the size of randomly packed polystyrene microspheres and the imposed magnetization modulation at the tens of micrometers scale [33], and directly imaging the signal variation as a function of the distance from the center of a cylinder [6]. Tuning the correlation distance while imaging arrays of hollow cylinders and straws, L.-S. Bouchard *et al.* reported DDF specific contrast variations for complex structures when d_c was on the order of the gap between these cylinders [34]. S.M. Brown *et al.* extracted the average bubble size distribution of the oil fraction in a water/oil emulsion [51], and S. Capuani *et al.* examined pore size in trabecular bone and travertine [52, 53]. Biological specimens studied with CRAZED include trabecular bone [36, 37],human brain [38, 39, 54], tendons [55] and cartilages like pig [56, 57] and mouse tails [58], earthworms and grapes pumped with nanoparticles [59].

Recently, Bouchard and Warren [47] demonstrated that the CRAZED signal of a cylindrical sample has a dependence on the sample orientation, suggesting a method for non-invasive mapping of fiber orientation in materials and biological tissues. However, they were not able to determine the axis orientation absolutely, but only relative to a known initial condition, by measuring the CRAZED signal along three perpendicular gradient directions before and after a sample rotation. Also, while they demonstrated a clear dependence of the signal on the correlation distance relative to the sample size, the exact nature of this dependence is unclear. In this work, we address these issues of CRAZED signal dependence on sample orientation and the gradient induced correlation distance in sciatic nerve and cylindrical phantoms with the goal of determining what size information can be gained from the CRAZED signal.

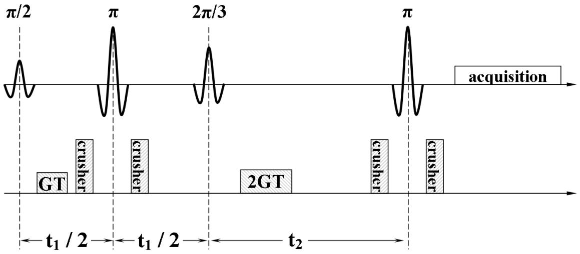

Figure 31: CRAZED pulse sequence

Methods

We have focused on peripheral sciatic nerve as a test case due to its relatively simple geometry, ignoring that its microstructures (though not its macrostructures) may be best measured via diffusion methods. Rat sciatic nerve is composed of cylindrical structures at the micrometer (axons), 100s of micrometers (fasciculi), and millimeter (nerve) distance scales. The nerve originates as one unit from the lumber spinal regions L4-L6, splits into the tibial and peroneal fascicles separated by a septum, then more distally at the point of our dissection, the tibial and peroneal fascicles are two bundles extending together as the sciatic nerve, approximately 0.4 mm in diameter, before they completely separate [60, 61].

Samples

Two sample types were measured: 1) a plastic tube 5.94±0.10 mm long and 1.25±0.10 mm in diameter filled with an aqueous $CuSO_4$ doped (1 g/L) water and 2) rat sciatic nerve prepared as described below.

A total of five male and five female Sprague Dawley rats weighing from 300 to 450 grams were used for this study. Immediately after animal sacrifice, the two sciatic nerves from the right and left leg were excised. Any residue of connective tissue was removed, taking care to avoid damaging the nerve. Two or three pieces, depending on the nerve condition and size, each trimmed to 8.0 mm length, were placed one on the top of another in a special sample holder and covered with perfluoropolyether vacuum oil (Fomblin 06/6, Solvay Solexis, Thorofare, NJ). Slight pressure applied after wrapping it with the polyethylene film (Great Value $^{\mathrm{TM}}$, Wal-Mart Inc, Bentonville, AR, USA) gives it proper compact cylindrical shape (1.8 mm wide) and preserved it from drying. This fluorinated oil is biologically and chemically inert, produces no NMR signal, and used in our case to avoid drying. Finally this sample was inserted within a 5 mm diameter fiberglass tube and placed in a custom made sample holder capable of sample positioning at arbitrary position and plane within the coil fixed in the magnet (see Fig.24).

All procedures were performed in accordance with AVMA Guidelines on Euthanasia and endorsed by the Vanderbilt University Institutional Animal Care and Use Committee.

CRAZED gradient values $G = [0.0489\ 0.1632\ 0.5441\ 1.8139\ 6.0595\ 20.0000]$ G/cm were chosen on a logarithmic scale. These gradients of length $T = 6$ ms each correspond to correlation distances $d_c = [4002\ 1199\ 359.7\ 107.9\ 32.30\ 9.786]$ μm.

The double quantum period has the same duration $t_1 = 17$ ms for both samples, while t_2 takes values of 65.5 and 20.6 ms for the water and nerve sample respectively. The acquisition window is centered around the double quantum echo and $TR = 5$ s.

Data Acquisition

Experimental data were acquired on a 7 Tesla 16-cm horizontal bore Varian Inova (Varian Inc., Palo Alto, CA, USA) scanner system running at 300 MHz and using a 25 mm diameter and 22 mm long Litz coil from Doty Scientific,Columbia, SC, USA.

A spectroscopic CRAZED sequence with a double quantum filter was implemented with four part phase cycling of the first pulse and receiver (see Fig. 31). After the first 90° pulse, magnetization is flipped into the YX plane and is spatially modulated along the gradient G direction during time T. The 120° pulse rotates part of this modulation back along the Z axis. After application of the second CRAZED gradient, twice as long as the first one, the dipolar field refocuses the magnetization during the acquisition time . Two 180° pulses are used to refocus magnetic field inhomogeneity. All pulses used in the sequence were adiabatic BIR-4. The first pulse and the acquisition were cycled with with phases 0, 90, 180, 270 and 0, 180, 0, 180, respectively, in order to select for double quantum coherences during t_1.

Both the water and nerve samples were rotated over a 90° arc in 10° steps (controlled by a custom made device). Rotation within a single plane takes on the order of 2.5 hours. At every step, sample positioning was confirmed via gradient echo imaging.

Histology and electron microscopy were performed to assess the underlying structures of the sciatic nerve and to determine the extent of degeneration during the CRAZED measurements. Sciatic nerve excised from the left leg was immediately fixed in 4% glutaraldehyde in 0.05M PBS overnight. Nerve from the right leg was alowed to sit for 3 hours in the magnet, in the sample holder, and then fixed in the same manner. Samples were transferred to 1% OsO_4 in PBS plus 1.5% $K_3Fe(CN)_63H_2O$

for 3 hours, washed in PBS, then stained *en bloc* with 1% uranyl acetate . After serial EtOH dehydrations, samples were passed through propylene oxide before transition to araldite resin in a vacuum oven. Ultra thin (60-70 nm) cross sections of sciatic nerves were examined on a Phillips CM10 TEM equipped with an AMT 2 mega-pixel camera. Thick sections (∼100 nm) were stained with toluidine blue and light photomicrographs were obtained on an Olympus microscope with a DP70 camera. All measurements were performed at the room temperature of 20°C.

Numerical Simulations

The water sample was simulated by a uniform cylinder 76 pts long and 16 pts wide with the M_z component set equal to one. The size of the simulation volume was 256 pts×256 pts×256 pts. Treating these dimensions as corresponding to a 2 cm×2 cm×2 cm cube in the real space we'll end up with the phantom 1.25 mm wide and 5.94 mm long, which matches the measured water sample.

The dipolar field was calculated via the methods of Enss *et al.* [7] and ignoring the zero spatial frequency component. Relaxation, diffusion, and field inhomogeneity were ignored, and a linear approximation to the signal was made. The method is well described elsewhere [47, 42] and is based on a discrete form of the DDF signal of the form of $S_i = \sum M_j\left(\mathbf{r}\right)B_k\left(\mathbf{r}\right) - M_k\left(\mathbf{r}\right)B_j\left(\mathbf{r}\right)$. Where i, j and k represent cyclic variations of x,y,z and summation is made over the all sample elements on the simulation grid. These approximations allow a simplified pulse sequence without refocusing pulses and with each segment performed instantaneously: $(\pi/2 - GT - 2\pi/3 - 2GT - acquisition)$. A four part phase cycling scheme $\phi_{\pi/2}$=[0 , $\pi/2$, π , $3\pi/2$]

and ϕ_{acq}=[0 , π , 0 , π] was implemented.

The minimum d_c is determined by the finite simulation grid spacing. We maintained ≥8 points per helix cycle, well above the low limit of 4 points per helix cycle in [7]. In addition, the signal when $d_c = 0$ was calculated analytically (as outlined in the appendix) to be $S_x = \frac{3\sqrt{3}}{4} M_0^2 \mu_0 \triangle_s V$.

Two types of rotations were made in full accordance with the experiment: one in the ZY plane, in 10 degree steps from along the Z axis ($\theta_{grad} = 0°$) to the Y axis ($\theta_{grad} = 90°$), and one in the YX plane, starting aligned along the Y axis ($\phi_{grad} = 0°$) to along the X axis ($\phi_{grad} = 90°$).

All simulations were performed using MATLAB®R2006b(73) (MathWorks, Natick, MA, USA) software package, running under RedHat Enterprise Linux-WS v4 OS (Red Hat, Inc, NC, USA) on a Dual Intel®XEON™, CPU 2.20 GHz with 3.5 Gb RAM and 80 Gb ATA HD of the local storage.

Results

Fig.32 illustrates the histology results. The electron micrograph of a sciatic nerve cross section in Fig.32a reveals the underlying ∼10 μm axon structure, while Fig.32b demonstrates that these structures are preserved during the 3 hour measurements. Pressure to the nerve from excision, handling, and placement into the sample holder can on occasion lead to regional compression artifacts [62], specifically changes in myelin shape while still preserving the roughly 10 μm fiber size (data not shown). Also, after 3 hours postexcision, axons and myelinating Schwann cells undergo degeneration; however, as illustrated in Fig.32b, all fibers remain intact, and the inevitable

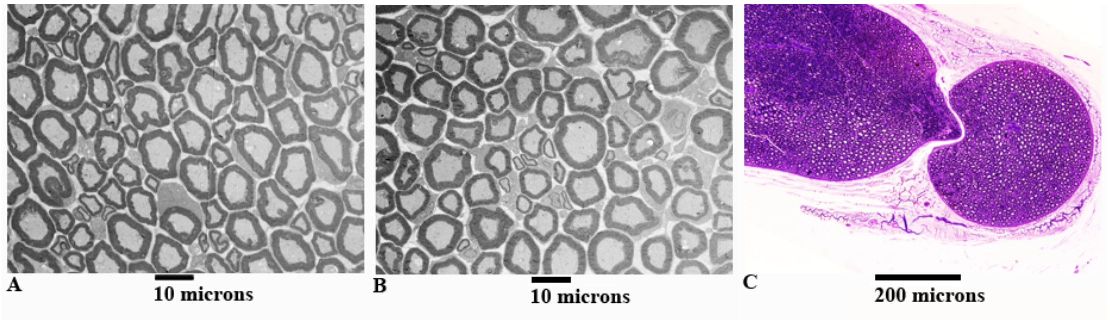

Figure 32: Histology of rat sciatic nerve cross sections. (a), (b) Electron micrographs reveal the 10 μm structures corresponding to myelinated axons. There is no discernible difference in fiber structures between (a) sciatic nerve fixed immediately upon dissection or (b) fixed after 3 hours post-excision. (c) Light microscopy of toluidene blue stained sciatic nerve show the peroneal (smaller) and tibial (larger) fascicles that make up the sciatic nerve.

changes to the myelin ultrastructure and degradation of proteins and mitochondria do not appear to effect our measurements. Both types of changes occur on a scale smaller than our minimal d_c=10μm. Fig. 2c. reveals the $\sim$ 400 μm structure of tibial and peroneal fascicles, which make up the sciatic nerve. The CRAZED results described below also indicate cylindrical structures on the $\sim$10 and $\sim$400 μm scale.

Fig.33 plots a typical result for the water sample data and simulations. The first two columns correspond to $Z-Y$ sample rotation data and simulations, respectively. The third and forth columns correspond to $Y-X$ sample rotation data and simulations, respectively. Each row corresponds to a different induced correlation distance. The $d_c = 0$ and ∞ cases could not be experimentally measured due to finite gradient strength and single quantum contamination, respectively. The results at 10 μm have little signal due to severe diffusion damping [63] and are not shown.

Fig.34 plots the results for the water sample data and simulations again, but with the $Z-Y$ sample rotation data presented as $\|G_Z\| - \|G_Y\| - \|G_Z\|$ and the $Y-X$ sample rotation data presented as $\|GXR\| - \|GYR\|$, where $\|G_i\|$ is the magnitude

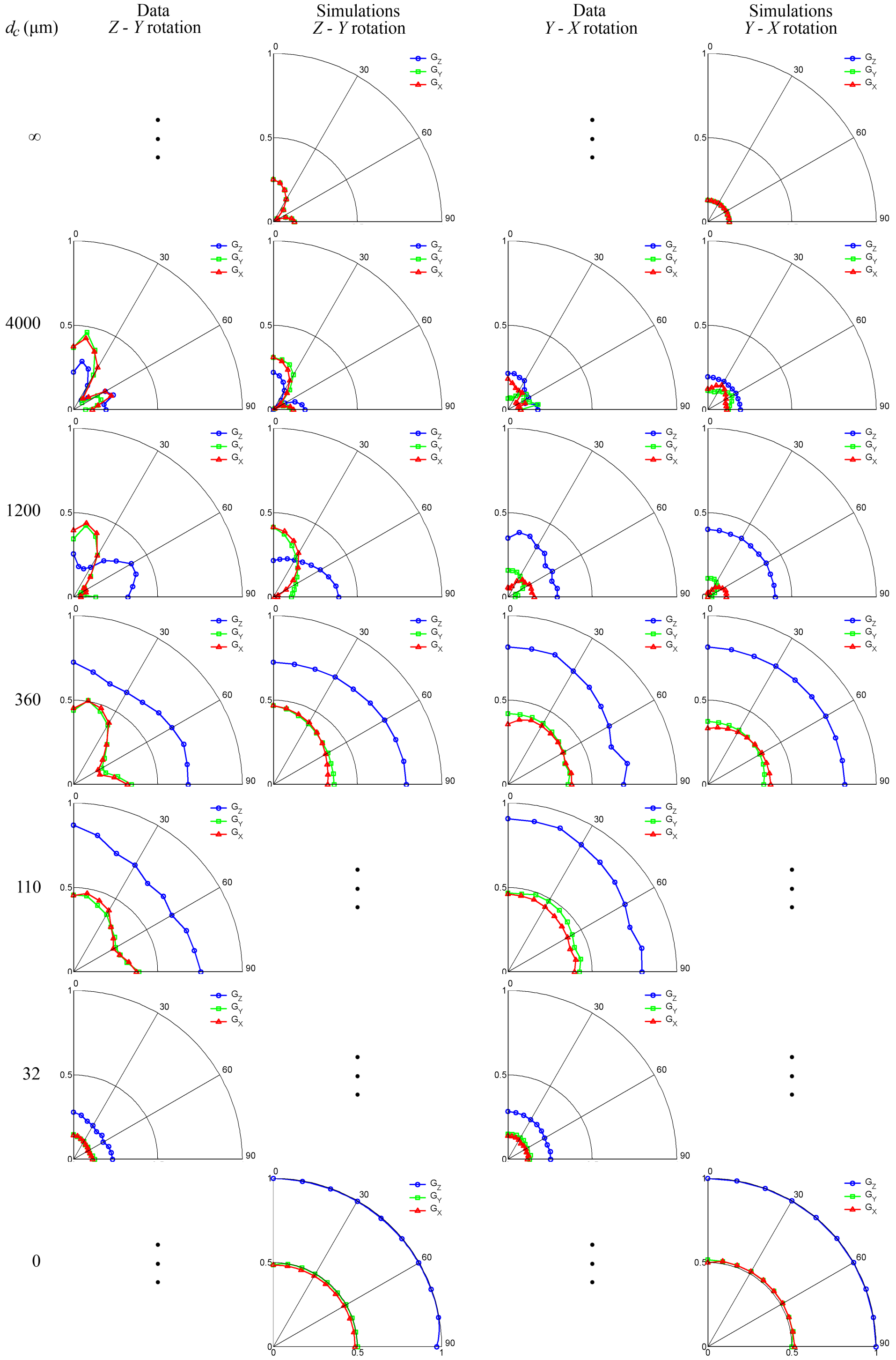

Figure 33: Water sample data and simulations of $Z-Y$ and $Y-X$ sample rotations, with the applied gradient in three directions (G_X, G_Y, G_Z) and with correlation distance values d_c=[0 32 110 360 1200 4000 ∞] μm. The polar angle represents the sample orientation in the $Z-Y$ or $Y-X$ planes. Each row represents a different d_c. The three dots represent missing data due to limited gradient strength ($d_c = 0$) and single quantum contamination ($d_c = \infty$) or missing simulations due to the finite grid resolution (d_c = 32 and 110 μm). Note the strong agreement between simulations and the data for this unstructured sample. Note also that as $d_c \to \infty$, the signal depends only on the sample orientation, and as $d_c \to 0$ the signal depends only on the applied gradient direction.

of the signal when the gradient is in the direction i and $\|GXR\|$ and $\|GYR\|$ are normalized in the way described in [47], that is $GXR = 4\|G_X\|/(\|G_X\| + \|G_Y\| + \|G_Z\|)$ and $GYR = 4\|G_Y\|/(\|G_X\| + \|G_Y\| + \|G_Z\|)$. The thick lines are the result of simulations, while the three data set are plotted as thinner lines.

Fig.35 plots the results for the peripheral nerve measurements. The first two columns correspond to $Z-Y$ sample rotation data plotted for each gradient direction and the calculated $\|G_Z\| - \|G_X\| - \|G_Y\|$, respectively. The third and forth columns correspond to $Y-X$ sample rotation data plotted for each gradient direction and the calculated $\|GXR\| - \|GYR\|$, respectively.

Discussion and Conclusions

Water sample

Fig. 33 plots the water sample data and cylinder simulations. There are several notable results.

There is strong agreement between the measured data and the simulations. This result supports the approach of Enss *et al.* [7] in simulating the CRAZED signal, even when ignoring relaxation and diffusion effects and taking a linear approximation to the signal. Note that at shorter correlation distances (e.g. 30 μm), diffusion effects damp the signal in this unstructured sample (At $d_c = 10\mu m$, there is very little remaining signal, and we have therefore not included results at this distance in Fig.33).

The relation between the measured signal and the induced correlation distance

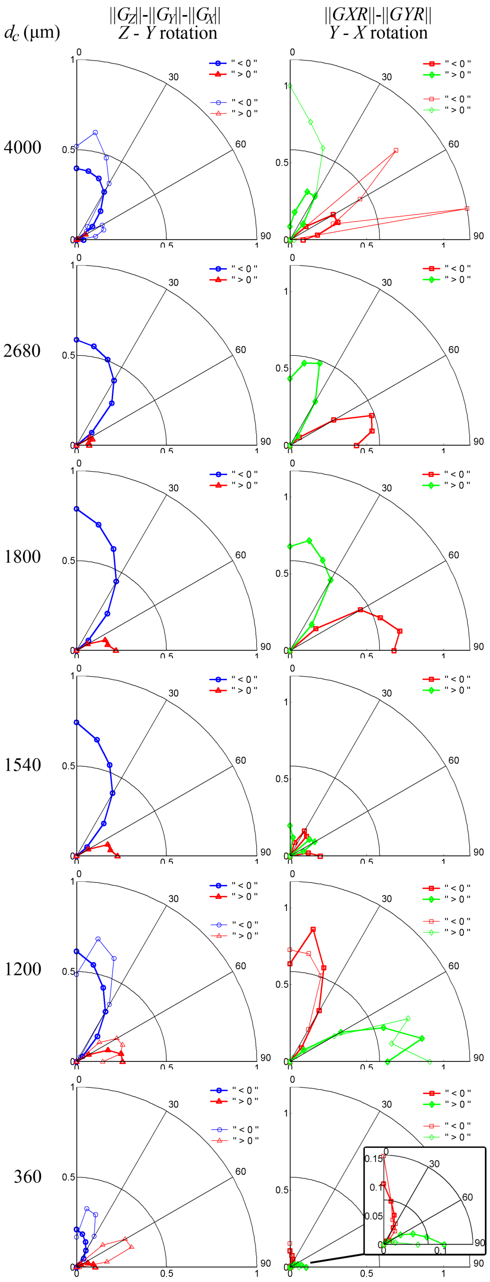

Figure 34: Cylinder simulations (thick lines) and water sample data (thin lines) dependence on sample orientation. The difference signal $\|G_Z\| - \|G_X\| - \|G_Y\|$ approximates $3\cos^2\theta_{sample} - 1$ for $Z - Y$ rotations at correlation distances less than or equal to the cylinder diameter (1250 μm). Likewise, $\|GXR\| - \|GYR\|$ approximates $2\cos^2\phi_{sample} - 1$ for $Y - X$ rotations in the same regime. Note also that $\|GXR\| - \|GYR\|$ flips sign when d_c is near the cylinder diameter (1250 μm).

is highly dependent on the sample and gradient orientation. This dependence on the gradient direction and sample orientation greatly limits the interpretbility of CRAZED measurements that only vary the correlation distance [34, 36, 59, 32], such

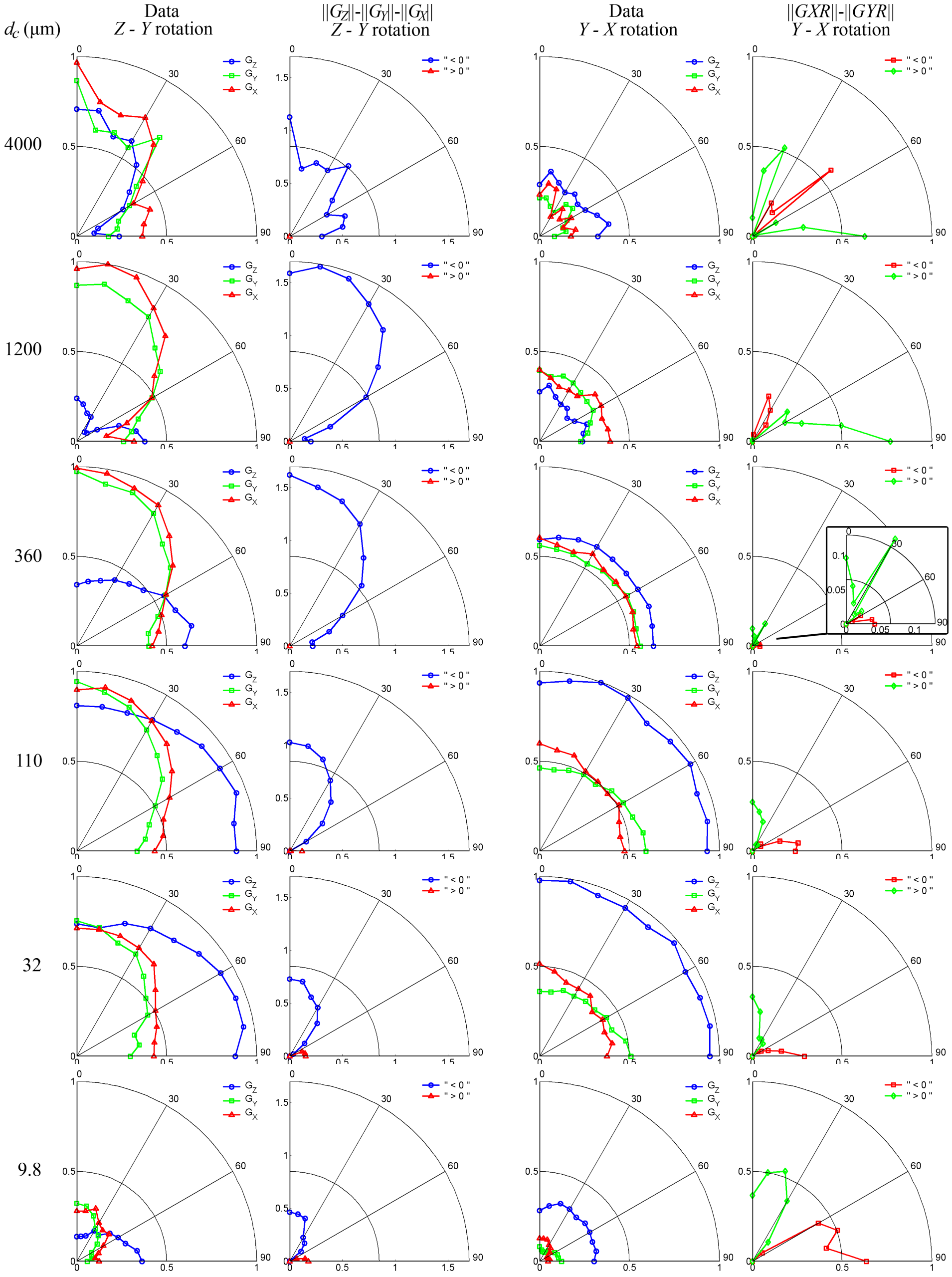

Figure 35: Nerve sample. Correlation distance values d_c=[9.8 32 110 360 1200 4000]μm. The first two columns are $Z-Y$ nerve sample rotations, with column 1 plotting the data directly, and the column 2 plotting $\|G_Z\|-\|G_X\|-\|G_Y\|$. Columns 3 and 4 are corresponding $Y-X$ sample rotations. Note the $3\cos^2\theta_{sample}-1$ (for column 2) and $2\cos^2\phi_{sample}-1$ (for column 4) signal dependence at small d_c values, and the sign flip in $\|GXR\|-\|GYR\|$ at $d_c=360$ μm

as those outlined in the introduction.

As $d_c \to \infty$, the signal depends only on the sample orientation. With the gradient magnitude equal to zero, there can obviously be no dependence on the gradient

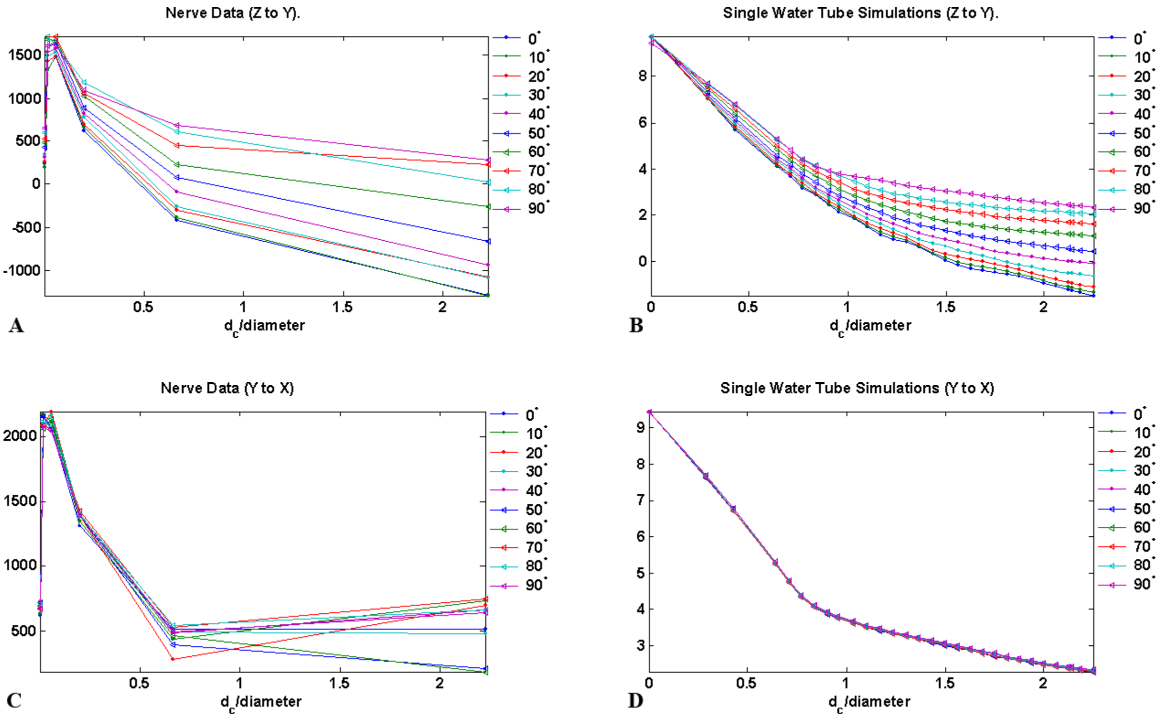

Figure 36: Nerve data (A and C) and water simulations (B and D) as a function of d_c (in units of the corresponding sample diameters), with gradients in the Z direction. Each line represents a different sample orientation. The key points are that 1) the sample orientation affects the signals' d_c dependence, and 2) that the overall shape of the d_c dependence is indicative of the gross sample size and not the underlying microstructure.

orientation. The $3\cos^2\theta_{sample} - 1$ dependence on the sample orientation is due to the dominance of spin interactions along the cylinder axis in the signal averaged over the sample.

As $d_c \rightarrow 0$ the signal depends only on the applied gradient direction, and varies like $3\cos^2\theta_{grad} - 1$. As the gradient induced oscillation length shrinks, all sample structures become (relatively) large and the sample appears homogeneous. Sample orientation then does not matter.

Fig. 34 plots the results for the water sample data and simulations again, but presented in terms of signal differences. Bouchard *et al.* [47] investigated sample orientation using $\|G_Z\| - \|G_X\| - \|G_Y\|$ for $Z - Y$ rotations and $\|GXR\| - \|GYR\|$ for

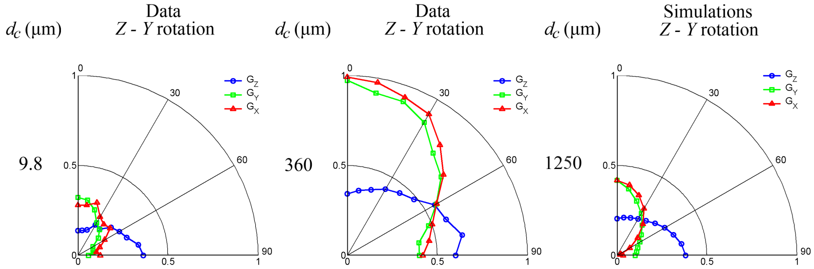

Figure 37: Nerve sample Z to Y rotation data for $d_c = 9.8$ and 360 μm. For comparison a numerical simulation of a homogeneous cylinder of diameter 1250 μm and $d_c = 1250$ μm is plotted as well. The similar shapes in all three cases indicates cylindrical structures in nerve with diameters of roughly 10 μm and 360 μm. Fig.35 indicates that this distinctive angular dependence occurs only at these two correlation distances.

$Y - X$ rotations, and they found corresponding $3\cos^2\theta_{sample} - 1$ and $2\cos^2\phi_{sample} - 1$ sample orientation dependences, respectively. Fig. 34 shows that these correspondences only hold, roughly, for $d_c \leq$ the cylinder diameter. Additional points of interest include that $\|G_Z\| - \|G_X\| - \|G_Y\|$ goes to zero at $d_c = 0$ and $|3\cos^2\theta_{sample} - 1|$ at $d_c = \infty$ (the first of which is an exception rule to the $d_c \leq$diameter rule), and that $\|GXR\| - \|GYR\|$ goes to zero at both $d_c = 0$ and $d_c = \infty$. (These results are not shown, but are clear from Fig.33).

Nerve sample

A central goal of CRAZED studies is to provide information on the sample structure. However the optimum acquisition parameters (d_c and gradient direction) and data analysis method are still not determined. One option is a full acquisition in the correlation space, gathering data at every gradient strength and direction [29]. This method suffers from exceedingly long acquisition times and possible complications due to diffusion damping. An alternative generalized numerical fitting method for simple geometries was demonstrated by Bouchard and Warren [42], but it requires *a priori* knowledge of the scale (though not shape) of the underlying structure.

One popular alternative is a simple 1D acquisition [34, 36, 59, 32], where only the correlation distance d_c is varied and not the gradient or sample orientation. However, the clear signal dependence on the sample orientation, evident in Fig.33 , complicates this approach. Nonetheless, some sample structure information can be gleaned from the general trend. Figs. 36b and 36d plot the simulated CRAZED signal as a function of d_c for sample rotations in the $Z-Y$ and $Y-X$ planes, respectively, and gradients in the Z direction. Each line represents a different sample orientation. While the signal has a clear dependence on θ_{sample}, in all cases the signal decays (very roughly) exponentially and with a decay constant on the order of one cylinder diameter. Figs. 36a and 36c give corresponding results for nerve. Again, the signal varies roughly exponentially with d_c and with a decay constant on the order of sample diameter. In this case, the sample is a 1.8 mm inner diameter hollow plastic filled with two sciatic nerve segments, so this gross signal variation gives an indication of the total nerve sample size, but not of the nerve substructures.

Our results suggest several possible analyses of the crazed data that reveal the underlying sample micro-anatomy, with all such methods indicating cylindrical structures in nerve with diameter of roughly 10 μm (axons) and/or 360 μm (tibial and peroneal fascicles). The most convincing results are from Fig.35 and are reproduced in Fig.37.

Fig.35 shows that the nerve sample data is a complex function of sample orientation, gradient direction, and correlation distance d_c. When d_c=10 μm and 360 μm, however, Fig.37 illustrates how this data matches a simulation of a cylinder of diameter d_c. The shape of this functional dependency on the sample orientation and gradient direction is unique to these two correlation distances in nerve, as is clear from Fig.35. (The corresponding water data and simulations in Fig.33 show that this same rough functional shape occurs in this structureless phantom only when $d_c \approx$the sample diameter of 1250 μm.) More subtle indicators of cylindrical structures in nerve include the $3\cos^2\theta_{sample} - 1$ dependence of $\|G_Z\| - \|G_Y\| - \|G_X\|$ at d_c=10 μm (but not at larger d_c) and the sign flip in $\|GXR\| - \|GYR\|$ at d_c = 360 μm, both illustrated in Fig.35. Both of these signal dependences occur in simulations near d_c = cylinder diameter, as shown in Fig.4.

While the indication of cylindrical structures at 10 μm is not surprising, and could have been better examined via diffusion measurements, the indication of a cylindrical structures near 360 μm likely reflect the tibial and peroneal fascicles (see Fig.32), which are not easily examined via other magnetic resonance methods. While these analyses requires sample rotation and therefore may not be well suited to *in vivo* studies, they do provide a strong indication of CRAZED's ability to reveal structures at otherwise unattainable distance scales.

CHAPTER V

FIBROTIC MURINE LIVER STUDIES.

Introduction

“Fibrosis is the formation or development of excess fibrous connective tissue in an organ or tissue as a reparative or reactive process, as opposed to a formation of fibrous tissue as a normal constituent of an organ or tissue” [64].

Today only a liver biopsy is an ultimate foolproof method for assessing hepatic fibrosis. It is known as an invasive and potentially harmful for the patient procedure. Magnetic resonance imaging is about to address this problem more closely (see for example [65, 66]) and our next test data. Crazed imaging, with its unique potentials is a promising method to detect the structural inhomogeneities accompanying liver fibrosis.

Methods

This part of the thesis project was intended to be a continuation of a different study where the same mouse liver sample was previously used for mechanical properties testing. This testing sought to determine the elastic modulus of normal and fibrotic murine livers [67]. In order to develop fibrosis, a group of mice received intraperitoneal injections of carbon tetrachloride (Sigma Chemical, St. Louis, MO, USA) mixed with olive oil (Sigma Chemical, St. Louis, MO, USA) in a 1:4 ratio, respectively, on a weekly basis. Each dose of CCl_4 was introduced in a 1 ml/kg injection. We had

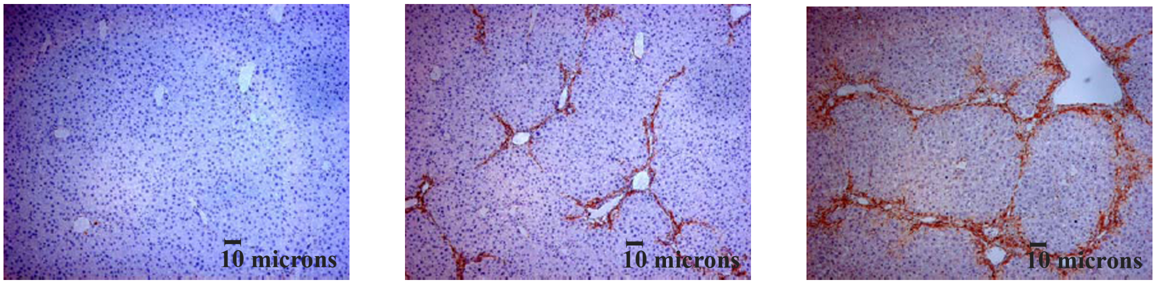

(a) (b) (c)

Figure 38: Stages of a liver fibrosis. Results from alpha-SMA staining with (a) normal, (b) mild fibrosis, and (c) more severe fibrosis. Reproduced with permission of Dr. Lyschik

in our possession a small part of the liver lobe embedded in polyacrylamide gel as a leftover from mechanical shift and compression testing. All these previous procedures take on the order of couple of hours.

Liver structure

The liver cell, or hepatocyte (Gr. hepar, liver, + kytos, cell), represents the basic structural component of the liver. These epithelial cells form a series of interconnected plates. When stacked together, these plates constitute the next structural level of organization, the liver lobule. The last one is formed of a polygonal (single honeycomb cell like) mass of tissue about 0.7 x 2 mm in size for humans [8] and more than twice as small in mice (see Fig.38) , with portal spaces at the periphery and a vein, called the central or centrolobular vein, in the center. Portal spaces, regions created between adjacent lobules, contain connective tissue, bile ducts, lymphatics, nerves, and blood vessels. The initial target for our studies are the structures on the order of 10 μm and, as one can see, they are represented by the central vein and corner spaces formed by connective fiber tissues enclosing hepatic lobules (see Fig.39).

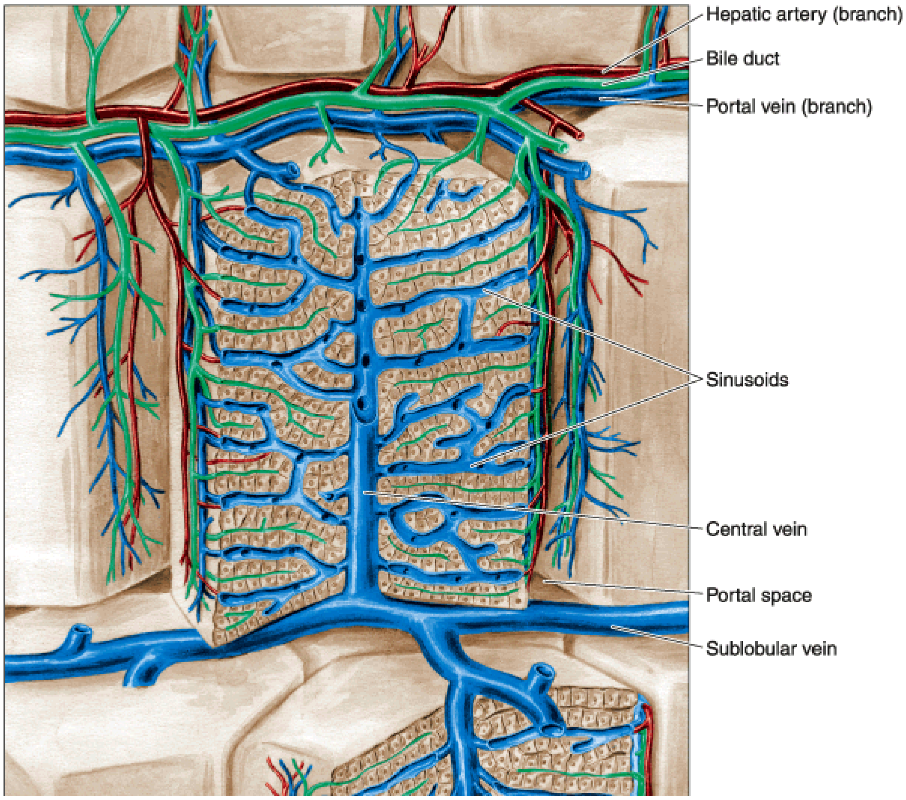

Figure 39: Liver structure. Hexagonal cylinder in the center is the liver lobule. It is surrounded by the portal space. Arteries (red), veins (blue), and bile ducts (green) are filling the portal spaces. Structures like nerves, connective tissue, and lymphatic vessels are not shown. Reproduced from [8].

Later stages of fibrosis offer another bigger scale structure as a target for detection, the hepatic lobule by itself enclosed by a swollen and degenerated fiber tissue (see Fig.38c). Central veins stay mainly intact for the shown type of fibrosis, but now the whole lobule is highlighted by the fibrotic tissue, which is expected to contribute to correlation distances spectrum as well. That sounds like a good back-up plan due to existing gradient strength limitations, diffusion damping and other reasons which are placing correlation distance of 10 μm at or well below resolution limits of our method.

Beginning this project we were not going to image the cell structure of the liver even if we were able to. Also there was made no systematic attempt to measure

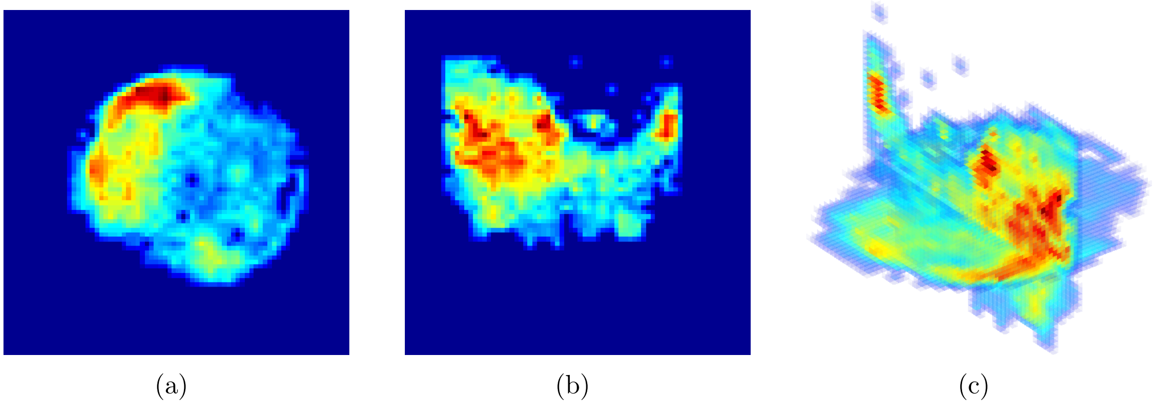
(a) (b) (c)

Figure 40: Gradient echo scout images of a liver sample 4.5×4.1 mm.(a) Sagital slice. (b) Axial slice. (c) Combined view of (a) and (b)

dynamics of T_1 and T_2 properties as a function of time for our leftover samples. Fibrotic structure of the liver is well known to stay intact for a time period well beyond several hours, which was confirmed by our visual examination. Thus we settled with our method refinement leaving most of the quantitative test procedures as a goal for the future studies.

Data acquisition

The liver sample used for measurements was prepared by applying an open end of 5 mm nmr tube (Wilmad-Labglass, Buena, NJ, USA) against the liver sample. Naturally sharp and with the wall thickness less then 0.5 mm this tube represents a suitable cutting tool when used on the part of the mouse liver lobe we have extracted from the gel. As a result we end up with a cylindrical sample with a radius equal to the inner radius of the tube and a height on the order of sample thickness at the place of application (in general it was on the order of the inner tube diameter as well) (see Fig.40).

The liver sample was placed in the bore of the magnet (7 Tesla 16-cm horizontal bore Varian Inova (Varian Inc., Palo Alto, CA, USA) scanner system running at 300 MHz and using a 25 mm diameter and 22 mm long Litz coil from Doty Scientific,Columbia, SC, USA) with the major axis of nmr tube aligned along the Z axis. For our measurements the same pulse sequence and phase cycling scheme was used, as described previously in Chapter 4. 2D experiment was set in such a way that the crazed gradient consecutively takes the values [1.0 3.0 5.0 7.0 9.0 11.0 13.0 15.0 17.0 19.0] G/cm and its direction is changed in steps of 5° from being aligned along the Z axis ($\theta_{gradient} = 0°$) to being aligned along the Y axis $\theta_{gradient} = 90°$. Duration of the first CRAZED gradient ("tgrad_DG") was chosen to be 2 ms. This procedure produced a 10 by 19 data matrix of double quantum echoes amplitudes.

When the induced magnetization helix is twisted strongly enough (much smaller than any sample structure) we expect to see $3\cos^2\theta_{gradient} - 1$ dependence on the CRAZED gradient orientation. When the corresponding correlation distance reaches the next (larger) level of structure size we expect to see deviations from this functional dependency on $\theta_{gradient}$, as in our previous nerve data and numerical simulations.

In order to ensure full recovery of the magnetization and preclude the possibility of stimulated echoes, TR (repetition time) was set to 20 s. With 4 part phase cycling done twice (signal to noise ratio at the $\theta_{gradient}$ angles close to 90° was still very low) this made the overall time of measurement about 8 hours, again posing the question of the practical applicability for this type of the measurement. Though significant decreases in the measurement time are likely possible with appropriate optimization.

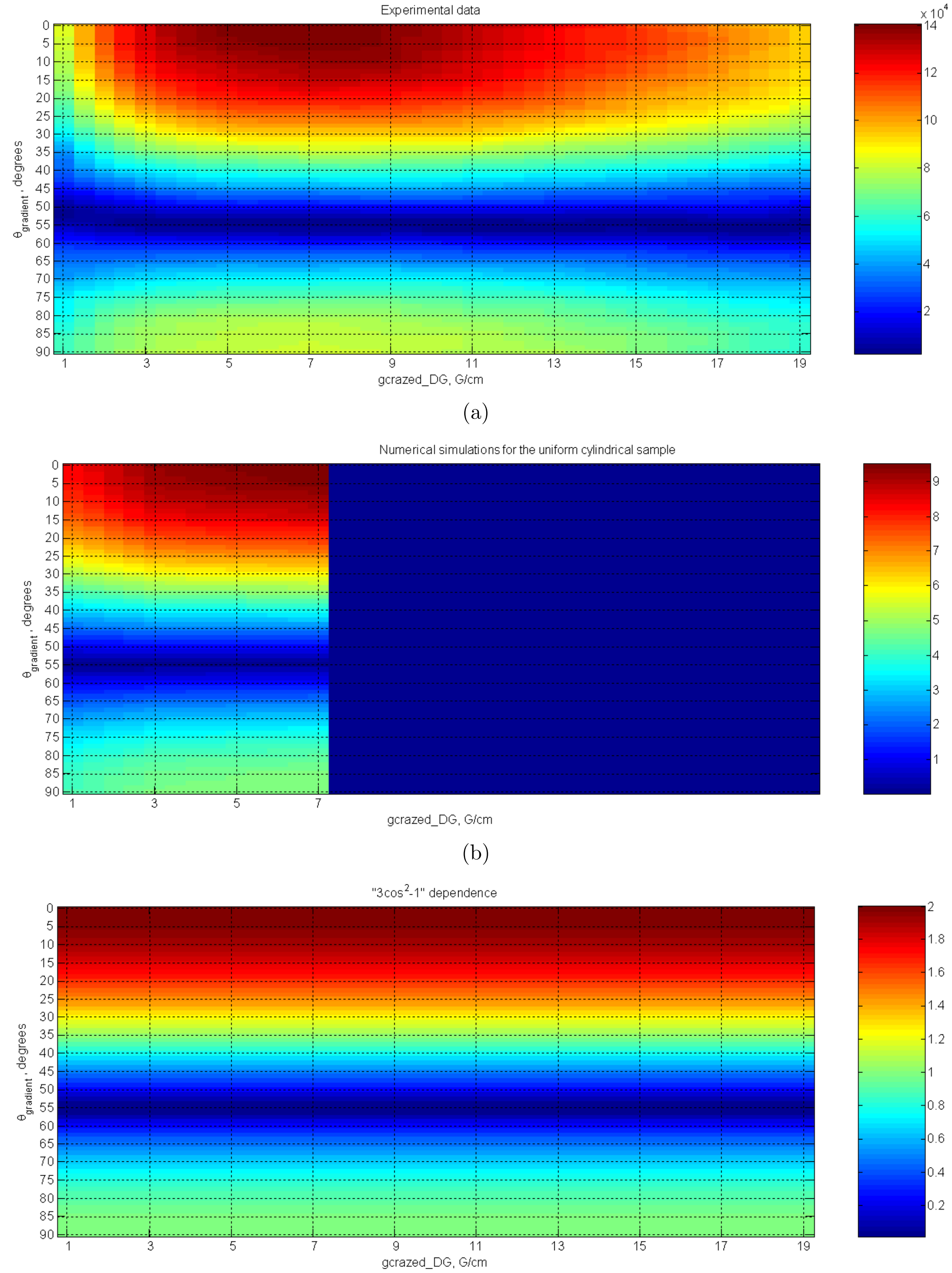

(a)

(b)

(c)

Figure 41: Liver sample.(a) Experimental data. (b) Numerical simulations. (c) $3\cos^2-1$ law

Numerical simulations

Our basic CRAZED numerical simulations were run for this study. The phantom was represented by uniform cylinder 192 pt high an 192 pt wide which is translated into 4×4 mm real values. The purpose was to generate the reference data when the induced correlation distance will be on the order of sample diameter (see Fig.42(b)).

Pulse sequence, its phase cycling scheme and other numerical procedures were implemented in the say way as described in Chapter 4, subsection "Numerical simulations" only now the sample stayed fixed in the magnet and the CRAZED gradients were rotated from Z axis backward along the Y axis in 5° steps. All simulations were performed using MATLAB®R2006b(73) (MathWorks, Natick, MA, USA) software package, running under RedHat Enterprise Linux-WS v4 OS (Red Hat, Inc, NC, USA) on a Dual Intel®XEON$^{\mathrm{TM}}$, CPU 2.20 GHz with 3.5 Gb RAM and 80 Gb ATA HD of the local storage.

Results

Results from these measurements are given in Figs.40, 41 and 42.

Figs.41 (a) and (b) show the two gradient echo images from the "scout" protocol implemented on 7 Tesla Varian small imaging system. The typical sample size was 4.0±0.5 mm wide and 4.0±0.5 mm long (on the figure it is 4.5×4.1 mm). Although not seen on the MR image this sample was shown to have a fibrosis stage corresponding to the Fig.38(b) (mild fibrosis).

Fig.41 shows the typical data comparison scheme we were using in our experiment. Part (a) represents the raw data. For the display purpose 10×19 matrix was interpolated twice with respect to the gradient values and twice with respect to the angle values which made it 37×73. Part (b) of the same figure shows numerical simulations for the uniform cylinder which has the same size as our liver sample but do not possess any substructure. These simulations stop at he gradient value of 7 G/cm because we are not able to simulate gradients stronger to sample a smaller distance scale. Numerical simulation data was interpolated as well to match the new 37×73 resolution of the experimental data. Part (c) is a three dimensional plot of the "$3\cos^2 -1$" function constant with respect to the gradient variations along X axis of the plot and given for the angles values ranged from 0° to 90°.

In order to minimize sensitivity of the data to diffusion damping and other parameters changing with the gradient strength but not related to the double quantum signal angular dependence, we need to normalize our data with respect to the first point in DQC=f($\theta_{gradient}$) dependence. At this point CRAZED gradient is aligned along the Z axis and $\theta_{gradient}$=0 (see Fig.42). This should be done for each value of the gradient.

Thus Fig.42 represents the same set of the data as on Fig.41 only each line along Y axis is normalized with respect to the first point, which was assigned a value of 2, the value which "$3\cos^2\theta_{gradient} - 1$" function should take if $\theta_{gradient}$=0.

Discussion and conclusions

Fig.41(a)-(b) and Fig.42(a)-(b) display several common features of the DDF field; such as zero signal at $\theta_{gradient}$=54.7° ("the magic angle"), typical gradient strength dependence along the X axis of the plots, as well as weighted $\alpha\,(3\cos^2(\theta_{gradient}) - 1)$

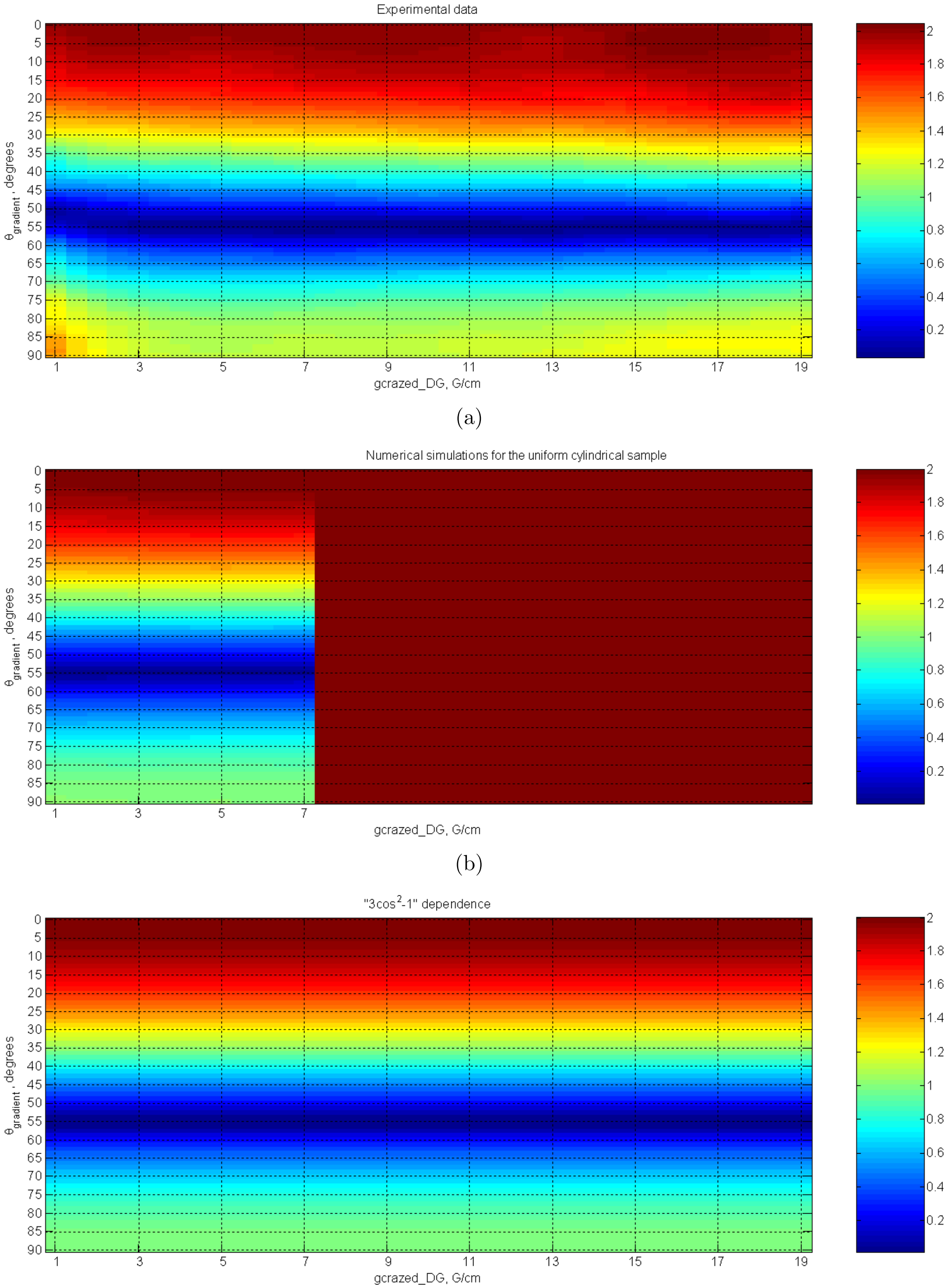

(a)

(b)

(c)

Figure 42: Liver sample. Normalized data.(a) Experimental data. (b) Numerical simulations. (c) $3\cos^2(\theta_{gradient}) - 1$ law

gradient direction dependence along the Y axis of the plots. Good match of Fig.41(a) with simulations on Fig.41(b) for the low gradient values proves one more time the reliability of our numerical simulations. Fig.41(c) plotted as a reference and shows that the closest match with the $3\cos^2(\theta_{gradient}) - 1$ dependence for the regular type of normalization (maximum signal in the data set was set equal to 2) is observed around $G = 7.0$ G/cm which corresponds to the d_c=0.09 mm which happens to be on the order of the lobule size (see Fig.40).

In order to further develop our approach we have normalized the data according to the procedure described in the results (with respect to the first point in $\theta_{gradient}$) dependence (see Fig.42). One more time we can see that the point in 7 G/cm (d_c =0.09 mm) have the closest match with $3\cos^2(\theta_{gradient}) - 1$ dependence.

We have abstained from the further studies due to the luck of biological samples and complex structured numerical model leaving it as a project for a future studies. The first obstacle is a matter of finding proper collaboration group while the last one is a matter of time and motivation, when an extra efforts should be invested into increasing the simulation grid size as well as the speed of calculations.

CHAPTER VI

CONCLUSIONS AND FUTURE STUDIES.

Conclusions and Future Studies

iMQC, despite its deceptive simplicity and less than optimal signal-to-noise ratio, is potentially a very powerful method. The coherent cumulative contribution of the signals from all the microscopic structure elements to the macroscopically-observed effect is amazing. At this time, all the classical ways of enhancing the signal (including phase cycling, multiple averaging and acquisition technique refinement) have been tested almost to their full extent without a major breakthrough. Nevertheless, the iMQC method is still viable and waiting for its time to come.

In this thesis, we have offered a full-scale simulation program for all the experimental CRAZED applications which have been done by our group. Full accounting for all the interaction mechanisms and collective effects in the numerical simulations give them immense predictive power.

Our implementation has many unique features like flexibility and expandability. Its block structure allows us to easily add different terms and interaction mechanisms, as well as arbitrary pulse components, to the simulations. We have already implemented and tested instantaneous and continuous versions of the RF pulses and gradients. The linear approximation for the dipolar field calculation used everywhere throughout this thesis is easily extended to the nonlinear regimes with times much longer than $\tau_{dipolar}$. Our temporary limitation on the simulation grid size may be easily bypassed by using algorithms for parallel computation as well as simple matrix fragmentation at all levels of the code.

We discovered new effects which have been observed numerically and experimentally by studying the complex structured samples. Two major biological tissues of interest were studied (see chapters IV and V). Rat sciatic nerve projects have shown encouraging results in sensitivity to the different length of scale in biological samples and may be linked to myelin and other neurodegenerative diseases of great importance. Methods used and tested for mice liver studies are applicable for any nested complex structures and may be useful to further facilitate the quest for high resolution MR.

Planned full-scale high-resolution numerical simulations will offer insight into subtle effects buried deep under field inhomogeneities, relaxation processes, diffusion, radiation damping and hardware imperfections. Right now it is still difficult to make sure that alterations to the magnetization helix are introduced by the real discontinuities in the spin distribution and not by experiment imperfections.

Ambiguous sensitivity to T_1, T_2 distributions raises the question of interaction with other types of contrast available for MR. So far, only part of the phase information about helix formation has been used. Our study will continue in this direction as well.

APPENDIX A

DDF CALCULATIONS IN FOURIER SPACE AND DIRECTLY

```
% Perform DDF calculations for Mz~=0 (Mx, My=0) through Fourier Space and Directly
% and store the data file with time necessary for both calculations

clear all; close all;

% Data input

% Range of voxels number to simulate. From n till N.
n=5;N=555;

% Calculation time for different methods

t=zeros(3,N-n+1);
% t(1,N) <= number of voxels
% t(2,N) <= time for the Fourier Space Calculations
% t(3,N) <= time for the Direct Calculations

counter=1;

for voxels=n:N

    t(1,counter)=voxels;

    % display current configuration

    voxels
    radius =floor(voxels/4);   % To make sure that the radius will not exceed 1/4th of voxels number
    ctr = floor(voxels/2 +1);  % Center of the phantom

    % preallocation of magnetization and other matrices
    mr3_initial = zeros([voxels voxels voxels]);        % Magnetization Distribution
    deltak = zeros([voxels voxels voxels]);             % Matrix of Dipolar Weighting Coefficients

    non_local_sum = zeros([voxels voxels voxels]);      % Non Local Sum for Direct Calculations
    Bd_0 = zeros([voxels voxels voxels]);

    % Object definition
    shape='cube';
    condition='(r1-ctr)^2 <= radius^2 & (r2-ctr)^2 <= radius^2 & (r3-ctr)^2 <= radius^2';

    %shape='cylinder';
    %condition='(r1-ctr)^2 + (r2-ctr)^2 <= radius^2 & (r3-ctr)^2';

    %shape='sphere';
    %condition='(r1-ctr)^2 + (r2-ctr)^2 + (r3-ctr)^2 <= radius^2';

    %shape='disc';
    %condition='(r1-ctr)^2 + (r2-ctr)^2 <= radius^2 & r3 == ctr';

    % Filling the value of initial magnetization with unit values
    for r1=1:voxels
        for r2=1:voxels
            for r3=1:voxels
                if eval(condition)
                    mr3_initial(r1,r2,r3) = 1.0;
                end
            end
        end
```

```
    end

    % Calculations through Fourier space, ignoring k=0 component
    tic
    zero_freq = floor(voxels/2 +1);
    for k1=1:voxels;
        for k2=1:voxels;
            for k3=1:voxels
                if k1==zero_freq && k2==zero_freq && k3==zero_freq
                    deltak(k1,k2,k3) = 0.0;
                else
                    deltak(k1,k2,k3) = (3*((k3-zero_freq)^2 / ...
                        ((k1-zero_freq)^2 + (k2-zero_freq)^2 + (k3-zero_freq)^2)) - 1)/2;
                end
            end
        end
    end
    br3_fourier=real(2/3.*ifftn(ifftshift(deltak.*fftshift(fftn(mr3_initial)))));
    t(2,counter)=toc;

    % Direct calculations
    tic
    for r1=1:voxels
        for r2=1:voxels
            for r3=1:voxels
                for rp1=1:voxels
                    for rp2=1:voxels
                        for rp3=1:voxels
                            if rp1 == r1 && rp2 == r2 && rp3 == r3
                                non_local_sum(r1,r2,r3)=non_local_sum(r1,r2,r3);
                            else
                                non_local_sum(r1,r2,r3)= non_local_sum(r1,r2,r3)...
                                    +(1-3*((r3-rp3)^2/((r1-rp1)^2 + (r2-rp2)^2 + (r3-rp3)^2))) / ...
                                    (2*((r1-rp1)^2 + (r2-rp2)^2 + (r3-rp3)^2)^1.5).* ...
                                    2*mr3_initial(rp1,rp2,rp3);
                            end
                        end
                    end
                end
            end
        end
    end
    br3_direct = 1/(4*pi)*non_local_sum;
    t(3,counter)=toc;

    save(strcat('Direct_And_Fourier_',num2str(voxels)), 'br3_direct', 'br3_fourier' , 'voxels', ...
    'shape', 'radius', 'ctr');
    save t t
    counter=counter+1;
end
```

APPENDIX B

THE MATLAB CODE IMPLEMENTATION OF THE CRAZED EXPERIMENT NUMERICAL SIMULATIONS

```
% June 07, 2008. Y to X Nerve Slice Rotations. Bunch D=238, Bunch L=30 , 256x256x256
clear all; close all;
tic
cd /home/kussaias/MatlabCode/m2008_JUN07_Axons/YtoX

% 10 degree step in  rotations
A_ngle=linspace(0,90,10)*pi/180;

% Fundamental constants
g = 267.522*10^6;                                       % [rad/s/T]
mu0 = 4*pi*1e-7;                                        % [NA^-2]
D = 2*10^(-9);                                          % [m^2/s]

% B0, Radiation damping, Dipolar Time
tesla =7.0;                                   % [T]
w0=tesla*g/(2*pi);                            % [1/s/T]
delta_w=0.0;                                  % [1/s]
filling_factor=1.0;
Q=7;
M0=0.00318*tesla;                             % [A*m-1] For the water at room temperature
tau_dipolar=1/(mu0*g*M0);                     % tau_dipolar=1/[Gamma*mu0*M0] seconds
tau_damping=tau_dipolar/(filling_factor*Q/2); % tau_damping=1/[Gamma*mu0*M0*(filling_factor*Q/2)]   [s]
tau_damping=1e8;

% Time and step of integration
% Redundant in this reduced case
dt = 5e-02;                                   % [s]

% Simulation volume parameters
shape='Nerve_Slice';
A_long='Y';
% Could be find in the data file and will be overwritten
voxels = 256;                                               % Number of voxels in the cube
ctr = floor(voxels/2 +1);                                   % Center of the cell
R=238/2;                                                    % Radius of the bundle in voxels
r=1;                                                        % Radius of individual nerve d=3pts ~ 10um
half_length=30/2;                                           % Half length of the fiber

voxel_size=1.8e-3/(238)/5;                                  % [m/voxel] ~Fascicle diameter/Number of


% R1, R2, chemical shift, and diffusion as a functions of position
R1_copy=.0; R2_copy=.0;
%R1 = R1_copy*mr_density;                               % [Hz]
R1=R1_copy; % array-->scalar to save memory
%R2 = R2_copy*mr_density;                               % [Hz]
R2=R1_copy; % array-->scalar to save memory
clear R1_copy R2_copy

% Gradient strength. As in Experiment
G_radient=[0.04893 0.16310 0.54367 1.83489 5.87165 19.57217]...                          % [Gauss/cm]
     *1e-4/1e-2;                                         % [T/m]

% Gradient duration. As in Experiment
T=6.0...                                                 % [ms]
         *1e-3;                                          % [s]
```

```

% Correlation distances
% [ i.e. How much space takes 1/2 of the full cycle ]
d_c=pi./(g*G_radient*T);                                 % [m]
display(d_c)
% [ How many voxels takes 1 full cycle ]
one_cycle_size=2.0*d_c/voxel_size;                       % [voxel]
% d_c in pts
display(d_c/voxel_size);                                 % [voxel]

% Apply Gauss filtering 'y'/'n'
   smoothing= 'n';
if smoothing=='y'

    zero_freq = floor(voxels/2 +1);
    variance=.7*voxels/(16*sqrt(log(2)));

    filter_name = strcat('Filter_',...
        num2str(voxels),'voxels_',...
        num2str(ctr),'ctr_',...
        num2str(round(variance*100)),'var');

    file_exists = which([filter_name '.mat']);
    if isempty(file_exists)
        gauss_filter=zeros([voxels voxels voxels]);
        for k1=1:voxels;
            for k2=1:voxels;
                for k3=1:voxels;
                    gauss_filter(k1,k2,k3) = (sqrt(2*pi)*variance)^-3*...
                        exp(-((k1-zero_freq)^2+(k2-zero_freq)^2+(k3-zero_freq)^2)/(2*variance^2));
                end;
            end;
        end;
        gauss_filter=gauss_filter/max(max(max(gauss_filter)));
        eval(['save ' filter_name ' gauss_filter']);
    else
        eval(['load ' filter_name ' gauss_filter']);
    end
    clear k1 k2 k3 zero_freq variance
end

% instantaneous RF pulses
RF_angles =[pi/2 2*pi/3];                               % [radians]

% Phase cycling data
rf1=[0 pi/2 pi 3*pi/2];                                 % first RF pulse
rf2=[0 0 0 0];                                          % second RF pulse
acq=[0 pi 0 pi];                                        % acqusition
N_phases=length(rf1);                                   % number of phase steps

% Generic name for the given geometry
Object_Data = [shape strcat('_v',num2str(voxels),'_R',num2str(round(R)),'_r3',...
        '_c',num2str(ctr),'_HL',num2str(half_length))]

for GT=1:length(G_radient)


pattern=[1 0 0                                          % unit gradient along X axis
         0 1 0                                          % unit gradient along Y axis
         0 0 1];                                        % unit gradient along Z axis

     for G=1:3;                                         % loop over the different gradient directions
         display(num2str(clock))
         gradient_cycles =pattern(G,:);                 % [cycles/voxel]

         % Current values of Mx and My magnetization
         P_olar_Mx=zeros(1,length(A_ngle));
         P_olar_My=zeros(1,length(A_ngle));
```

```
        for D_irect=1:length(A_ngle)

            % Phase cycling if any. Otherwise just one step
            for v=1:N_phases;

                % Specific color for all 4 phase steps
                v_color=['r' 'g' 'b' 'k'];

                % Display current sample's orientation
                display(A_ngle(D_irect)*180/pi)

                % Load current .mat file for the rotated sample
                eval(['load ' strcat(Object_Data,'_',A_long,'_',num2str((D_irect-1)*10))]);

                % Sum of all spins
                spin_number=sum(sum(sum(mr3)));

                % Sum of all spins in specific XY plane.
                spin_number_XY=squeeze(sum(squeeze(sum(mr3,1)),1));

                % Need to replace all zeros with ones to avoid 'division by zero'
                % error message in normalization procedure
                for c=1:length(spin_number_XY)
                    if spin_number_XY(c)==0
                        spin_number_XY(c)=1;
                    end
                end

              % mr_density, mr1,mr2,and mr3 as function of position

              % mr_density =  zeros([voxels voxels voxels]);
                mr1 = zeros([voxels voxels voxels]);
                mr2 = zeros([voxels voxels voxels]);
              % mr3 loaded from the hard drive

                % Gauss filtering
                if smoothing=='y'
                    eval(['load ' filter_name ' gauss_filter']);
                    mr1=real(ifftn(ifftshift(gauss_filter.*fftshift(fftn(mr1)))));
                    mr2=real(ifftn(ifftshift(gauss_filter.*fftshift(fftn(mr2)))));
                    mr3=real(ifftn(ifftshift(gauss_filter.*fftshift(fftn(mr3)))));
                end
                clear gauss_filter;

                % Field of instantaneous gradient
                gradient_matrix_name = strcat('Inst_Gradient_',...  % Name contains number of voxels
                    num2str(voxels),'voxels_',num2str(ctr));       % and position of the center 'ctr'

                file_exists = which([gradient_matrix_name '.mat']);
                if isempty(file_exists)

                    g_cycl_mat_X=zeros(voxels,voxels,voxels);
                    g_cycl_mat_Y=zeros(voxels,voxels,voxels);
                    g_cycl_mat_Z=zeros(voxels,voxels,voxels);

                % All matrix has symmetric "ctr" value at the center coordinate which is not required
                    for j=1:voxels;
                        g_cycl_mat_X(j,:,:)=(j-ctr)*ones(voxels,voxels);
                        g_cycl_mat_Y(:,j,:)=(j-ctr)*ones(voxels,voxels);
                        g_cycl_mat_Z(:,:,j)=(j-ctr)*ones(voxels,voxels);
                    end;

                    eval(['save ' gradient_matrix_name ' g_cycl_mat_X g_cycl_mat_Y g_cycl_mat_Z']);

                else
                    eval(['load ' gradient_matrix_name ' g_cycl_mat_X g_cycl_mat_Y g_cycl_mat_Z']);
                end
```

```
            % Modifying the components of uniform unit field of instantenous grad. by
            % the  gradient_cycles matrix values
            g_cycl_mat_X=g_cycl_mat_X*gradient_cycles(1);
            g_cycl_mat_Y=g_cycl_mat_Y*gradient_cycles(2);
            g_cycl_mat_Z=g_cycl_mat_Z*gradient_cycles(3);

            % calculations of contribution of the gradients in all
            % directions to the local frequency offset
            g_cycl_mat=(g_cycl_mat_X+...
                        g_cycl_mat_Y+...
                        g_cycl_mat_Z)/one_cycle_size(GT);
            % and rescale with respect to the real size of the CURRENT cycle
            clear file_exists j k l gradient_matrix_name g_cycl_mat_X g_cycl_mat_Y g_cycl_mat_Z

            % interface again for phase counter
            %figure(2);

            %set(gcf,'Position',[768 69 509 880], 'PaperPosition', [.0 .0 11 8.5],...
            %    'PaperOrientation','Landscape');

            %subplot(4,2,1);axis off;
            %text(0,1.4,strcat('voxels',' = ',num2str(voxels)));
            %text(0,0.2,strcat('tau_d_i_p_o_l',' = ',num2str(tau_dipolar),' s' ));
            %text(0,0.0,strcat('smoothing =',' "',smoothing,'"'));

            %text(.4,1.4,strcat(shape,' sampled at' ,'  dt =', num2str(dt),' s'));
            %text(.4,1.2,strcat('B_0 =',num2str(tesla),' Tesla'));
            %text(.4,1.0,'first inst grad [cycles/voxel]=');
            %text(0.9,1.0,strcat('[',num2str(gradient_cycles/one_cycle_size(GT)),']'));
            %text(.4,0.8,'first inst grad [T/m]=');
            %text(0.9,0.8,strcat('[',num2str(G_radient(GT)),']'));
            %text(.4,0.6,'correlation distance [m] =');
            %text(0.9,0.6,strcat('[',num2str(d_c(GT))      ,']'));

            %text(.4,0.4,strcat('voxel size =',num2str(voxel_size),'meter/voxel'));
            %text(.4,0.2,strcat('cell size =',num2str(voxels*voxel_size),' meter'));

         %text(1.4,1.4,strcat('RF pulses',' = ','[',num2str(RF_angles.*180/pi),']', ' degrees'));
         %text(1.4,1.2,strcat('rf_1  phases',' = ','[',num2str(rf1.*180/pi),']', ' degrees'));
         %text(1.4,1.0,strcat('rf_2  phases',' = ','[',num2str(rf2.*180/pi),']', ' degrees'));
         %text(1.4,0.8,strcat('Acq phases',' = ','[',num2str(acq.*180/pi),']', ' degrees'));

            %subplot(4,2,1);axis off;
            %text(2.1,1.4-(v-1)*0.2,strcat('current step v',' = ',num2str(v)));
            %drawnow;hold on;

            % Creating the final distribution of the magnetizations for the
            % different combinations of RF pulse phases

            [mr1, mr2, mr3]=...
                instant_rf(mr1, mr2, mr3, RF_angles(1), rf1(v));
            [mr1, mr2, mr3]=...
                instant_grad(mr1, mr2, mr3, g_cycl_mat);
            [mr1, mr2, mr3]=...
                instant_rf(mr1, mr2, mr3, RF_angles(2), rf2(v));
            [mr1, mr2, mr3]=...
                instant_grad(mr1, mr2, mr3, 2.0*g_cycl_mat);

            clear g_cycl_mat

            % Phase cycling. Prefix 'd_' denotes Mx,My,Mz
            % magnetizations in terms of acqusition reference frame

            d_mr1=zeros([voxels voxels voxels]);
            d_mr2=zeros([voxels voxels voxels]);
            d_mr3=zeros([voxels voxels voxels]);

% Creating or overwriting existing ones "t=-0" .mat files for the Mx, My and Mz 3D magnetization
```

```
                if v==1
                    name=strcat('Mx','_',num2str(0));
                    eval(['save ' name ' d_mr1']);

                    name=strcat('My','_',num2str(0));
                    eval(['save ' name ' d_mr2']);

                    name=strcat('Mz','_',num2str(0));
                    eval(['save ' name ' d_mr3']);
                end
                % basic definition of the phase cycling
                if acq(v)==0
                    d_mr1=mr1; d_mr2=mr2;
                end

                if acq(v)==pi/2
                    d_mr1=mr2; d_mr2=-mr1;
                end

                if acq(v)==pi
                    d_mr1=-mr1; d_mr2=-mr2;
                end

                if acq(v)==3*pi/2
                    d_mr1=-mr2; d_mr2=mr2;
                end

                % I'm using d_mr3 as a temporary storage cell
                % and updating the Mx, My, Mz from hard drive by it
                % with each phase step

                name=strcat('Mx','_',num2str(0));
                d_mr3=d_mr1;
                eval(['load ' name ' d_mr1']);
                d_mr1=d_mr3+d_mr1;
                eval(['save ' name ' d_mr1']);

                name=strcat('My','_',num2str(0));
                d_mr3=d_mr2;
                eval(['load ' name ' d_mr2']);
                d_mr2=d_mr3+d_mr2;
                eval(['save ' name ' d_mr2']);

                name=strcat('Mz','_',num2str(0));
                % "d_mr2=mr3" mr3 stays the same irrespectively of the acqusition
                % phase
                d_mr2=mr3;
                eval(['load ' name ' d_mr3']);
                d_mr3=d_mr2+d_mr3;
                eval(['save ' name ' d_mr3']);

                % These averaged values are used to plot magnetization evolution
                mr1_1=sum(sum(sum(mr1)))/spin_number;
                mr2_1=sum(sum(sum(mr2)))/spin_number;
                mr3_1=sum(sum(sum(mr3)))/spin_number;

                % Evolution under the Bloch equation

                ps_grad=0.0; % means no background or other "non" instanteneous gradients
                t=0;

                counter=1;
                while t<=.0;
                    % 4th order Runga-Kutta: 'Numerical Recipes in C', 1988, p. 570
                    [d_mr1, d_mr2, d_mr3] = ddf_bloch_eqns( ...
                        mr1, mr2, mr3,M0,...
                        R1, R2, delta_w, ps_grad, D,...
                        ctr,t,dt,...
```

```
    spin_number,spin_number_XY);
% Warren’s linear approximation
mr1=d_mr1;
mr2=d_mr2;
mr3=d_mr3;

%mr1=mr1+dt*d_mr1/6;
%mr2=mr2+dt*d_mr2/6;
%mr3=mr3+dt*d_mr3/6;

%[d_mr1, d_mr2, d_mr3] = ddf_bloch_eqns( ...
%    mr1+dt*d_mr1/2,mr2+ dt*d_mr2/2,mr3+ dt*d_mr3/2,M0,...
%    R1, R2, delta_w, ps_grad(:,:,:), D,...
%    ctr,t,dt,...
%    spin_number,spin_number_XY);
%mr1=mr1+dt*d_mr1/3;
%mr2=mr2+dt*d_mr2/3;
%mr3=mr3+dt*d_mr3/3;

%[d_mr1, d_mr2, d_mr3] = ddf_bloch_eqns(...
%    mr1 + dt*d_mr1/2, mr2+ dt*d_mr2/2, mr3+ dt*d_mr3/2,M0,...
%    R1, R2, delta_w, ps_grad, D,...
%    ctr,t,dt,...
%    spin_number,spin_number_XY);
%mr1=mr1+dt*d_mr1/3;
%mr2=mr2+dt*d_mr2/3;
%mr3=mr3+dt*d_mr3/3;

%[d_mr1, d_mr2, d_mr3] = ddf_bloch_eqns( ...
%    mr1 + dt*d_mr1,mr2 + dt*d_mr2,mr3 + dt*d_mr3,M0,...
%    R1, R2, delta_w, ps_grad(:,:,:), D,...
%    ctr,t,dt,...
%    spin_number,spin_number_XY);
%mr1=mr1+dt*d_mr1/6;
%mr2=mr2+dt*d_mr2/6;
%mr3=mr3+dt*d_mr3/6;

mr1_2=sum(sum(sum(mr1)))/spin_number;
mr2_2=sum(sum(sum(mr2)))/spin_number;
mr3_2=sum(sum(sum(mr3)))/spin_number;

% p1 and p2 controls the subplot windows for the graphic
% output depending on the acqusition phase
if acq(v)==0
    p1=3;p2=5;
    mr1_1_v=mr1_1; mr1_2_v=mr1_2;
    mr2_1_v=mr2_1; mr2_2_v=mr2_2;
end

if acq(v)==pi/2
    % "-mr1_1" magnetization sent to p1=5 subplot
    % dedicated for the My signal in aqusition frame
    p1=5;p2=3;
    mr1_1_v=-mr1_1; mr1_2_v=-mr1_2;
    mr2_1_v=mr2_1;  mr2_2_v=mr2_2;
end

if acq(v)==pi
    p1=3;p2=5;
    mr1_1_v=-mr1_1; mr1_2_v=-mr1_2;
    mr2_1_v=-mr2_1; mr2_2_v=-mr2_2;
end

if acq(v)==3*pi/2
    p1=5;p2=3;
    mr1_1_v=mr1_1;  mr1_2_v=mr1_2;
    mr2_1_v=-mr2_1; mr2_2_v=-mr2_2;
end
```

```

%figure(2);
%subplot(4,2,3);title('<mr_x>');drawnow;hold on;
%subplot(4,2,5);title('<mr_y>');drawnow;hold on;

%subplot(4,2,p1);
%line([t t+dt],[mr1_1_v mr1_2_v],'color',v_color(v));
%title('<mr_x>');
%grid on;axis tight;drawnow;hold on;

%subplot(4,2,p2);
%line([t t+dt],[mr2_1_v mr2_2_v],'color',v_color(v));
%plot(t+dt, 2*(tau_dipolar/(t+dt))*real(besselj(2,-(t+dt)/tau_dipolar)),'r.');
%title('<mr_y>');
%grid on;axis tight;drawnow;hold on;

%subplot(4,2,7);
%line([t t+dt],[mr3_1 mr3_2],'color',v_color(v));
%title('<mr_z>');
%grid on;axis tight;drawnow;hold on;

%saveas(gcf, strcat('General','_',num2str(v),'_',num2str(counter)), 'jpg');

% Need to make all previous .mat files equal to 0, starting
% with counter=1 for the first phase setp only
if v==1
    name=strcat('Mx','_',num2str(counter));
    d_mr1=0.0*d_mr1; eval(['save ' name ' d_mr1']);

    name=strcat('My','_',num2str(counter));
    d_mr2=0.0*d_mr2; eval(['save ' name ' d_mr2']);

    name=strcat('Mz','_',num2str(counter));
    d_mr3=0.0*d_mr3; eval(['save ' name ' d_mr3']);
end
% the same phase cycling scheme as before
if acq(v)==0
    d_mr1=mr1; d_mr2=mr2;
end

if acq(v)==pi/2
    d_mr1=mr2; d_mr2=-mr1;
end

if acq(v)==pi
    d_mr1=-mr1; d_mr2=-mr2;
end

if acq(v)==3*pi/2
    d_mr1=-mr2; d_mr2=mr2;
end

% updating the accumulated value of magnetization with each step

name=strcat('Mx','_',num2str(counter));
d_mr3=d_mr1;
eval(['load ' name ' d_mr1']);
d_mr1=d_mr3+d_mr1;
eval(['save ' name ' d_mr1']);

name=strcat('My','_',num2str(counter));
d_mr3=d_mr2;
eval(['load ' name ' d_mr2']);
d_mr2=d_mr3+d_mr2;
eval(['save ' name ' d_mr2']);

name=strcat('Mz','_',num2str(counter));
d_mr2=mr3;
```

```
                    eval(['load ' name ' d_mr3']);
                    d_mr3=d_mr2+d_mr3;
                    eval(['save ' name ' d_mr3']);

                    mr1_1=mr1_2;
                    mr2_1=mr2_2;
                    mr3_1=mr3_2;

                    t=t+dt;
                    counter=counter+1;
                end
            end

            N=counter-1;
            load('Mx_0.mat');
            load('My_0.mat');
            load('Mz_0.mat');

            mr1_1=sum(sum(sum(d_mr1)))/spin_number;
            mr2_1=sum(sum(sum(d_mr2)))/spin_number;
            mr3_1=sum(sum(sum(d_mr3)))/spin_number;

            t=0;counter=1;
            % ploting result of phase cycling after uploading the final
            % values of magnetization
            while counter<=N;

                load(strcat('Mx_',num2str(counter)));
                load(strcat('My_',num2str(counter)));
                load(strcat('Mz_',num2str(counter)));

                mr1_2=sum(sum(sum(d_mr1)))/spin_number;
                mr2_2=sum(sum(sum(d_mr2)))/spin_number;
                mr3_2=sum(sum(sum(d_mr3)))/spin_number;

                %figure(2);

                %subplot(4,2,3);
                %line([t t+dt],[mr1_1 mr1_2],'color','b','Linewidth',2);
                %title('<mr_x>');
                %grid on;axis tight;hold on;

                %subplot(4,2,5);
                %line([t t+dt],[mr2_1 mr2_2],'color','b','Linewidth',2);
                %plot(t+dt, 2*(tau_dipolar/(t+dt))*real(besselj(2,-(t+dt)/tau_dipolar)),'r.');
                %title('<mr_y>');
                %grid on;axis tight;hold on;

                %subplot(4,2,7);
                %line([t t+dt],[mr3_1 mr3_2],'color','b','Linewidth',2);
                %title('<mr_z>');
                %grid on;axis tight;hold on;

                mr1_1=mr1_2;
                mr2_1=mr2_2;
                mr3_1=mr3_2;

                t=t+dt;
                counter=counter+1;

                P_olar_My(D_irect)=mr2_2;
                P_olar_Mx(D_irect)=mr1_2;

            end

            %figure(2);%clf;
            %figure(3);clf;

```

```
         end

         Current_G=G_radient(GT);
         eval(['save ' strcat('Polar_NrvSlc','_Dir',num2str(G),'_Gr',num2str(GT)) ' P_olar_My ...
         P_olar_Mx Current_G Object_Data voxel_size R r A_long']);


         %figure(4)
         %subplot(1,2,1);
         %polar(A_ngle,abs(P_olar_Mx));
         %title('Mx');
         %drawnow;hold on;
         %subplot(1,2,2);
         %polar(A_ngle,abs(P_olar_My));
         %title('My');
         %drawnow;hold on;
         %whos;
         clear d_mr1 d_mr2 d_mr3 mr1 mr2 mr3
         %whos;
     end
end
toc
quit
```

```
    function [d_mr1, d_mr2, d_mr3] = ddf_bloch_eqns(mr1,mr2,mr3,M0,...
        R1, R2, delta_w,ps_grad, D,...
        ctr,t,dt,...
        spin_number,spin_number_XY)

    g = 267.522*10^6;                   %units: 1/(s T)
    mu0 = 4*pi*1e-7;                    %units: NA^-2

    b_damp1=0.0;
    b_damp2=0.0;

    %b_damp1 =(sum(sum(sum(mr2)))/spin_number)/(g*M0*tau_damping);
    %b_damp2 =(sum(sum(sum(mr1)))/spin_number)/(g*M0*tau_damping);

    [br1, br2, br3] = ddf(mr1,mr2,mr3);


    d_mr1 =  mr2.* (delta_w + 2*pi*ps_grad + g*mu0*M0*br3) - mr3 .* (g*b_damp2 + g*mu0*M0*br2) + ...
    diffusion_term(D, mr1) - R2.*mr1;
    d_mr2 = -mr1.* (delta_w + 2*pi*ps_grad + g*mu0*M0*br3) + mr3 .* (g*b_damp1 + g*mu0*M0*br1) + ...
    diffusion_term(D, mr2) - R2.*mr2;
    d_mr3 =  mr1.* (g*b_damp2+g*mu0*M0*br2) - mr2 .* (g*b_damp1+g*mu0*M0*br1) + ...
    diffusion_term(D, mr3)-R1.*mr3+R1;

    %-------------------------------------------------------------
    function diff_term = diffusion_term(D,mr1);
    diff_term = 0;                  % needs to be implemented
```

```
function [br1, br2, br3] = ddf(mr1, mr2, mr3)
voxels = size(mr1,1);
%non_local_sum=zeros(voxels,voxels,voxels);
deltak = zeros(size(mr1));

%zero_freq_file = ['ddf_0freq_' num2str(voxels)];
%file_exists = which([zero_freq_file '.mat']);
%if isempty(file_exists)
%    for r1=1:voxels
%        for r2=1:voxels
%            for r3=1:voxels
%                for rp1=1:voxels
%                    for rp2=1:voxels
%                        for rp3=1:voxels
%                            if rp1 == r1 & rp2 == r2 & rp3 == r3
%              integrand(rp1,rp2,rp3)= 0;
```

```
%                            else
%              integrand(rp1,rp2,rp3)= (1-3*((r3-rp3)^2/((r1-rp1)^2 + (r2-rp2)^2 + (r3-rp3)^2))) / ...
%                                (2*((r1-rp1)^2 + (r2-rp2)^2 + (r3-rp3)^2)^1.5);
%                            end
%                        end
%                    end
%                end
%              non_local_sum(r1,r2,r3) = sum(sum(sum(integrand)));
%            end
%        end
%    end
%eval([’save ’ zero_freq_file ’ non_local_sum’]);
%else
%eval([’load ’ zero_freq_file ’ non_local_sum’]);
%end

%load(’ddf_0freq_217.mat’);

%br1_from_0_component = -1/(4*pi)*non_local_sum;
%br2_from_0_component = -1/(4*pi)*non_local_sum;
%br3_from_0_component =  2/(4*pi)*non_local_sum;


zero_freq = floor(voxels/2 +1); %calculate using filter symetric about zero freq
deltak_file = [’ddf_deltak_’ num2str(voxels)];
file_exists = which([deltak_file ’.mat’]);
if isempty(file_exists)
    for k1=1:voxels;
        for k2=1:voxels;
            for k3=1:voxels
                if k1==zero_freq & k2==zero_freq & k3==zero_freq
                    deltak(k1,k2,k3) = 0;
                else
                    deltak(k1,k2,k3) = (3*((k3-zero_freq)^2 / ...
                    ((k1-zero_freq)^2 + (k2-zero_freq)^2 + (k3-zero_freq)^2)) - 1)/2;
                end
            end;
        end;
    end
    eval([’save ’ deltak_file ’ deltak’]);
%else
%    eval([’load ’ deltak_file ’ deltak’]);
end

%deltak=ones(voxels,voxels,voxels);

br1=fftn(mr1);  br1=fftshift(br1);
br2=fftn(mr2);  br2=fftshift(br2);
br3=fftn(mr3);  br3=fftshift(br3);

eval([’load ’ deltak_file ’ deltak’]);

br1=deltak.*br1;
br2=deltak.*br2;
br3=deltak.*br3;

clear deltak;

br1=ifftshift(br1); br1=ifftn(br1); br1=real(-1/3*br1);
br2=ifftshift(br2); br2=ifftn(br2); br2=real(-1/3*br2);
br3=ifftshift(br3); br3=ifftn(br3); br3=real( 2/3*br3);


%br1 =   real(-1/3*( ifftn(ifftshift(deltak.*fftshift(br1)))));%-mk1/voxels^3*1/(4*pi)*non_local_sum;
%br2 =   real(-1/3*( ifftn(ifftshift(deltak.*fftshift(br2)))));%-mk2/voxels^3*1/(4*pi)*non_local_sum;
%br3 =   real( 2/3*( ifftn(ifftshift(deltak.*fftshift(br3)))));%+mk3/voxels^3*2/(4*pi)*non_local_sum;
```

```
function [mr1_after_rot, mr2_after_rot, mr3_after_rot] = instant_rf( ...
```

```
    mr1, mr2, mr3, rf_radians, rf_phases)
    mr1_after_rot = ...
        cos(rf_phases)*( ...
            mr1  ...
        ) + ...
        sin(rf_phases)*( ...
            mr1*cos(rf_radians) - mr3*sin(rf_radians) ...
        );
    mr2_after_rot = ...
        cos(rf_phases)*( ...
            mr2*cos(rf_radians) + mr3*sin(rf_radians)  ...
        ) + ...
        sin(rf_phases)*( ...
            mr2 ...
        );
    mr3_after_rot = ...
        cos(rf_phases)*( ...
            -mr2*sin(rf_radians) + mr3*cos(rf_radians)  ...
        ) + ...
        sin(rf_phases)*( ...
            mr1*sin(rf_radians) + mr3*cos(rf_radians) ...
        );
```

```
function [mr1_after_grad, mr2_after_grad, mr3_after_grad] = instant_grad( ...
    mr1, mr2, mr3, g_cycl_mat)

    mr1_after_grad = ...
        cos(2*pi*g_cycl_mat).*( ...
            mr1  ...
        ) + ...
        sin(2*pi*g_cycl_mat).*( ...
            mr2 ...
        );
    mr2_after_grad = ...
        cos(2*pi*g_cycl_mat).*( ...
            mr2  ...
        ) - ...
        sin(2*pi*g_cycl_mat).*( ...
            mr1 ...
        );
    mr3_after_grad = mr3;
```

REFERENCES

[1] E. Mark Haacke, Robert W. Brown, Michael R. Thompson, and Ramesh Venkatesan. *Magnetic Resonance Imaging. Physical Principles and Sequence Design.* A John Wiley & Sons, Inc., Publications, New York, N.Y., 1999.

[2] G. Deville, M. Bernier, and J.M. Delrieux. NMR multiple echoes observed in solid ^{3}He. *Phys. Rev. B*, 19(11):5666–5689, 1979.

[3] R. Bowtell, R.M. Bowley, and P. Glover. Multiple spin echoes in liquids in a high magnetic field. *J. Magn. Reson.*, 88:643–651, 1990.

[4] Gheorghe D. Mateescu and Adrian Valeriu. *2D NMR: Density Matrix and Product Operator Treatment.* Prentice Hall, Englewood Cliffs, NJ, 1993.

[5] Wolfgang Richter and Warren S. Warren. Intermolecular multiple quantum coherences in liquids. *Concep. Magn. Reson.*, 12(6):396–409, 2000.

[6] R. Bowtell, S. Gutteridge, and C. Ramanathan. Imaging the long-range dipolar field in structured liquid state samples. *J. Magn. Reson.*, 150:147–155, 2001.

[7] Tilman Enss, Sangdoo Ahn, and Warren S. Warren. Visualizing the dipolar field in solution NMR and MR imaging: three-dimensional structure simulations. *Chem. Phys. Lett.*, 305:101–108, 1999.

[8] Luiz Carlos Junqueira and Jose Carneiro. *Basic Histology:Text and Atlas, 11th Edition.* McGraw-Hill, New York, N.Y., 2005.

[9] I. I. Rabi, J. R. Zacharias, S. Millman, and P. Kusch. A new method of measuring nuclear magnetic moment. *Phys. Rev.*, 53(4):318–318, 1938.

[10] Otto Stern. A new method for the measurement of the bohr magneton. *Phys. Rev.*, 10(4):852–854, 1937.

[11] http://nobelprize.org/.

[12] Raymond Damadian. Tumor detection by nuclear magnetic resonance. *Science*, 171(3976):1151–1153, 1971.

[13] P.C. Lauterbur. Image formation by induced local interactions: Examples employing nuclear magnetic resonance. *Nature*, 242(5394):190–191, 1973.

[14] A. Kumar, D. Welti, and R.R. Ernst. NMR Fourier zeugmatography. *J. Magn. Reson.*, 18(1):69–83, 1975.

[15] http://www.magnet.fsu.edu/.

[16] W. Dürr, D. Hentschel, R. Ladebeck, R. Oppelt, and A. Oppelt. Abstract, 8th Annual Meeting Society of Magnetic Resonance in Medicine. page 1173, 1989.

[17] P. Glover, R. Bowtell, P. Harvey, M. McJury, G. Brown, and P. Mansfield. Abstract, 8th Annual Meeting Society of Magnetic Resonance in Medicine. page 285, 1989.

[18] D. Einzel, G. Eska, Y. Hirayoshi, T. Kopp, and P. Wolfe. Multiple spin echoes in a normal fermi liquid. *PRL*, 53:2312–2315, 1984.

[19] Warren S. Warren, Wolfgang Richter, Amy Hamilton Andreotti, and Bennett T. Farmer II. Generation of impossible cross-peaks between bulk water and biomolecules in solution nmr. *Science*, 262:2005–2009, 1993.

[20] W. Aue, E. Bartholdi, and R.R. Earnst. Two-dimensional spectroscopy. application to nuclear magnetic resonance. *J. Chem. Phys.*, 64(5):2229–2246, 1976.

[21] J. Jeener. Equivalence between the classical and the warren approaches for the effects of long range dipolar couplings in liquid nuclear magnetic resonance. *J. Chem. Phys.*, 112(11):5091–5094, 2000.

[22] A. Abragam. *The principles of nuclear magnetism.* McGraw-Hill, London,UK, 1961.

[23] Y.Y. Lin, N. Lisitza, S. Ahn, and W. S. Warren. Resurrection of crushed magnetization and chaotic dynamics in solution nmr spectroscopy. *Science*, 290(5489):118–120, 2000.

[24] P. Kumar. Excitation of multiple quantum coherences by a single nonselective radiofrequency pulse due to the breakdown of the high-field approximation. *Chem. Phys. Lett.*, 259:611–613, 1996.

[25] S. Lee, W. Richter, S. Vathyam, and W. S. Warren. Quantum treatment of the effects of dipole-dipole interactions in liquid nuclear magnetic resonance. *J. Chem. Phys.*, 105(3):874–900, 1996.

[26] http://www.chem.duke.edu/ wwarren/nmr.php.

[27] R. Bowtell. Indirect detection via the dipolar demagnetizing field. *J. Magn. Reson.*, 100:1–17, 1992.

[28] Wolfgang Richter, Sanghyuk Lee, Warren S. Warren, and Qiuhong He. Imaging with intermolecular multiple-quantum coherences in solution nuclear-magnetic-resonance. *Science*, 267:654, 1995.

[29] R. Bowtell and P. Robyr. Structural investigations with the dipolar demagnetizing field in solution NMR. *Phys. Rev. Lett.*, 76(26):4971–4974, 1996.

[30] Warren S. Warren, Sangdoo Ahn, Marlene Mescher, Michael Garwood, Kamil Ugurbil, Wolfgang Richter, Rahim R. Rizi, Jeff, Hopkins, and John S. Leigh. Mr imaging contrast enhancement based on intermolecular zero quantum coherences. *Science*, 281:247, 1998.

[31] Wolfgang Richter, Marlene Richter, Warren S. Warren, Hellmut Merkle, Peter Andersenb, Gregor Adriany, and Kamil Ugurbilb. Functional magnetic resonance imaging with intermolecular multiple-quantum coherences. *Magn. Reson. Imag.*, 18:489–494, 2000.

[32] Geoffrey D. Charles-Edwards, Geoffrey S. Payne, Martin O. Leach, and Angelo Bifone. Effects of residual single-quantum coherences in intermolecular multiple-quantum coherence studies. *J. Magn. Reson.*, 166:215–227, 2004.

[33] P. Robyr and R. Bowtell. Nuclear magnetic resonance microscopy in liquids using the dipolar field. *J. Chem. Phys.*, 106(2):467–476, 1997.

[34] Louis-Serge Bouchard, Rahim R. Rizi, and Warren S. Warren. Magnetization structure contrast based on intermolecular multiple-quantum coherences. *Magn. Reson. Med.*, 48:973–979, 2002.

[35] F. M. Alessandri, S. Capuani, and B. Maraviglia. Multiple spin echoes in heterogeneous systems:physical origins of the observed dips. *J. Magn. Reson.*, 156:72–78, 2002.

[36] Chih-Liang Chin, Xiaoping Tang, Louis-S. Bouchard, Punam K. Saha, Warren S. Warren, and Felix W. Wehrli. Isolating quantum coherences in structural imaging using intermolecular double-quantum coherence MRI. *J. Magn. Reson.*, 165:309–314, 2003.

[37] Louis-S. Bouchard, Felix W. Wehrli, Chih-Liang Chin, and Warren S. Warren. Structural anisotropy and internal magnetic fields in trabecular bone: Coupling solution and solid dipolar interactions. *J. Magn. Reson.*, 176:27–36, 2005.

[38] Jianhui Zhong, Zhong Chen, and Edmund Kwok. New image contrast mechanisms in intermolecular double-quantum coherence human MR imaging. *J. Magn. Reson. Imag.*, 12:311–320, 2000.

[39] Rahim R. Rizi, Sangdoo Ahn, David C. Alsop, Sean Garrett-Roe, Marlene Mescher, Wolfgang Richter, Mitchell D. Schnall, John S. Leigh, and Warren S. Warren. Intermolecular zero-quantum coherence imaging of the human brain. *Magn. Reson. Med.*, 43:627–632, 2000.

[40] X.-P. Tang, C.-L. Chin, L.-S. Bouchard, F.W.Wehrli, and Warren S. Warren. Observing bragg-like diffraction via multiple coupled nuclear spins. *Phys. Lett. A*, 326:114–125, 2004.

[41] Chandrasekhar Ramanathan and Richard W. Bowtell. Nmr imaging and structure measurements using the long-range dipolar field in liquids. *Phys. Rev. E*, 66:041201, 2002.

[42] Louis-S. Bouchard and Warren S. Warren. Reconstruction of porous material geometry by stochastic optimization based on bulk nmr measurements of the dipolar field. *J. Magn. Reson.*, 170:299–309, 2004.

[43] P. Robyr and R. Bowtell. Measuring patterson functions of inhomogeneous liquids using the nuclear dipolar field. *J. Chem. Phys.*, 107(3):702–706, 1997.

[44] W.H. Press, S.A. Teukolsky, W.T. Vetterling, and B.P. Flannery. *Numerical Recipies in C, 2nd ed.* Cambridge University Press, New York, N.Y., 1992.

[45] W.S. Warren, S. Lee, W. Richter, and S. Vathyam. Correcting the classical dipolar demagnetizing field in solution NMR. *Chem. Phys. Lett.*, 247:207–214, 1995.

[46] J. P. Marques, Sir Peter Mansfield, S. Grant, S. Blackband, and R. W. Bowtell. Intermolecular multiple quantum coherences at high magnetic field: The nonlinear regime. *J. Chem. Phys.*, 123:164311, 2005.

[47] Louis-S. Bouchard and Warren S. Warren. Multiple-quantum vector field imaging by magnetic resonance. *J. Magn. Reson.*, 177:9–21, 2005.

[48] P. J. Basser, J. Mattiello, and D. LeBihan. MR diffusion tensor spectroscopy and imaging. *BioJrn*, 66:259–267, 1994.

[49] Bruce M. Damon, Zhaohua Ding, Adam W. Anderson, Andrea S. Freyer, and John C. Gore. Validation of diffusion tensor MRI-based muscle fiber tracking. *Magn. Reson. Med.*, 48:97–104, 2002.

[50] Christian Beaulieu. The basis of anisotropic water diffusion in the nervous system–a technical review. *NMR in Biomedicine*, 15:435–455, 2002.

[51] S. M. Brown, P. N. Sen, and D. G. Cory. Nuclear magnetic resonance scattering across interfaces via the dipolar demagnetizing field. *J. Chem. Phys.*, 124:295, 2002.

[52] Silvia Capuani, Francesca Curzi, Francesco Maria Alessandri, Bruno Maraviglia, and Angelo Bifone. Characterization of trabecular bone by dipolar demagnetizing field MRI. *Magn. Reson. Med.*, 46:683–689, 2001.

[53] S. Capuani, M. Alesiani, F.M. Alessandri, and B. Maraviglia. Characterization of porous media structure by non linear nmr methods. *Magn. Reson. Imag.*, 19:319–323, 2001.

[54] Jianhui Zhong, Zhong Chen, and Edmund Kwok. In vivo intermolecular double-quantum imaging on a clinical 1.5 T MR scanner. *Magn. Reson. Med.*, 43:335–341, 2000.

[55] Bahadir Ozus, Geoffrey D. Clarke, Stephen J. Dodd, and Gary D. Fullerton. Orientational dependence of intermolecular double quantum coherence (iDQC) signal from tendon tissue. *Magn. Reson. Med.*, 53:1183–1186, 2005.

[56] T. Hou, Z. Chen, D.W. Hwang, J.H. Zhong, and L.P. Hwang. Intermolecular double-quantum coherence mr microimaging of pig tail with unique image contrast. *Magn. Reson. Imag.*, 22:543–550, 2004.

[57] Bingwen Zheng, Dennis W. Hwang, Zhong Chen, and Lian Pin Hwang. Rotating frame intermolecular double quantum spin-lattice relaxation t1pDQC, DQC weighted magnetic resonance imaging. *Magn. Reson. Med.*, 53:930–936, 2005.

[58] Bingwen Zheng, Zhong Chen, Scott D. Kennedy, and Jianhui Zhong. iDQC MRI weighted by longitudinal relaxation in the rotating frame. *Magn. Reson. Med.*, 56:327–333, 2006.

[59] Kerry L. Shannon, Rosa T. Branca, Gigi Galiana, Silvia Cenzano, Louis-Serge Bouchard, Winston Soboyejo, and Warren S. Warren. Simultaneous acquisition of multiple orders of intermolecular multiple-quantum coherence images in vivo. *Magn. Reson. Imag.*, 22:1407–1412, 2004.

[60] H. Schmalbruch. Fiber composition of the rat sciatic nerve. *The Anatomical Record*, 215:71–81, 1986.

[61] Dimiter Prodanov and Hans K.P. Feirabend. Morphometric analysis of the fiber populations of the rat sciatic nerve, its spinal roots, and its major branches. *J. Comp. Neurol*, 503:85–100, 2007.

[62] J. Carlander, K. Johansson, S. Lindstrom, A. K. Velin, C. H. Jiang, and C. Nordborg. Comparison of experimental nerve injury caused by ultrasonically activated scalpel and electrosurgery. *British Journal of Surgery*, 92(6):772–777, 2005.

[63] Wilson Barros Jr., John C. Gore, and Daniel F. Gochberg. Communications. simultaneous measurement of D and T_2 using the distant dipolar field. *J. Magn. Reson.*, 178:166–169, 2006.

[64] Dorland and William Alexander Newman. *Dorland's Illustrated Medical Dictionary, 29th ed.* W.B. Saunders Company, Philadelphia, PA, 2000.

[65] Laurent Huwart, Frank Peeters, Ralph Sinkus, Laurence Annet, Najat Salameh, Leon C. ter Beek, Yves Horsmans, and Bernard E. Van Beers. Liver fibrosis: non-invasive assessment with mr elastography. *NMR Biomed*, 19(2):173–179, 2006.

[66] Miwa Koinuma, Isamu Ohashi, Kaoru Hanafusa, and Hitoshi Shibuya. Apparent diffusion coefficient measurements with diffusion-weighted magnetic resonance imaging for evaluation of hepatic fibrosis. *J. Magn. Reson. Imag.*, 22(1):80–85, 2005.

[67] Stephanie L. Barnes, Andrej Lyshchik, Mary K. Washington, John C. Gore, and Michael I. Miga. Development of a mechanical testing assay for fibrotic murine liver. *Med. Phys.*, 34(11):4439–4450, 2007.